Dispersion-theoretical analysis of the nucleon electromagnetic form factors

Dissertation

zur

Erlangung des Doktorgrades (Dr. rer. nat.)

der

Mathematisch–Naturwissenschaftlichen Fakultät

der

Rheinischen Friedrich–Wilhelms–Universität Bonn

vorgelegt von

Maxim Belushkin

aus

Dubna

Bonn 2007

Angefertigt mit Genehmigung der Mathematisch-Naturwissenschaftlichen Fakultät der Rheinischen Friedrich-Wilhelms-Universität Bonn

Referent:	Prof. Dr. Ulf-G. Meißner
Koreferent:	Prof. Dr. H.-W. Hammer

Tag der Promotion:	22 Juni 2007
Erscheinungsjahr:	2007

Diese Dissertation ist auf dem Hohschulschriftenserver der ULB Bonn `http://hss.ulb.uni-bonn.de/diss_online` elektronisch publiziert.

Declaration

I hereby declare that the work in this thesis is original and has been carried out by me at the Helmholtz Institut für Strahlen- und Kernphysik, Universität Bonn, under the supervision of Prof. Dr. Ulf-G. Meißner and in partial fulfilment of the requirements of the Doctor Of Philosophy Degree of the University of Bonn. I further declare that this work has not been the basis for the awarding of any degree, diploma, fellowship, associateship or similar title of any university or institution.

Maxim Belushkin
April 2007

Helmholtz Institut für Strahlen- und Kernphysik,
Abteilung Theorie, Universität Bonn,
Nußallee 14-16, Bonn 53115,
Germany.

We do not know in advance what are the right questions to ask, and we often do not find out until we are close to an answer.

- Steven Weinberg

Abstract

The structure of the proton and the neutron is of fundamental importance for the study of the strong interaction dynamics over a wide range of momentum transfers. The nucleon form factors encode information on the internal structure of the nucleon as probed by the electromagnetic interaction, and, to a certain extent, reflect the charge and magnetisation distributions within the proton and the neutron.
In this thesis we report on our investigation of the electromagnetic form factors of the proton and the neutron with dispersion relation techniques, including known experimental input on the $\pi\pi$, $K\bar{K}$ and the $\rho\pi$ continua and perturbative QCD constraints. We include new experimental data on the pion form factor and the nucleon form factors in our simultaneous analysis of all four form factors in both the space- and the timelike regions for all momentum transfers, and perform Monte-Carlo sampling in order to obtain theoretical uncertainty bands. Finally, we discuss the implications of our results on the pion cloud of the nucleon, the nucleon radii and the Okubo-Zweig-Iizuka rule, and present our results of a model-independent approach to estimating two-photon effects in elastic electron-proton scattering.
The results of this thesis have been published in parts:

[1] *Novel evaluation of the two-pion contribution to the nucleon isovector form factors*, M. A. Belushkin, H.-W. Hammer, Ulf-G. Meißner, Phys. Lett. B 633 (2006) 507-511 [arXiv: hep-ph/0510382]

[2] *Dispersion analysis of the nucleon form-factors including meson continua*, M. A. Belushkin, H.-W. Hammer, Ulf-G. Meißner, Phys. Rev. C 75 (2007) 035202 [arXiv: hep-ph/0608337]

[3] *Model-independent extraction of two-photon effects in elastic electron-proton scattering*, M. A. Belushkin, H.-W. Hammer, Ulf-G. Meißner, in preparation.

Contents

Chapter 1

Introduction

Nucleons - the proton and the neutron - are building blocks of matter. Nevertheless, they are not fundamental. They are complex composite objects, their constituents being quarks and gluons. The discovery of the proton and the neutron have played a key role in the development of the theory of the strong force - quantum chromodynamics (QCD).

Ever since the proton and the neutron were discovered, they have posed challenges of increasing complexity to nuclear physics. At first, the nucleons were considered to be point-like, structureless spin-$\frac{1}{2}$ Dirac particles. Their masses were known to be nearly identical. The proton was known to have a positive charge, the neutron - no net charge. The strength of the interaction between any pair of nucleons was also known to be the same. The combination of these facts hinted at a symmetry of the underlying Hamiltonian. The symmetry would necessarily be approximate, since the masses of the proton and the neutron are not exactly the same. In 1932, Heisenberg [Hei32] introduced the concept of isospin in analogy to the particle spin. He proposed that the proton and the neutron are two states of the same particle - the nucleon. Both particles are isospin $\frac{1}{2}$, but, by definition, the projection of isospin onto a fixed direction in isospin space is $I_3 = +\frac{1}{2}$ for the proton, and $I_3 = -\frac{1}{2}$ for the neutron. Heisenberg presented a mathematical formulation of the isospin symmetry: the underlying Hamiltonian of the strong interactions is invariant under the action of the Lie group SU(2). We now know that isospin symmetry is a subgroup of a much larger flavour symmetry group.

Due to the charges of the nucleons, enormous Coulomb repulsion must necessarily exist within the nuclei. The existence of a new fundamental force, the strong force, was evident. In 1935, Yukawa postulated a new particle [Yuk35], the pion, which was, in analogy to the photon and the electromagnetic interaction, the quantum field responsible for mediating the strong interaction. The pion mass was determined by the range of the nuclear force. Experimental evidence for

the existence of two charged pions came in 1947 with the works of Powell and his collaborators [LMOP47, LOP47a, LOP47b]. Powell was awarded the 1950 Nobel Prize for this discovery. The neutral pion was discovered in 1948, completing the pion triplet. The fundamental role of the pion cloud surrounding the nucleons was already becoming evident.

Alongside the studies of the nucleon interactions, first evidence of the composite nature of the nucleons was emerging. In 1933, R. Frisch and O. Stern [FS33] performed a measurement of the proton's magnetic moment. A point-like spin-$\frac{1}{2}$ Dirac particle possesses a magnetic moment of ~ 1 nuclear magnetons. The measurement of Frisch and Stern yielded a value "between 2 and 3 nuclear magnetons" [FS33]. Further experimental evidence for the composite nature of the proton was to come in the 1950's.

In 1952, another breakthrough came as Glaser introduced the bubble chamber [GR55], a discovery for which he was awarded the Nobel Prize in 1960. This paved the way to the discovery of a large number of particles - by the late 1960's, over 100 particles were known. A classification scheme for baryons and mesons was proposed by Gell-Mann [Gel62] and Ne'eman [Nee61] in 1961, called the Eightfold way. This was an extension of the original isospin symmetry proposed by Heisenberg. Gell-Mann organised the mesons and spin-$\frac{1}{2}$ baryons into octets, and the spin-$\frac{3}{2}$ baryons into a decuplet within a SU(3) scheme, now known as flavour-SU(3). The decuplet predicted a new particle - the Ω^-, which was indeed experimentally observed in 1964, proving the success of the approach.

At the same time, new experimental evidence for the composite nature of the nucleons came from the Stanford Linear Accelerator Centre (SLAC). In 1955, high-energy elastic electron-proton scattering experiments were performed [HA55]. Strong deviations in the measured cross section compared to the cross section for scattering on a point-like particle were observed. A prediction for the charge radius of the proton emerged - $\langle r^2 \rangle^{1/2} \sim 0.8$ fm [Hof57]. The composite nature of the proton helped explain many other experimental results at that time, i.e. the abundance of pions produced in electron-positron reactions in Frascati, and a large number of inelastic reactions at a neutrino beam in CERN.

As the number of particles being discovered grew, it became apparent that they can not all be fundamental particles. In 1964, Gell-Mann [Gel64] and Zweig [Zwe64] independently proposed that hadrons are composed from quarks: baryons from three quarks or anti-quarks, and mesons from quark-antiquark pairs. The nuclear force no longer is the fundamental force of the strong interaction - nucleons and pions are composite particles, and the field of the strong interaction is not the pion but the gluon field, coupled to the colour charges of the quarks. The nuclear force is the remnant of the strong force. For his works, Gell-Mann was awarded the Nobel Prize in Physics in 1969, and the research laid the foundation of the theory of strong interactions - quantum chromodynamics (QCD).

When quarks were first proposed, it was not clear whether they are

merely a convenient mathematical concept or new subnuclear particles, especially due to the fact that experimental searches for free quarks gave negative results. Quarks are confined within hadrons, and, as the colour force increases with increasing distance between them, they can not be separated. Experiments dealing with deep inelastic scattering of electrons on the nucleons were to a large extent responsible for the present conviction that we can determine the properties of the quarks even though they can not be isolated - just as the early experiments dealing with the scattering of electrons on nuclei implied that the electron scatters off some charged particle which stays intact while the nucleus breaks into pieces, similar evidence was obtained in high energy electron-proton scattering experiments.

The study of the internal structure of the nucleons not only provides a fundamental test of QCD, but is also important for the understanding of a wide range of nuclear reactions. For example, precise knowledge of the nucleon form factors is of great importance in the analysis of parity violation experiments designed to probe the strangeness content of the nucleon [Mue97, Ani98]; investigations of the electromagnetic interactions of nuclei like the deuteron [Phi06] or ^{16}O [Fis04], as well as other light nuclei [Sic01] also require high precision knowledge of the nucleon structure.

This thesis is organised as follows. In Chapter 2, an introduction to the problem of the structure of the nucleons is presented. The nucleon structure functions - the form factors - are introduced. Elastic electron-nucleon scattering, a time-honoured tool to probe the electromagnetic structure of the nucleons, is discussed in the one-photon exchange approximation. The scattering process is related to intermediate meson exchange processes, and dispersion relations are introduced as a model-independent framework for the analysis of the nucleon form factors.

In Chapter 3, the theoretical input and the constraints for the form factors is discussed. It is shown how certain contributions from the intermediate states can be constructed from experimental data. Asymptotic constraints are discussed, and two models that we have developed to enforce these constraints and, at the same time, parameterise the unknown multi-particle exchange contributions are presented.

Chapter 4 presents two modern techniques used to extract information about the structure of the nucleons from experimental data. Corrections to the one-photon exchange and their influence on the process of obtaining the form factors are discussed in relation to a long-standing discrepancy between the results obtained using different experimental techniques.

In Chapter 5 a mathematical formulation of the analysis of experimental data is given. Different regression methods and the implementation of constraints are presented, and the use of Monte-Carlo techniques for the production of the theoretical uncertainty estimates is discussed.

The results of our form factor analyses are presented in Chapter 6. First, our reanalysis of the important two-pion exchange contribution is given together

with our investigation of the pion cloud of the nucleon. It is followed by our results for the form factors obtained within the two models developed to enforce the correct asymptotic form factor behaviour. The chapter concludes with the results of our analysis of potential additional structure in the neutron electric form factor, the implications of such structure for the pion cloud of the nucleon, and the analysis of the preliminary experimental data from the CLAS collaboration.

In Chapter 7 we present the results of our cross section analysis, and our model-independent estimate of additional corrections not present in the standard corrections applied to experimental data. We conclude that the difference between the results of different experimental techniques is not as dramatic as originally thought, and it can indeed be explained by two photon exchange effects.

Finally, a summary of our results and an outlook on future refinements and upcoming experimental data are presented in Chapter 8.

Chapter 2

The Structure of the Nucleon

The determination of the structure of the nucleon is one of the key problems of hadronic physics. Nucleons are composite systems, the constituents being quarks and gluons bound by increasingly strong forces for decreasing momentum transfers, which corresponds to increasing distances. In the GeV region, the spacial scale is $\sim$ 1 fm - the order of the range of the nuclear force, the strong running coupling constant $\alpha_s(Q^2)$ becomes increasingly large. This brings the problem into the sphere of non-perturbative quantum chromodynamics. In this regime, confinement is extremely important - i.e. the fact that the strong force confines quarks into pairs and triplets - and the nucleon structure and interactions are determined by hadronic degrees of freedom, rather than quarks and gluons.

2.1 Electron Scattering as a Probe of Nucleon Structure

Elastic electron-nucleon scattering is traditionally the simplest and most effective way to extract information about the nucleon structure. If the nucleons were point-like, structureless particles, the cross section for electron-nucleon scattering would be given by the Mott cross section. More than 50 years have passed since the early experiments at SLAC [HA55] revealed deviations of the cross section for the scattering of electrons on protons at rest from the Mott cross section. During this time, the problem of hadronic structure in general, and of nucleon structure in particular, has received wide interest from both the experimental and the theoretical sides.

The earliest theoretical investigations of the problem of nuclear structure as probed in elastic electron-nucleon scattering experiments are usually credited to Rosenbluth [Ros50]. In 1950, he used the then-novel Feynman techniques to

calculate the cross section for high-energy elastic electron-nucleon scattering, which involved modified charge and magnetic moment expressions for the proton. They were calculated under the assumption that the proton in the reaction spends part of the time in the state of a neutron and a positively charged meson. While Rosenbluth did not introduce the structure functions of the proton explicitly in his expression for the cross section, the modified charge and magnetic moment he calculated depended on a kinematical variable for the process, describing the effects of the charge and magnetisation distributions within the proton.

In 1956, Hofstadter related the electron-proton cross section for elastic scattering to the Mott cross section for the scattering of an electron on a point-like proton [Hof56] directly through the charge density distribution within the proton. He introduced the structure functions - the form factors - explicitly as a Fourier transform of the charge distribution function. This laid the foundations for the development of the first method for the extraction of the nucleon structure functions from the experimental data on the cross sections for elastic electron-nucleon scattering.

Since 1968, an alternative approach to measuring the nucleon form factors has been actively developed - polarisation transfer (PT) [AR68, Dom69, AR74, ACG80, DR85, RD88]. In polarisation transfer experiments, a polarised electron beam scatters on an unpolarised nucleon target, and the electron polarisation is transferred to the recoil nucleon. In double polarisation experiments, a polarised electron beam scatters on a polarised nucleon target, and the recoil nucleon acquires an additional polarisation vector component.

In recent years, high-precision polarisation transfer experiments have been widely performed. Their results do not agree with the results of previous unpolarised scattering experiments which employ the Rosenbluth separation technique. This discrepancy has been a subject of intense investigation. In Chapter 4 a detailed explanation of both techniques and the possible origins of this problem are discussed, and in Chapter 7 the results of our analysis of this problem are presented.

In addition to elastic scattering processes, which provide information for the form factors in the so-called spacelike region, a number of inelastic processes also allow one to access information about the structure of the nucleons in the so-called timelike region. For example, the form factors in the timelike region have been measured in electron-positron annihilation into a nucleon-antinucleon pair. The form factors in the spacelike and the timelike regions are not independent. In fact, if the form factors in one of these regions were known with infinite precision, the form factors in the other region would be uniquely determined. A discussion of the analytic properties of the nucleon form factors is presented in Section 2.5 of this Chapter.

2.2 Kinematics

In the laboratory frame, an electron of mass m_e and initial four-momentum $k = (E, \vec{k})$ scatters on a nucleon of mass M_N at rest. The initial four-momentum of the nucleon is $p = (M_N, \vec{0})$. In the Born approximation, the scattering is described by the exchange of a single virtual photon with four-momentum $q = k - k'$, where $k' = (E', \vec{k}')$ is the four-momentum of the outgoing electron.

The elastic scattering process $e(k) + N(p) \rightarrow e(k') + N(p')$ is depicted on Figure 2.1 to leading order in the Born approximation (the one-photon exchange approximation). Here k, k', p, p' are the initial and final four-momenta of the electron and of the nucleon, respectively. The scattering process can be described with the help of the Lorentz-invariant Mandelstam variables:

$$s = (k + p)^2, \quad t = (p' - p)^2, \quad u = (k - p')^2 \,. \tag{2.1}$$

Here $t = q^2 = (p' - p)^2$ is the invariant four-momentum transfer squared. It is also convenient to introduce $Q^2 = -q^2$. In the spacelike region, $Q^2 > 0$ and $q^2 < 0$, and in the timelike region $q^2 > 0$ and $Q^2 < 0$. The variable $q = (\omega, \vec{q})$ is often referred to as the photon virtuality.

The Mandelstam variables are related to the kinematic variables in the laboratory frame as:

$$Q^2 = 2EE'(1 - \cos\theta) \,, \tag{2.2}$$

$$s = 2EM_N + M_N^2 + m_e^2 \,, \tag{2.3}$$

where θ is the electron scattering angle.

Due to total momentum conservation, only two of these invariants are independent, satisfying the condition

$$s + t + u = 2M_N^2 + 2m_e^2 \,, \tag{2.4}$$

where M_N and m_e are the masses of the nucleon and the electron, respectively. Furthermore, the four-momenta of the incoming and outgoing electrons and nucleons must satisfy the on-shell conditions:

$$k^2 = k'^{\,2} = m_e^2, \quad p^2 = p'^{\,2} = M_N^2 \,. \tag{2.5}$$

Due to the spins of the particles involved, in general there are $2^4 = 16$ helicity amplitudes required to describe the full scattering process, where helicity is defined as the projection of the total angular momentum onto the direction of motion:

$$h = \vec{J} \cdot \hat{p}, \quad \hat{p} = \frac{\vec{p}}{|\vec{p}|} \,. \tag{2.6}$$

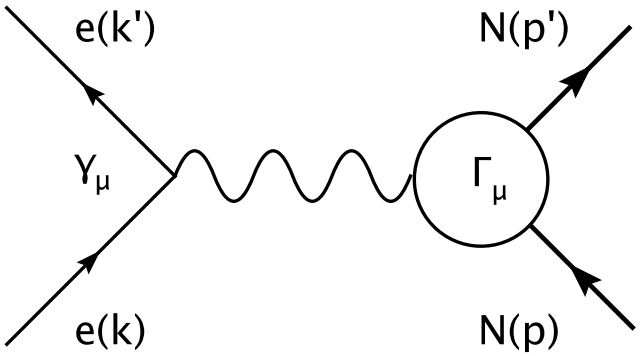

Figure 2.1: The Feynman diagram for the one-photon exchange approximation for elastic electron-nucleon scattering.

Assuming parity and time-reversal invariance [GNO57], only 6 independent invariant amplitudes remain. Furthermore, three more vanish as the electron mass is neglected, a valid approximation since highly relativistic energies are required to probe the nucleon structure. In the Born approximation, where the scattering process is described by the exchange of a single photon as shown on Figure 2.1, one more amplitude vanishes, and all information about the process is encoded in two form factors, which are functions of the invariant four-momentum transfer squared only. They encode all information about the structure of the nucleon as seen by the electromagnetic interaction.

Up until recently, the lowest-order Born approximation corresponding to the Feynman diagram on Figure 2.1 was the only contribution under consideration. While the form factors are intrinsic properties of the nucleons and are therefore independent of this approximation, their extraction from experiment is not. Terms of higher order in the fine structure constant α were included as radiative corrections. Their calculation, however, involved a number of approximations - for example, the effect of the internal structure of the nucleons was neglected. The discrepancy between the Rosenbluth and the polarisation transfer techniques has sparked renewed interest in the consistent treatment of higher order corrections. This topic is discussed in Chapter 4.

2.3 Nucleon Form Factors

The matrix element for the Feynman diagram (Figure 2.1) can be written as:

$$\mathcal{M} = -4\pi i j^e_\mu(k', k)\frac{1}{q^2}J^{\mathrm{em}}_\mu(p', p)\,, \tag{2.7}$$

where $j^e_\mu(k',k)$ is the electron's charge current density,

$$j^e_\mu(k',k) = -ie\bar{u}(k')\gamma_\mu u(k)\,, \tag{2.8}$$

and the current density $J^{\rm em}_\mu(p',p) = ie\bar{u}(p')\Gamma_\mu u(p)$ encodes information about the nucleon's electromagnetic structure.

It has been shown [Fol52, Sal55, YLR57] using Lorentz and gauge invariance that the most general form of the matrix element of the vector current operator between two nucleon states is:

$$\langle p'|\Gamma_\mu|p\rangle = \bar{u}(p')\Big[F_1(t)\gamma_\mu + i\frac{F_2(t)}{2M_N}\sigma_{\mu\nu}q^\nu\Big]u(p)\,, \tag{2.9}$$

where $F_1(t)$ and $F_2(t)$ are the Dirac and Pauli form factors, respectively. They encode information about the structure of the nucleons. At low q^2 they are determined by the gross properties such as the charges and the magnetic moments, while at high momentum transfers they encode information about the quark substructure of the nucleons. Thus, they are normalised at $t = 0$ to the charges and anomalous magnetic moments of the proton and the neutron:

$$F_1^p(0) = 1, \quad F_1^n(t) = 0, \quad F_2^p(0) = \kappa_p, \quad F_2^n(0) = \kappa_n\,, \tag{2.10}$$

where $\kappa_p = 1.793$ and $\kappa_n = -1.913$ in units of nuclear magnetons.

It should be noted that although Eq. (2.9) is the most general way of writing the current vertex, it is not the only way - there are many possible terms that satisfy the invariance requirements. However, by using the Dirac equation, all the forms can be reduced to the form given by Eq. (2.9).

Instead of discussing the proton and neutron form factors directly, it is convenient to introduce an isospin decomposition:

$$\begin{aligned} F_i^{(s)} &= \frac{1}{2}(F_i^p + F_i^n)\,, \\ F_i^{(v)} &= \frac{1}{2}(F_i^p - F_i^n)\,, \end{aligned} \tag{2.11}$$

where $F_i^s(F_i^v)$ are the isoscalar (isovector) form factors, respectively. The importance of this decomposition will be discussed in the following sections.

Another important linear combination of the form factors is given by the Sachs form factors:

$$G_E(t) = F_1(t) - \tau F_2(t), \quad G_M(t) = F_1(t) + F_2(t), \quad \tau = -\frac{t}{4M_N^2}\,. \tag{2.12}$$

The physical meaning of the Sachs form factors is best understood when the hadronic current is written in the Breit frame, where the energy transfer $\omega = 0$

and $Q = |\vec{q}_{\mathrm{Breit}}|$. In that frame in the non-relativistic limit the Sachs form factors can be considered to be the Fourier-transformed charge and magnetic current density distributions $\rho_{\mathcal{C}}$ and $\rho_{\mathcal{M}}$, respectively:

$$\rho_{\mathcal{C},\mathcal{M}}(r) = \frac{4\pi}{(2\pi)^3} \int_0^\infty G_{E,M}(Q) \frac{\sin Qr}{Qr} Q^2 dQ \tag{2.13}$$

The charge and magnetisation distributions determined by Eq. (2.13) should not, however, be interpreted strictly as the physical distribution of charge and magnetic moment within the nucleons. Such an interpretation is only possible in the non-relativistic limit, but the experimental data for the form factors is well in the relativistic regime.

The experimental data for the nucleon form factors is usually given in terms of the Sachs form factors. It is convenient to present the form factor results for G_M^n, G_E^p and G_M^p normalised to the dipole form factor,

$$G_D(Q^2) = \left(1 + \frac{Q^2}{m_D^2}\right)^{-2}, \tag{2.14}$$

with $m_D^2 = 0.71$ GeV^2 determined from a fit to the low-Q^2 form factor data. The dipole form factor describes the electric and the magnetic form factors of the proton and the magnetic form factor of the neutron reasonably well at low momentum transfers. It is a Fourier transform of the exponential radially symmetric charge and magnetisation distributions,

$$G_D(Q^2) = \frac{m_D^3}{2} \int_0^\infty \mathrm{e}^{-m_D r} \frac{\sin(qr)}{q} r \, dr \, . \tag{2.15}$$

2.4 Theoretical Investigation of the Nucleon Form Factors

A number of approaches aimed at describing the nucleon structure which are not based on dispersion relation techniques exist. The applicability of most, however, is limited in the range of momentum transfers. This section gives a brief overview of some of the main alternative approaches.

2.4.1 Constituent Quark Models

In its simplest form, the nucleon is a three-body bound-state problem, the solution of which is difficult to obtain even if the interactions would be well known. A number of constituent quark models (CQM) aimed at describing the nucleon structure exist.

- Cardarelli *et al.* have performed a calculation using a One-Gluon-Exchange (OGE) potential [CPSS95, CS00]. Their calculation yields values of G_E^n qualitatively consistent with the experimental data, but their prediction for the ratio G_M^p/G_M^n turns out to be inconsistent with experimental data.
- Wagenbrunn, Boffi *et al.* have calculated the nucleon electromagnetic form factors using the Goldstone-Boson-Exchange (GBE) potential [WBKP00, BGKP01]. They obtain a reasonably good description of the experimental data, but deviations at increasing Q^2 values become significant for the magnetic form factor of the proton.
- A manifestly covariant CQM calculation using the Bethe-Salpeter equation and an instanton-induced interaction between the quarks was performed by Merten *et al.* [MLKM02]. The results obtained are in quantitative agreement with experimental data, and the correct scaling of the ratio G_E^p/G_M^p is predicted, although the rate of the decrease of the ratio is too large compared to experimental data.
- Gross and Agbakpe performed a covariant CQM calculation using a covariant spectator model [GA04]. Using a ten parameter fit to experimental data, they obtain a good overall description of the form factors in the spacelike region, although the behaviour of G_M^n at high Q^2 values does not describe several experimental points in that region.

2.4.2 Cloudy Bag Model

Pions, as the lightest hadrons, provide the longest-range contribution to the nucleon interactions. An improvement of the CQM models - pion cloud models - include the pionic degrees of freedom.

In the Cloudy Bag model, three constituent quarks are surrounded by a pion cloud. A difference is made between the bare nucleon, which consists of three constituent quarks, and the physically observable nucleon, surrounded by the pion cloud. The photon can interact either with the bare nucleon, the nucleon in the presence of a pion, or with a charged pion from the cloud of the nucleon.

Miller recently performed a light-front cloudy bag model calculation [Mil02]. The result of the calculation describes the neutron form factor data reasonably well, but the proton magnetic form factor is not well reproduced, especially at increasing Q^2 values.

2.4.3 The Skyrme Model

The Skyrme model was developed in 1961 as a non-linear theory of interacting pions [Sky61, Sky62]. It incorporates the symmetries of QCD in a minimal Lagrangian,

operating on a 2×2 unitary field. The fundamental fields entering the non-linear σ-model Lagrangian consist of just the pion fields. The "Skyrmions", i.e. non-trivial classical solutions of the underlying non-linear σ-model, are used to model baryons: in the initial approximation, the nucleon is obtained as a certain classical configuration of pion fields.

Meißner *et al.* have performed a calculation of the nucleon electromagnetic form factors within the framework of an extended Skyrme model, where ρ and ω vector mesons are introduced explicitly as dynamical gauge bosons [MKW86]. The results of the calculation provide a satisfactory agreement of the experimental values up to $Q^2 \sim 0.5$ GeV^2.

More recently, Holzwarth has performed a calculation of the nucleon form factors within the Skyrme model [Hol96]. The results of the calculation reproduce the main features of the form factors up to $Q^2 \sim 1.0$ GeV^2, although the electric form factor of the proton shows a steep decrease starting at $Q^2 \approx 0.5$ GeV^2 which is not supported by the experimental data.

2.4.4 Lattice QCD

Lattice QCD calculations provide an *ab initio* calculation of quantities such as the nucleon electromagnetic form factors from the underlying theory of QCD. Lattice QCD is a discretised version of QCD formulated in terms of path integrals on a space-time lattice. The continuum theory is restored by extrapolating the results obtained at finite lattice spacings to a zero lattice spacing. Due to high computation costs, the calculations are also performed with unphysically large quark masses. Extrapolation to the physical quark masses is not a simple nor a straightforward task, and the uncertainties arising from the extrapolation are large.

There exist two distinct contributions to the calculation of the nucleon electromagnetic form factors using lattice QCD. They are schematically depicted in Figure 2.2. In the connected diagram, the photon couples to one of the quarks in either the initial or the final nucleon. The quark lines correspond to dressed quarks, i.e. include an arbitrary number of gluon exchanges between the quarks. In the so-called quenched approximation, the fluctuations of these gluons into quark-antiquark pairs are neglected. The unquenched calculation additionally includes sea-quark insertions into the gluon lines.

In the second, disconnected diagram, the photon couples to a quark-antiquark pair, which then interacts with the nucleon via the exchange of gluons. The calculation of this contribution in lattice QCD is extremely expensive in terms of computation time, and is neglected in current calculations. It cancels in the isovector form factors, however.

A recent calculation of the nucleon isovector form factors performed by

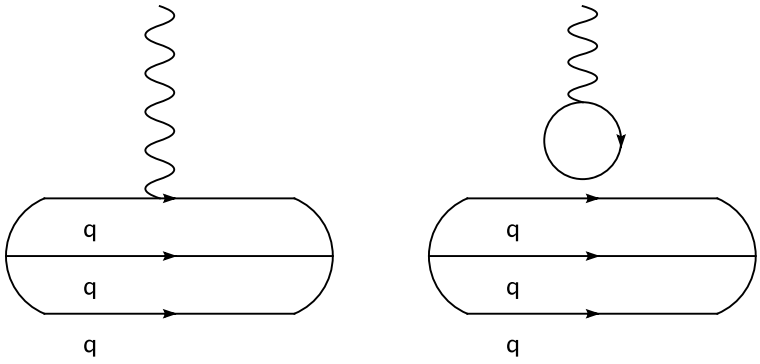

Figure 2.2: Schematic illustration of the two graphs contributing to the calculation of the nucleon electromagnetic form factors in lattice QCD.

the Nicosia-MIT group [AKNT06, Ale06] significantly overestimates the nucleon isovector form factors within both the quenched and the unquenched calculations.

Göckeler *et al.* from the QCDSF collaboration have also performed a calculation of the nucleon form factors in quenched lattice QCD [GHHP03]. They find a good agreement of the calculated ratio $\mu_p G_E^p / G_M^p$ with the experimental data up to $Q^2 \sim 3.5$ GeV^2.

2.4.5 Chiral Perturbation Theory

Chiral perturbation theory (χPT) is a low-energy effective field theory of QCD. The Lagrangian of this effective field theory is constructed to have the symmetries of the QCD Lagrangian. In particular, it incorporates the spontaneously broken chiral symmetry of QCD, as a consequence of which pions emerge as nearly massless Goldstone bosons.

All terms entering the effective Lagrangian are ordered by powers of momentum and masses which are considered small on hadronic scales (e.g. the pion mass), and studied order by order. Different soft scale expansion schemes (power-counting schemes) have been developed in the literature. χPT can also be extended to describe the interactions of Goldstone bosons with heavy ground state baryons. At low momentum transfers, the nucleon form factors can be studied with χPT.

Bernard *et al.* have performed a calculation of the nucleon form factors in the framework of an effective chiral Lagrangian including pions, nucleons and the $\Delta(1232)$ [BFHM98] up to $Q^2 \sim 0.2$ GeV^2. Their results are in good agreement with the dispersion-theoretical analysis of Ref. [MMD95].

Kubis and Meißner have performed a calculation of the nucleon electromagnetic form factors to fourth order in covariant baryon χPT with a phenomeno-

logical extension to include vector mesons [KM00]. They obtained an accurate description of all four nucleon form factors in the spacelike region up to momentum transfers $Q^2 \sim 0.4$ GeV^2.

Schindler *et al.* have calculated the nucleon form factors up to fourth order in manifestly Lorentz-invariant chiral perturbation theory with vector mesons as explicit degrees of freedom [SGS05]. They obtain results similar to the results of Ref. [KM00].

2.4.6 Generalised Parton Distributions

Parton distributions are conveniently introduced in the study of deep inelastic scattering processes, where the individual quarks and gluons are resolved. Parton distributions encode information about the distribution of the longitudal momentum and polarisation carried by quarks, antiquarks and gluons within a fast moving hadron. Generalised parton distributions are an extension of parton distributions. They additionally contain information about the distribution of the partons in the plane transverse to the direction in which the hadron is moving - this information is integrated out in the ordinary parton distributions. Generalised parton distributions (GPDs) are studied in a variety of exclusive scattering processes.

Guidal *et al.* have performed a calculation of the nucleon electromagnetic form factors using GPDs [GPRV04]. Their results for the electric form factor of the neutron and for the ratio G_E^p/G_M^p are in good agreement with experimental data, but the description of the magnetic form factors of both the proton and the neutron is not as precise, and misses a lot of the structure present in the form factors.

2.5 Dispersion Relations

Dispersion relations provide a powerful model-independent non-perturbative framework for the analysis of the electromagnetic structure of the nucleons simultaneously in both the spacelike and the timelike regions. In this section, a brief overview of the basic properties of analytic functions is presented, and dispersion relations for the nucleon form factors are introduced.

2.5.1 Some Properties of Analytic Functions

Analyticity is a strong constraint for functions of a complex variable. Let $f(x) = u(z) + iv(z)$ be a complex function of a complex variable z. In order for $f(z)$ to be complex-differentiable with respect to z, the derivative must be independent of the choice of direction with respect to which it is taken, since $z = x + iy$. This de-

mand leads to the well-known Cauchy-Riemann equations for complex-differentiable functions:

$$\begin{cases} du/dx = dv/dy\,, \\ du/dy = -dv/dx\,. \end{cases} \tag{2.16}$$

A complex function is analytic in a region $\mathcal{R}$ if it is complex differentiable at every point in $\mathcal{R}$, and the partial derivatives entering Eq. (2.16) exist. An important consequence is that if a function is analytic, so are all of its derivatives.

The real and imaginary parts of an analytic function are not arbitrary - they must satisfy the Cauchy-Riemann condition, Eq. (2.16). Therefore, if the real (imaginary) part of an analytic function is given, the imaginary (real) part is determined up to an additive constant. The relation between the real and imaginary parts of an analytic function can be further strengthened by applying the well-known Cauchy integration rules.

Points at which a function is not analytic are called singularities. Cauchy's theorem states that if a function $f(z)$ is an analytic function, continuous within and on a smooth contour $\mathcal{C}$, then

$$\oint f(z)dz = 0\,. \tag{2.17}$$

An important consequence of the Cauchy's theorem is the Cauchy integral formula, which states that

$$\oint_{\mathcal{C}} \frac{f(z)}{z-a}dz = 2\pi i f(a) \begin{cases} 1, & \text{if a is within } \mathcal{C}\,, \\ \frac{1}{2}, & \text{if a is on } \mathcal{C}\,, \\ 0, & \text{if a is outside } \mathcal{C}\,. \end{cases} \tag{2.18}$$

Cauchy's formula is a very powerful tool for the investigation of the properties of analytic functions - it shows the strong correlation between the values of the analytic function all over the complex plane. An important consequence of Cauchy's formula are the integral relations between the real and imaginary parts of an analytic function, which form the basis of dispersion relation techniques:

$$u(x,0) = \frac{1}{\pi}\mathcal{P}\int_{-\infty}^{+\infty} \frac{v(\xi,0)}{\xi - x}d\xi\,, \tag{2.19}$$

$$v(x,0) = -\frac{1}{\pi}\mathcal{P}\int_{-\infty}^{+\infty} \frac{u(\xi,0)}{\xi - x}d\xi\,.$$

Here $\mathcal{P}$ denotes the principal value of the integral.

2.5.2 Dispersion Relations for the Nucleon Form Factors

Dispersion relations are a powerful tool used to connect the absorptive and the dispersive behaviour of the nucleons. They have a long successful history of applications to the analysis of the structure of the nucleons [CKGZ58, FGT58, HP75,

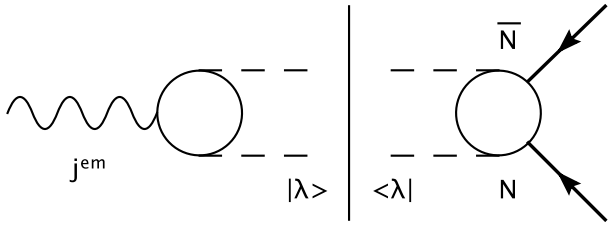

Figure 2.3: The spectral decomposition of the nucleon matrix element of the electromagnetic current $j_\mu^{\rm em}$.

HPSB76, MMD95, HMD96]. Based on unitarity and analyticity, dispersion relations connect the real and imaginary parts of the electromagnetic form factors of the nucleon. Assuming the convergence of an unsubtracted dispersion relation for the form factors, one can write for a generic form factor $F(t)$:

$$F(t) = \frac{1}{\pi} \int_{t_0}^{\infty} \frac{{\rm Im}F(t')}{t' - t - i\epsilon} dt' \,, \tag{2.20}$$

where t_0 is the threshold of the lowest cut of $F(t)$, and $i\epsilon$ defines the integral for values of t on the cut. Using Eq. (2.20) the electromagnetic structure of the nucleon can be related to its absorptive behaviour: the imaginary part Im F entering Eq. (2.20) can be obtained from a spectral decomposition [CKGZ58, FGT58]. For this purpose, it is convenient to consider the electromagnetic current matrix element in the timelike region:

$$J_\mu = \langle N(p)\overline{N}(\overline{p})|j_\mu^{\rm em}(0)|0\rangle = \overline{u}(p)\Big[F_1(t)\gamma_\mu + i\frac{F_2(t)}{2M}\sigma_{\mu\nu}(p+\overline{p})^\nu\Big]v(\overline{p}), \tag{2.21}$$

where p and $\overline{p}$ are the momenta of the nucleon and the antinucleon created by the current $j_\mu^{\rm em}$, respectively. The four-momentum transfer squared in the timelike region is $t = (p+\overline{p})^2$.

Using the Lehmann-Symanzik-Zimmermann (LSZ) reduction formalism, the imaginary part of the form factors is obtained by inserting a complete set of intermediate states [CKGZ58, FGT58] as schematically depicted on Figure 2.3:

$${\rm Im}J_\mu = \frac{\pi}{Z}(2\pi)^{3/2}\mathcal{N}\sum_\lambda \langle p|\bar{J}_N(0)|\lambda\rangle\langle\lambda|j_\mu^{\rm em}(0)|0\rangle v(\bar{p})\delta^4(p+\bar{p}-p_\lambda)\,, \tag{2.22}$$

where $\mathcal{N}$ is a nucleon spinor normalisation factor, Z is the nucleon wave function renormalisation, and $\overline{J}_N(x) = J^\dagger(x)\gamma_0$ with $J_N(x)$ a nucleon source:

$$(\partial\!\!\!/ + m)\psi(x) = J_N(x)\,, \tag{2.23}$$

where $\psi(x)$ is the nucleon field operator. This decomposition relates the spectral function to the on-shell matrix elements of other processes: the virtual photon first

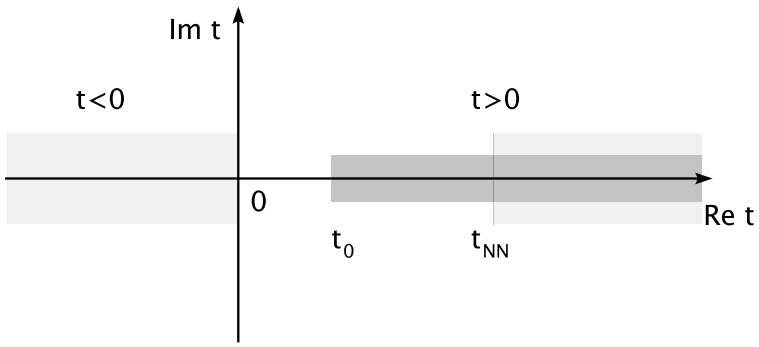

Figure 2.4: Schematic illustration of the analytic structure of the form factors in the complex t plane. The light shaded areas show the regions where the nucleon form factors are measured. The spacelike region corresponds to $t < 0$. It contains no cuts or poles. In the timelike region $t > 0$. The lowest cut opens at t_0. As will be discussed in the following Chapter, it corresponds to the two-pion cut for the isovector form factors, and the three-pion cut for the isoscalar form factors. In the timelike region, the form factors are measured at $t \geq t_{NN}$, where $t_{NN} = 4M_N^2$ is the threshold of nucleon-antinucleon production.

produces a certain on-shell intermediate state, which proceeds to interact with the nucleons.

Figure 2.4 shows a schematic illustration of the analytic structure of the nucleon form factors. The light shaded areas denote the regions where the form factors are measured. In the spacelike region, $t < 0$, no cuts or poles are present. The nucleon form factors in the spacelike region are measured in elastic electron-nucleon scattering experiments. In the timelike region, cuts corresponding to multi-particle exchange and poles corresponding to resonance contributions are present. The lowest cut opens at t_0. As detailed in the following Chapter, in the isovector channel $t_0 = 4M_\pi^2$ which corresponds to two-pion exchange. In the isoscalar channel, the lowest-mass contribution starts with the exchange of three pions and $t_0 = 9M_\pi^2$. These contributions generate an imaginary part of the form factors, which is related to the real part through the dispersion relation (2.20).

2.6 The Pion Cloud of the Nucleon

Before the advent of QCD, it was already well known that mesons play a key role in determining the properties of the nucleon interactions [Yuk35, FHK38] - the bare nucleon is surrounded by a meson cloud, and the pion, as the lightest meson, defines the longest-range part of the nuclear force. This concept was made more precise using dispersion theory in the 1950s [CKGZ58, FGT58]. Within the framework of pure vector meson dominance (VMD), the virtual photon first decays into a meson,

which in turn interacts with the nucleons. The lowest-mass vector mesons are the $\rho(770)$, $\omega(782)$ and $\phi(1020)$. In the timelike region, the process $e^+e^- \to hadrons$, these mesons show up as resonances for appropriate q^2 values, $q^2 > 0$. In the spacelike region, one therefore expects the interaction $eN \to eN$ to be dominated by these low-lying poles. For the form factors, this is reflected in the fact that the form factors in the spacelike region ($q^2 < 0$) are an analytic continuation of the form factors in the timelike region ($q^2 > 0$). Single pion exchange would provide the longest-range contribution to the interaction; however, as will be discussed in Section 3.1, single pion exchange is prohibited in the electromagnetic interaction, and the contribution starts with the two-pion exchange. In 1959, Frazer and Fulco wrote down partial wave dispersion relations that relate the nucleon electromagnetic structure to pion-nucleon scattering and predicted the existence of the ρ resonance [FF59, FF60b]. The two-pion contribution can be determined from experimental data. Information about the pion cloud of the nucleon can be extracted from the analysis of the two-pion contribution, although such an extraction is necessarily model-dependent.

The analysis of the nucleon form factors in terms of vector meson dominance allows to estimate important meson parameters. The meson-nucleon coupling constants can be determined; isospin violating effects directly enter the analysis through $\rho - \omega$ mixing. The analysis of specific low-Q^2 features of the nucleon form factors allows to estimate the possible mass regions where additional contributions would be required, and qualitative constraints on additional non-resonant contributions which are not explicitly included can be placed.

An analysis of the lowest-mass pionic contributions provides a means to determine the extent of the pion cloud of the nucleons. Additionally, an estimate of the strangeness content of the nucleons is made possible through an analysis of the coupling of the ϕ meson. The results for the ϕ coupling are based on a maximal violation of the OZI rule, however, since we assume the contribution to the isoscalar spectral function in the region of 1 GeV^2 to come entirely from the ϕ meson pole. In order to refine this analysis and provide more realistic values for the strangeness content of the nucleon, other contributions have to be considered [MMSO97].

In this framework, the size of the nucleons can also be extracted in a trivial way.

Chapter 3

The Theoretical Input

Certain contributions to the spectral functions can be constructed directly from experimental data. Additional contributions have to be parameterised. In this Chapter, the theoretical input for the spectral functions is discussed together with the constraints placed on the form factors.

3.1 The Spectral Functions

The states $|\lambda\rangle$ entering Eq. (2.22) are asymptotic states of momentum p_λ, and they carry the same quantum numbers as the current $j_\mu^{\rm em}$. The photon is a spin-1 particle odd under parity and charge conjugation, $J^{PC} = 1^{--}$. The isospin is not fixed, it can be $I = 0$ (isoscalar) or $I = 1$ (isovector). Combined with G-parity, defined as charge conjugation and a rotation in isospin space by 180^o around the 2nd axis I_2, the allowed intermediate states must possess the quantum numbers $(I^G)J^{PC} = 0^-(1^{--})$ or $1^+(1^{--})$. The exchange of a single pion is prohibited by charge conjugation: the electromagnetic current changes sign under the transformation, $J_\mu^{\rm em} \to -J_\mu^{\rm em}$, whereas a single pion state does not, $|\pi^0\rangle \to |\pi^0\rangle$, thus $\langle\pi^0|J_\mu^{\rm em}|0\rangle = 0$. Furthermore, a single pion has a total angular momentum $J = 0$, while $J = 1$ is required. The next lowest-mass state consists of two pions. The required angular momentum $J = 1$ corresponds to a relative P-state, which is odd under particle exchange; thus, in order to satisfy overall Bose symmetry, the state vector has to be odd in isospin space too, corresponding to $I = 1$. Generally, this follows from G-parity conservation - the contribution to the isovector channel comes from only even numbers of pions exchanged, and to the isoscalar channel only from odd numbers of pions exchanged.

3.1.1 Two-Pion Exchange

Already as early as in 1959, it was pointed out by Frazer and Fulco [FF59] that a pure vector meson dominance (VMD) approach is at odds with the general constraints of unitarity. In particular, in the isovector channel one notices a strong non-resonant contribution starting at $t_0 = 4M_\pi^2$ and extending all the way to the $\rho(770)$ peak. This contribution is due to the two-pion continuum, and arises from the projection of the nucleon born graphs, or, in modern language, the nucleon triangle diagram. This leads to a logarithmic singularity on the second Riemann sheet located at $t_c = 4M_\pi^2 - M_\pi^4/M_N^2 = 3.98M_\pi^2$, very close to the two-pion threshold. Neglecting this important unitarity contribution leads to a gross underestimate of the nucleon isovector radii.

The unitarity relation of Frazer and Fulco [FF59, FF60a, FF60b] determines the isovector spectral functions for the two-pion exchange contribution in terms of the pion form factor and the P-wave pion-nucleon scattering amplitudes:

$$\begin{aligned} \mathrm{Im}G_E(t) &= \frac{(t/4 - M_\pi^2)^{3/2}}{M_N\sqrt{t}} F_\pi(t)^* f_+^1(t) \\ \mathrm{Im}G_M(t) &= \frac{(t/4 - M_\pi^2)^{3/2}}{\sqrt{2t}} F_\pi(t)^* f_-^1(t) \end{aligned} \tag{3.1}$$

where $F_\pi(t)$ is the pion form factor, and $f_\pm^1(t)$ are the pion-nucleon scattering amplitudes.

Strictly, this relation gives the exact two-pion exchange contribution in the q^2 range starting from the two-pion threshold, $t_0 = 4M_\pi^2$, up to the four-pion channel threshold, $t = 16M_\pi^2$. However, the four-pion contribution is small up to $t \sim 50M_\pi^2$, which means the phase of $F_\pi(t)$ and $f_\pm^1(t)$ is the same in this region, and Eq. (3.1) is valid all the way up to $q^2 \sim 1$ GeV^2.

It is important to note that the pion-nucleon scattering amplitudes, $f_\pm^1(t)$, are required in the unphysical regime, $4M_\pi^2 \leq t \leq 4M_N^2$. This problem is solved by analytic continuation - a method used to extend the domain of definition of a given analytic function by performing a power series expansion with a sufficiently large radius of convergence. For a data set with no errors, the process of analytic continuation is unique. However, error bars on experimental measurements introduce an unavoidable ambiguity in the technique. Two independent analyses of analytical continuation of πN scattering amplitudes exist [Hoh83, Pie], however, and the final results obtained for the scattering amplitudes agree. A modern re-analysis of the πN scattering amplitudes with the inclusion of data collected since the works of Höhler and Pietarinen would be welcome.

With the availability of new high-precision data on the pion form factor from the CMD-2 [Akh99], KLOE [Alo04] and SND [Ach05] collaborations, we have re-analysed the two-pion contribution to the isovector nucleon form factors. A detailed report of this analysis is given in Section 6.1. It is important to note for

further discussion that the resulting two-pion contribution to the nucleon isovector form factors can be conveniently parameterised by a simple function of the form

$$F_i^{v,2\pi}(t) = \frac{a_i + b_i(1 - t/c_i)^{-2/i}}{2(1 - t/d_i)}\,, i = 1, 2, \tag{3.2}$$

where a_i, b_i, c_i and d_i are constants extracted from the full dispersion integrals.

3.1.2 $K\bar{K}$ exchange

The $K\bar{K}$ exchange contribution to the nucleon electromagnetic form factors has been evaluated in Ref. [HR99a, HR99b] from an analytic continuation of the KN scattering amplitudes. The $K\bar{K}$ contribution to the spectral functions is given by [HR99a, HR99b]

$$\begin{aligned} \mathrm{Im}F_1^{(s),K\bar{K}}(t) &= \mathrm{Re}\left\{ \left(\frac{M_N q_t}{4p_t^2} \right) \left[\frac{\sqrt{t}}{2\sqrt{2}M_N} b_1^{1/2,-1/2}(t) - b_1^{1/2,1/2}(t) \right] F_K(t)^* \right\}, \\ \mathrm{Im}F_2^{(s),K\bar{K}}(t) &= \mathrm{Re}\left\{ \left(\frac{M_N q_t}{4p_t^2} \right) \left[b_1^{1/2,1/2}(t) - \frac{\sqrt{2}M_N}{\sqrt{t}} b_1^{1/2,-1/2}(t) \right] F_K(t)^* \right\}, \end{aligned} \tag{3.3}$$

where $p_t = \sqrt{t/4 - M_N^2}$, $q_t = \sqrt{t/4 - M_K^2}$, $F_K(t)$ represents the kaon form factor, and $b_1^{1/2,\pm 1/2}$ are the $J = 1$ partial waves for $K\bar{K} \to N\bar{N}$.

In principle, a logarithmic singularity on the second Riemann sheet also exists in this case, located at $t_{c,K\bar{K}} = 4M_K^2 - M_K^4/M_N^2$. However, since the kaon is much heavier than a pion, this singularity is shifted further away from the two-kaon threshold. Additionally, the $K\bar{K}$ cut opens up at the $\phi(1020)$ mass, and is thus dominated by the ϕ peak from threshold. Therefore, it is possible to parameterise the contribution of the $K\bar{K}$ continuum to the nucleon form factors in terms of a simple pole at the ϕ mass with fixed residua as determined by a full analysis using Eq. (3.3) [HR99a, HR99b]:

$$F_i^{s,K\bar{K}}(t) = \frac{1}{\pi} \int\limits_{4M_K^2}^{\infty} \frac{\mathrm{Im}F_i^{s,K\bar{K}}(t')}{t' - t} dt' \approx \frac{a_i^{K\bar{K}}}{M_\phi^2 - t}, \quad i = 1, 2 \tag{3.4}$$

where $a_1^{K\bar{K}} = 0.1054$ GeV^2 and $a_2^{K\bar{K}} = 0.2284$ GeV^2. This form of the $K\bar{K}$ contribution is used in our analysis as a fixed contribution to the isoscalar spectral functions.

3.1.3 Correlated $\rho\pi$ exchange

It has been shown [JHS94] that the interaction between a pion and a ρ meson has a strong influence on the nucleon-nucleon interactions. The correlated $\rho\pi$ exchange

contribution has been calculated in Ref. [MMSO97] in the framework of the Bonn-Jülich model [Hol95]. The contribution to the nucleon form factors can be evaluated in terms of a dispersion integral, and the result can be conveniently parameterised with a fictious ω' pole, $M_{\omega'} = 1.12$ GeV [MMSO97]:

$$F_i^{s,\rho\pi}(t) = \frac{1}{\pi} \int\limits_{(M_\pi+M_\rho)^2}^{\infty} \frac{\mathrm{Im}F_i^{s,\rho\pi}(t')}{t'-t} dt' \approx \frac{a_i^{\rho\pi}}{M_{\omega'}^2 - t}, \quad i = 1,2 \tag{3.5}$$

where $a_1^{\rho\pi} = -1.01$ GeV^2 and $a_2^{\rho\pi} = -0.04$ GeV^2. This result is used on all our analysis as a fixed contribution to the form factors in the isoscalar channel.

3.1.4 One-Meson Exchange

In addition to the fixed continuum contributions discussed in the previous sections, contributions from vector mesons are parameterised in terms of vector meson poles. The two-pion continuum explicitly generates the contribution from the $\rho(770)$ meson, and thus no pole is required at the ρ mass. The next two low-mass mesons are the $\omega(781)$ and the $\phi(1020)$ mesons, which contribute to the isoscalar spectral functions. In our analysis, they are included as poles with a fixed mass, but their residua can vary. No further poles are allowed with a mass below ~ 1 GeV, and higher-mass poles are included to parameterise the contributions from the higher-mass resonances. Thus, the general structure of the spectral functions is:

$$\mathrm{Im}F_i^s(t) = F_i^{s,K\bar{K}}(t) + F_i^{s,\rho\pi}(t) + \sum_{V=\omega,\phi,s_1,\ldots} \pi a_i^V \delta(M_V^2 - t), \quad i = 1,2, \tag{3.6}$$

$$\mathrm{Im}F_i^v(t) = F_i^{v,2\pi}(t) + \sum_{V=v_1,v_2,v_3,\ldots} \pi a_i^V \delta(M_V^2 - t), \quad i = 1,2,$$

where M_V is the resonance mass, and a_i^V are the residua, related to the meson-nucleon coupling constants g_i^{VNN} by:

$$a_i^V = \frac{M_V^2}{f_V} g_i^{VNN}. \tag{3.7}$$

The coupling constants f_V are known from the widths of the leptonic decays $V \to e^+e^-$:

$$f_V = \alpha \sqrt{\frac{4\pi}{3} \frac{M_V}{\Gamma(V \to e^+e^-)}}, \tag{3.8}$$

with $\alpha = e^2/4\pi$ the fine structure constant.

We have investigated the possibility of using the Breit-Wigner form with an adjustable width instead of pole terms for the resonance contributions. This approach did not produce any sizeable improvement of our results, but drastically increased the number of free parameters. This has a negative effect on the mathematical stability of the problem. Instead, we have developed two models to account

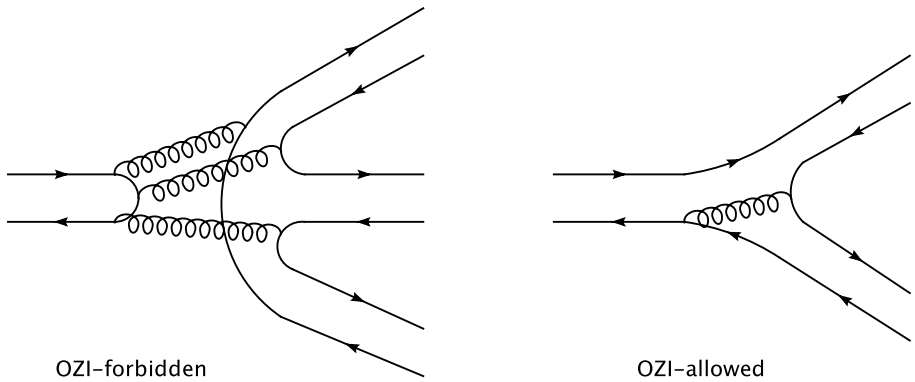

Figure 3.1: OZI-forbidden and OZI-allowed meson decay processes.

for the additional continuum contributions beyond the $\pi\pi$, $K\bar{K}$ and the $\rho\pi$ exchange contributions which are included explicitly. Both models generate an imaginary part of the form factors beyond the $N\bar{N}$ threshold in the timelike region. They are presented at the end of this Chapter.

3.1.5 The Okubo-Zweig-Iizuka rule

The Okubo-Zweig-Iizuka (OZI) rule was proposed independently by Okubo in 1963, Zweig in 1964 [Zwe64] and Iizuka in 1966. It states that in a meson decay, the quark-antiquark pair forming the meson does not annihilate into hard gluons. Instead, a quark-antiquark pair is produced from the vacuum. It recombines with the quark-antiquark pair from the meson, as schematically shown on Figure 3.1.

This rule imposes a restriction on the coupling of the ϕ meson to the nucleon. If the ϕ was composed only of a strange quark-antiquark pair - a pure $s\bar{s}$ state - and the nucleon had no strangeness component, a direct coupling of the ϕ to the nucleon would be forbidden. The only possible coupling would be through a $\phi \to K\bar{K}$ decay, with the $K\bar{K}$ pair subsequently coupling to the nucleon.

However, the ϕ meson is not a pure $s\bar{s}$ state - it has a small amount of the $u\bar{u} + d\bar{d}$ admixture, through which it can couple to the nucleon. The nucleon also has a small strangeness component. Therefore, a consequence of the OZI rule is the fact that the direct ϕ coupling to the nucleon must be small, and that the $K\bar{K}$ continuum contribution should account for the rest of the ϕ strength.

Thus, the inclusion of an explicit pole at the ϕ mass is not excluded in the VMD analysis, even with the inclusion of the $K\bar{K}$ continuum discussed in Section 3.1.2. The explicit coupling constant determined by such an analysis, in cases where the ϕ pole can unambiguously treated as a physical meson, can put constraints on the OZI-rule violating effects, and can be used in an analysis of the

strangeness content of the nucleons.

3.2 The Size of the Nucleon

At low momentum transfers, the electron probes the outer region of the nucleon charge distribution. Expanding a generic form factor, $F(Q^2)$, in this regime, the following expression is obtained:

$$F(Q^2) = F(0)\left(1 - \frac{1}{6}\langle r^2\rangle Q^2 + \mathcal{O}(Q^4)\right), \tag{3.9}$$

where $\langle r^2\rangle$ is called the mean square radius. Its definition stems from a non-relativistic description of the scattering process, in which a point-like particle interacts with a given charge distribution $\rho(r)$:

$$\langle r^2\rangle = \int_0^\infty 4\pi r^2\rho(r)dr = -\frac{6}{F(0)}\frac{dF(Q^2)}{dQ^2}\bigg|_{Q^2=0}. \tag{3.10}$$

Eq. (3.10) can be used for all form factors except F_1^n and G_E^n, which vanish in the limit $Q^2 \to 0$. In this case, the leading normalisation term in the expansion (3.9) is left out, and the definition of the mean square radius becomes

$$\langle r^2\rangle_E^n = -6\frac{dG_E^n(Q^2)}{dQ^2}\bigg|_{Q^2=0} \tag{3.11}$$

for the neutron charge radius. The same expression holds for $\langle r^2\rangle_1^n$ after replacing G_E^n with F_1^n. The slopes of G_E^n and F_1^n are related:

$$\frac{dG_E^n}{dQ^2}\bigg|_{Q^2=0} = \frac{dF_1^n}{dQ^2}\bigg|_{Q^2=0} - \frac{F_2^n(0)}{4M_N^2}, \tag{3.12}$$

where the second term on the right hand side of the equation is called the Foldy term. It gives the dominant contribution to the slope of G_E^n.

Thus, the analysis of the form factors of the nucleons provides a direct way to estimate the nucleon size. Alternative methods for the determination of the nucleon charge and magnetic radii exist, allowing to perform a comparison of the results of the form factor analysis to other determinations:

- Lamb shift measurements in hydrogen determine the proton charge radius with high precision: recent measurements [Bou96, Sch99] have been analysed in Ref. [Mel99]. The result of the analysis gives a value of $r_E^p = 0.883(14)$ fm.
- A recent re-analysis of the world data on elastic electron-nucleon scattering with the inclusion of Coulomb corrections provides a value for the proton magnetic radius [Sic03] $r_M^p = 0.855(35)$ fm.

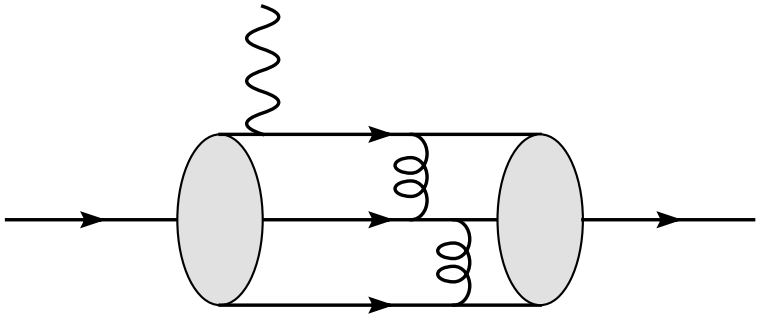

Figure 3.2: A schematic perturbative QCD picture for the interaction of the virtual photon with the nucleon at asymptotically large momentum transfers.

- A value for the neutron charge radius, $(r_E^n)^2 = -0.115(4)$ fm^2, has been derived in a recent re-evaluation of the ORELA experiment [KKRS97].
- Electron-deuteron scattering allows to determine the magnetic radius of the neutron. A recent analysis [Kub01] gives $r_M^n = 0.873(11)$ fm.

3.3 Perturbative QCD Constraints

At asymptotically large values of Q^2, perturbative QCD (pQCD) constrains the behaviour of the nucleon form factors - photons of sufficiently large virtuality see a nucleon consisting of three quarks moving collinear with the nucleon. In order for the momentum of the virtual photon to be distributed evenly between the quarks, gluon exchanges are required, as schematically depicted on Figure 3.2. For the scaling behaviour, Brodsky and Lepage find [LB80]:

$$F_i(t) \underset{Q^2\to\infty}{\longrightarrow} \frac{1}{Q^{2(i+1)}} \Big[\ln\Big(\frac{Q^2}{Q_0^2}\Big)\Big]^{-\gamma}, \quad i = 1, 2, \tag{3.13}$$

where $Q_0 \simeq \Lambda_{QCD}$, and the anomalous dimension $\gamma \approx 2$ depends weakly on the number of flavours [LB80].

The leading power scaling of the form factors can be easily understood in terms of gluon exchange. The propagator associated with the exchange of a single gluon is proportional to $1/Q^2$. Thus, the helicity conserving Dirac form factor $F_1(Q^2)$ scales roughly as $1/Q^4$, since two gluon exchanges are required. The Pauli form factor $F_2(Q^2)$ involves a helicity flip between the initial and final nucleons, which requires the exchange of another gluon. Thus, its leading power scaling behaviour is $1/Q^6$.

The asymptotic behaviour of the form factors has recently been studied in connection with the unexpected behaviour of the ratio $Q^2F_2(Q^2)/F_1(Q^2)$ measured

at Jefferson Lab [JLAB00, JLAB01] shown on Figure 3.3: the ratio $QF_2(Q^2)/F_1(Q^2)$ is constant for $Q^2 \geq 1.5$ GeV^2, and not $Q^2F_2(Q^2)/F_1(Q^2)$ as one expects from the pQCD prediction (3.13). Two new independent analyses predict different logarithmic corrections [BJY02, RJ03]. Although the experimental data for the current range of Q^2 values does not suggest the onset of asymptotic pQCD behaviour, our analysis includes the leading power constraints on the form factors. This guarantees the correct asymptotics, and allows to estimate the order of magnitude of the Q^2 values where the pQCD behaviour of the form factors becomes evident.

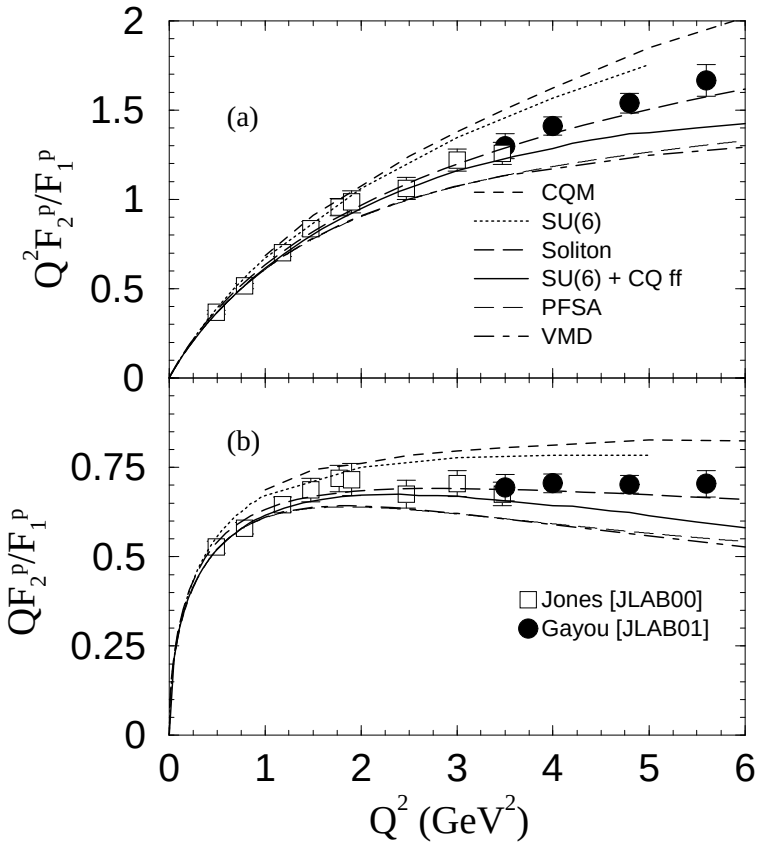

Figure 3.3: The ratios $QF_2^p(Q^2)/F_1^p(Q^2)$ and $Q^2F_2^p(Q^2)/F_1^p(Q^2)$ measured at JLab [JLAB00, JLAB01]. Figure taken from [JLAB01]. Our definition of the form factors differs from the conventions of [JLAB00, JLAB01] by a normalisation factor κ_p. The lines indicate the different model predictions.

In order to obtain the correct leading power behaviour,

$$F_1(t) \underset{t\to\infty}{\longrightarrow} \frac{1}{t^2}\,, \qquad F_2(t) \underset{t\to\infty}{\longrightarrow} \frac{1}{t^3}\,, \tag{3.14}$$

terms up to order $1/t$ must cancel in the expansion of $F_i(t)$, $i = 1, 2$, in the limit

$t \to \infty$. For $F_2(t)$, terms at order $1/t^2$ must also vanish. Written in terms of the spectral functions, these conditions dictate:

$$\int_{t_0}^{\infty} \mathrm{Im}F_i(t) t^n dt = 0, \quad i = 1, 2, \tag{3.15}$$

with $n = 0$ for F_1 and $n = 0, 1$ for F_2.

The pQCD constraints can be included in different ways. A previous analysis [MMD95] also included the logarithmic corrections. The way they were implemented, however, lead to an unphysical singularity in the timelike region. Instead, we have constructed two models which parameterise the contributions from continua which are not included explicitly and which enforce the correct leading power pQCD scaling behaviour. Both models are discussed in detail in the following sections.

3.3.1 The Superconvergence Approach

The constraint dictated by Eq. (3.15) can be directly translated into constraints on the parameters of the resonance poles included in the analysis - the superconvergence relations. In a pure VMD approach, where the form factor is given by

$$F(t) = \sum_V \frac{a^V}{M_V^2 - t}\,, \tag{3.16}$$

the $1/t$ expansion gives:

$$F(t) = -\sum_V a^V \left(\frac{1}{t}\right) - \sum_V a^V M_V^2 \left(\frac{1}{t^2}\right) - \sum_V a^V M_V^4 \left(\frac{1}{t^3}\right) + \ldots \tag{3.17}$$

The requirement that the leading terms up to order $1/t$ vanish places the constraint on the residua of the resonance poles:

$$\sum_V a^V = 0\,. \tag{3.18}$$

For the Pauli form factors, terms up to order $1/t^2$ must vanish, leading to an additional constraint:

$$\sum_V a^V M_V^2 = 0\,. \tag{3.19}$$

These constraints hold for the isoscalar form factors, since the $K\bar{K}$ and the correlated $\rho\pi$ exchange processes are parameterised in terms of simple meson poles. For the isovector form factors, however, the two-pion contribution has a more complicated functional form, given in Eq. (3.2). By performing an expansion in powers of t in

the limit $t \to \infty$, the superconvergence relations for the isovector form factors can be derived. Using Eq. (3.2), they have the following form:

$$\begin{aligned} \frac{a_1 d_1}{2} + \sum_V a^V &= 0 \qquad \text{for } F_1^v, \\ \left.\begin{aligned} \frac{a_2 d_2}{2} + \sum_V a^V &= 0 \\ \frac{a_2 d_2^2 - b_2 c_2 d_2}{2} + \sum_V a^V M_V^2 &= 0 \end{aligned}\right\} &\quad \text{for } F_2^v \,. \end{aligned} \tag{3.20}$$

In addition, we add a very broad resonance to both the isoscalar and the isovector form factors. This contribution has the structure

$$F_i^{I,\text{broad}}(t) = \frac{a_i^I (M_I^2 - t)}{(M_I^2 - t)^2 + \Gamma_I^2} \,, i = 1, 2, \; I = s, v. \tag{3.21}$$

It parameterises weak continuum contributions in addition to the explicitly included two-pion, $K\bar{K}$ and $\rho\pi$ continua, and generates an imaginary part of the spectral functions in the timelike region for $t \geq 4M_N^2$. The width-like parameter Γ_I [GeV^2] is very large, of the same order of magnitude as M_I^2. A typical value is $\Gamma_I \sim 10$ GeV^2. Thus, Eq. (3.21) is only a convenient parameterisation of continua - it must not be understood as a physical resonance. The broad resonance contributions are also accounted for in the superconvergence relations.

It is convenient to write down the complete set of superconvergence relations as a set of linear equations for the resonance pole residua in matrix form, additionally enforcing the correct form factor normalisation dictated by Eq. (2.10). For the Dirac form factors, the normalisation conditions and the superconvergence relations fix the residua of two resonances. For the Pauli form factors, the additional superconvergence relation allows to fix the residua of a third resonance. Without loss of generality, the linear equations can be written down for the residua of two (three) lowest-mass resonance poles for the Dirac (Pauli) form factors, respectively. Thus, the set of linear equations takes the form

$$\begin{aligned} \begin{pmatrix} M_{I_1}^{-2} & M_{I_2}^{-2} & M_{I_3}^{-2} \\ 1 & 1 & 1 \end{pmatrix} \begin{pmatrix} a_1^{I_1} \\ a_1^{I_2} \end{pmatrix} &= \vec{C}_1^I \,, \\ \begin{pmatrix} M_{I_1}^{-2} & M_{I_2}^{-2} & M_{I_3}^{-2} \\ 1 & 1 & 1 \\ M_{I_1}^2 & M_{I_2}^2 & M_{I_3}^2 \end{pmatrix} \begin{pmatrix} a_2^{I_1} \\ a_2^{I_2} \\ a_2^{I_3} \end{pmatrix} &= \vec{C}_2^I \,, \\ I = s, v \,, \end{aligned} \tag{3.22}$$

where

$$\vec{C}_1^I = \begin{pmatrix} F_1^I(0) - \sum_{k>2} \frac{a_1^{I_k}}{M_{I_k}^2} - \frac{a_1^{I_{\text{broad}}} M_{I_{\text{broad}}}^2}{M_{I_{\text{broad}}}^4 + \Gamma_{I_{\text{broad}}}^2} - \delta_{I,v} \frac{a_1+b_1}{2} \\ - \sum_{k>2} a_1^{I_k} - \delta_{I,v} \frac{a_1 d_1}{2} \end{pmatrix} \tag{3.23}$$

$$\vec{C}_2^I = \begin{pmatrix} F_2^I(0) - \sum_{k>3} \frac{a_2^{I_k}}{M_{I_k}^2} - \frac{a_2^{I_{\text{broad}}} M_{I_{\text{broad}}}^2}{M_{I_{\text{broad}}}^4 + \Gamma_{I_{\text{broad}}}^2} - \delta_{I,v} \frac{a_2+b_2}{2} , \\ - \sum_{k>3} a_2^{I_k} - \delta_{I,v} \frac{a_2 d_2}{2} \\ - \sum_{k>3} a_2^{I_k} M_{I_k}^2 - \delta_{I,v} \left(\frac{a_2 d_2^2}{2} - \frac{b_2 c_2 d_2}{2} \right) \end{pmatrix} , \quad I = s, v \, . \tag{3.24}$$

These equations constrain 10 parameters in total: two residua for each of F_1^s and F_1^v and three residua for each of F_2^s and F_2^v.

3.3.2 The Explicit pQCD Approach

An alternative approach to enforcing pQCD behaviour is the addition of an explicit term compatible with Eq. (3.13). Superconvergence relations are still enforced in order to cancel the leading powers in the $1/t$ expansion, but, generally, no broad resonance is added. We have chosen terms of the form:

$$F_i^{I,\text{pQCD}} = \frac{a_i^I}{1 - c_i^2 t + b_i^2 (-t)^{i+1}} \, , i = 1, 2, \quad I = s, v. \tag{3.25}$$

Such a term behaves like an effective resonance pole for low values of t, and explicitly enforces pQCD behaviour for large values of t.

The parameters b_i and c_i are the same for the isoscalar and isovector form factors, while the residua a_i^I depend on the channel. This method allows for a smooth interpolation between the low-t and the high-t regions.

Another important consequence of this approach to enforcing the pQCD constraints is the investigation of the onset of pQCD behaviour. Perturbative QCD can not predict the scale at which the asymptotic behaviour should become evident in experiment. Non-perturbative tools are required for such an analysis, and dispersion relations provide this opportunity.

In order to provide predictions for the Q^2 values where the asymptotic behaviour sets on, we investigate the ratio $R(Q^2) = Q^2 F_2^p(Q^2)/F_1^p(Q^2)$. Numerically, it can be constructed directly from our form factor analyses. However, there is a difference between the expectations for the results of the SC and the pQCD approaches.

Analytically, finding the onset of pQCD behaviour amounts to solving

the following equation:

$$\frac{dR(Q^2)}{dQ^2} = 0 \tag{3.26}$$

for Q^2. In a pure VMD approach, where the form factors are given by (3.16), the solution of Eq. (3.26) yields a denominator of the form:

$$Q^2_{\mathrm{pQCD}} \sim (\sum_V a_1^V \sum_V a_2^V)^{-1} \,. \tag{3.27}$$

Due to the pQCD constraints on the residua (3.18), the denominator vanishes. Similar structures appear in the numerator of the solution, therefore Q^2_{pQCD} remains finite, but one expects large estimates for Q^2_{pQCD} within the SC approach. The pQCD terms, however, are not bound by superconvergence relations, since they provide the correct asymptotic behaviour by construction. The solution of Eq. (3.26) depends on free parameters - the pQCD term parameters a_i^I, b_i and c_i. The pQCD approach is therefore expected to provide a more realistic estimate of the onset of pQCD behaviour.

Chapter 4

Cross Section Analysis

In this Chapter, the problem of the extraction of the form factors from experimental data for both elastic and inelastic scattering is discussed. Radiative corrections applied to the cross section measurements are introduced. The discrepancy between the Rosenbluth and the polarisation transfer techniques is discussed on the basis of the two-photon corrections.

4.1 Rosenbluth Separation

Before the advent of polarisation transfer experiments, our knowledge about the nucleon form factors came almost exclusively from elastic *ep* scattering experiments. The form factors were extracted from the differential cross section measurements using the Rosenbluth formula for the differential cross section [Ros50]:

$$\frac{d\sigma}{d\Omega} = \left(\frac{d\sigma}{d\Omega}\right)_{\text{Mott}} \frac{\tau}{\epsilon(1+\tau)}[G_M^2(Q^2) + \frac{\epsilon}{\tau}G_E^2(Q^2)]\,, \tag{4.1}$$

where $\epsilon = (1 + 2(1+\tau)\tan^2(\theta/2))^{-1}$ is the virtual photon polarisation and θ is the scattering angle.
The Mott cross section for the scattering from a point particle is:

$$\left(\frac{d\sigma}{d\Omega}\right)_{\text{Mott}} = \frac{\alpha^2 E' \cos^2(\theta/2)}{4E^3 \sin^4(\theta/2)}\,, \tag{4.2}$$

where E and E' are the energies of the initial and scattered electron, respectively, and $\alpha = e^2/4\pi$ is the electromagnetic fine structure constant.

Because the form factors in Eq. (4.1) are functions of Q^2 only, by performing measurements at a fixed Q^2 for different values of ϵ it is possible to extract

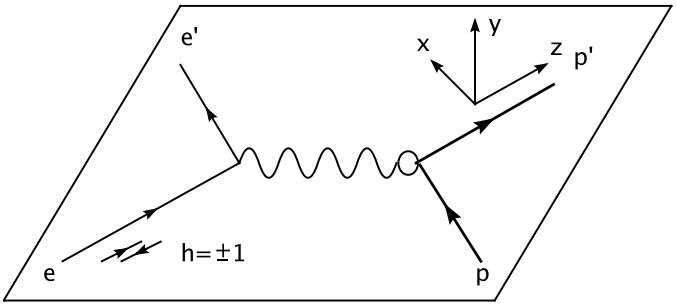

Figure 4.1: The kinematics for the polarisation transfer experiments. A longitudinally polarised electron scatters on a proton with the exchange of a virtual photon.

G_M^2 from the cross section measured at $\epsilon = 0$, and the ratio G_E/G_M from the slope in ϵ.

Similar measurements for the neutron form factors are nearly impossible. The contribution of G_E^n to the differential cross section is very small. It provides only $\sim$ 5% of the en cross section. In addition, the absence of a free neutron target is a strong limitation. The experiments on a deuterium target produce large uncertainties due to the corrections for ep scattering, as well as corrections for nuclear effects in deuterium.

4.2 Polarisation Transfer Separation

In 1968, Akhiezer and Rekalo [AR68] pointed out the possibility of using a polarised electron beam scattering on a nucleon target to obtain the nucleon form factors by measuring the polarisation of the recoiling nucleon. The kinematics for such a scattering process are schematically shown on Figure 4.1. In a further review paper [AR74] they discussed the possibility of obtaining G_E^p in the presence of a dominant G_M^p from the reaction $\vec{e}p \rightarrow e\vec{p}$ at large momentum transfers. In 1982, Arnold, Carlson and Gross [ACG80] presented the methods for the measurement of the neutron form factors in the reaction $^2H(\vec{e}, e'\vec{n})p$.

For the scattering of longitudinally polarised electrons off an unpolarised target, there are only two non-zero polarisation components for the recoil nucleon: transverse P_x and longitudinal P_z. For a 100% longitudinally polarised electron beam, they are related to the electric and magnetic form factors [ACG80]:

$$I_0 P_x = -2\sqrt{\tau(1+\tau)} G_E G_M \tan(\theta/2)\,, \tag{4.3}$$
$$I_0 P_z = \frac{1}{M_N}(E+E')\sqrt{\tau(1+\tau)} G_M^2 \tan^2(\theta/2)\,,$$

where $I_0 = G_E^2(Q^2) + \frac{\tau}{\epsilon} G_M^2(Q^2)$. Thus, the longitudinal and transverse polarisation

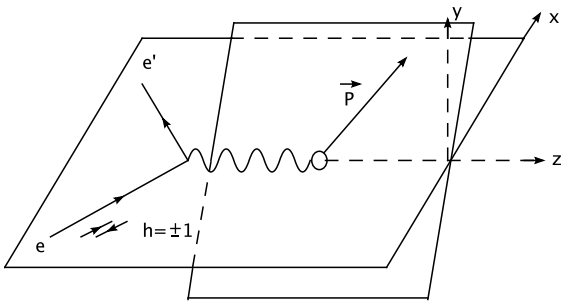

Figure 4.2: The kinematics for the double polarisation transfer experiments. A longitudinally polarised electron scatters on a polarised proton with the exchange of a virtual photon.

components are proportional to G_M^2 and $G_E G_M$, respectively. The ratio of the form factors in polarisation transfer experiments is given by:

$$\frac{G_E}{G_M} = -\frac{P_x}{P_z}\frac{(E+E')}{2M_N}\tan(\theta/2)\,. \tag{4.4}$$

Another possibility for measuring the form factors with polarisation transfer techniques was discussed in 1969 by Dombey [Dom69]. He proposed double polarisation experiments: the scattering of longitudinally polarised electrons on a polarised nucleon target. The kinematics for the process are schematically depicted on Figure 4.2. Donnelly and Raskin [DR85, RD88] related the measurable asymmetry for two different beam helicities to the ratio of the electric and magnetic form factors:

$$A = -\frac{A_1 G_E G_M + A_2 G_M^2}{G_E^2 + \tau(1+2(1+\tau)\tan^2(\theta/2))G_M^2}\,, \tag{4.5}$$

where A_1 and A_2 depend on the kinematical variables and the orientation of the nucleon polarisation vector $\vec{P}$ with respect to the scattering plane, and

$$A = \frac{\sigma_+ - \sigma_-}{\sigma_+ + \sigma_-}\,. \tag{4.6}$$

The cross sections σ_+ and σ_- correspond to the two different beam helicities. The asymmetry in parallel kinematics, where the momentum transfer vector $\vec{q}$ is parallel to the target polarisation vector, is proportional to the nucleon's magnetic form factor squared. The asymmetry in perpendicular kinematics, where the momentum transfer vector is perpendicular to the target polarisation vector, is proportional to the product $G_E G_M$.

The polarisation transfer techniques provide several advantages over the Rosenbluth separation method:

- If the polarisations can be measured simultaneously, only one measurement at a given Q^2 is required. This reduces systematic errors associated with angle and beam energy changes.

- For the extraction of the ratio G_E/G_M the knowledge of the beam polarisation is not required.
- Two-photon effects are suppressed. A discrepancy exists between the Rosenbluth and the polarisation transfer form factor extraction, which may be explained by two-photon physics. This topic is discussed in detail in Section 4.4.

4.3 Radiative Corrections

With the advent of the new continuous beam electron accelerators such as CEBAF (Jefferson laboratory), ELSA (Bonn) and MAMI (Mainz), a large amount of high precision data on the cross sections for electron-nucleon scattering has become available. It is therefore clear that if meaningful results are to be obtained for the nucleon form factors, one has to take into account effects higher order in the fine structure constant α than the one-photon exchange approximation. Depending on the experimental conditions - initial beam energy, momentum transfer and detector resolution, the radiative corrections can be as large as 30% of the uncorrected cross section. These corrections include the QED processes of radiation of an unobserved real photon, vacuum polarisation, lepton-photon vertex corrections and the two-photon exchange box diagrams. The set of elastic diagrams to be considered is shown on Fig. 4.3, and the inelastic diagrams are shown on Fig. 4.4.

Another important reason to study the higher order corrections carefully is the apparent discrepancy between the form factors extracted using the Rosenbluth and the polarisation transfer techniques. World data on the ratio $\mu_p G_E^p/G_M^p$ is shown on Figure 4.5. The apparent discrepancy between the two approaches has been a subject of intense discussion in recent years, leading to fundamental questions regarding the validity of one of the techniques.

When the discrepancy in Figure 4.5 was first observed, it was noted that the values of G_E^p extracted using the Rosenbluth separation technique are not consistent with each other. It was often assumed that the difference between the two techniques can therefore be explained by systematic uncertainties in the Rosenbluth extractions. This scattering of values is largely explained by the fact that new experiments extracted the data from a combination of the new cross section measurements and older results. The normalisation uncertainties arising from such a treatment were often neglected. A global reanalysis of the Rosenbluth data [Arr03] showed that only the data from individual measurements are consistent. Nevertheless, the results of the global data analysis still disagreed with the polarisation transfer results. This lead to speculations of a fundamental problem with either the Rosenbluth, or the polarisation transfer methods. Currently, this discrepancy is believed to be due to hard two-photon exchange corrections, discussed in detail in Section 4.4.

Several independent analyses of the radiative corrections exist. Schwinger

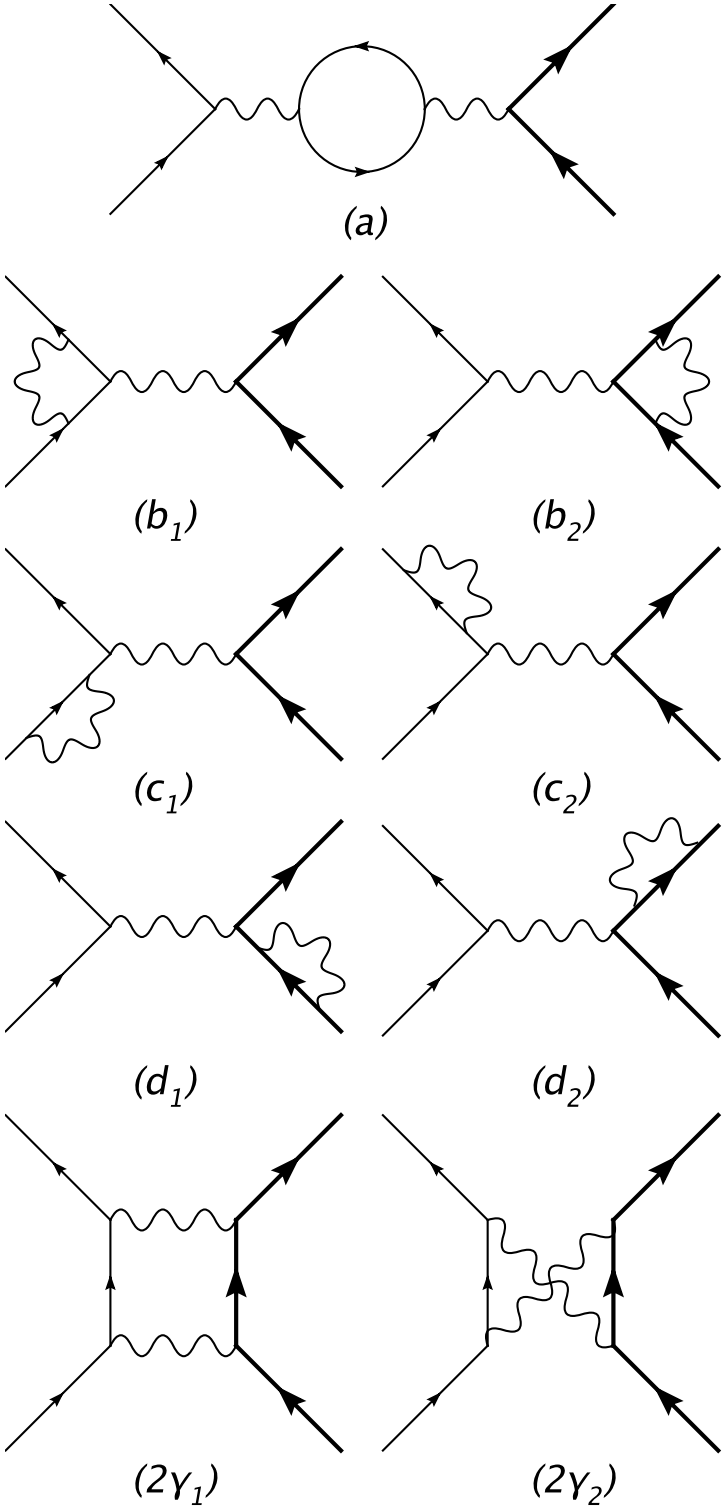

Figure 4.3: Feynman diagrams for elastic amplitudes contributing to the radiative corrections: vacuum polarisation (a), vertex corrections (b_1, b_2), self-energy corrections (c_1, c_2, d_1, d_2) and two-photon exchange corrections ($2\gamma_1, 2\gamma_2$).

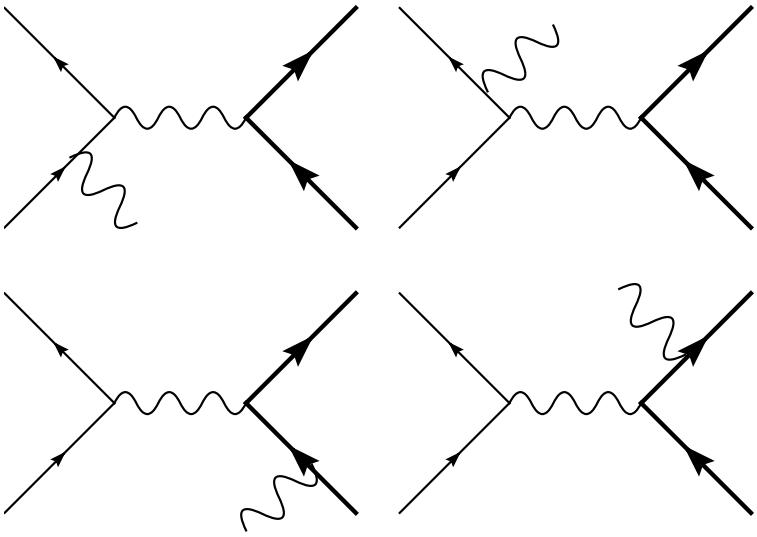

Figure 4.4: Feynman diagrams for inelastic amplitudes contributing to the radiative corrections (Bremsstrahlung).

related the corrected and uncorrected cross sections by a factor of $(1 + \delta)$ [Sch49]:

$$\left(\frac{d\sigma}{d\Omega}\right)_{\text{measured}} = \left(\frac{d\sigma}{d\Omega}\right)_{\text{Born}} (1 + \delta)\,. \tag{4.7}$$

In 1961, Tsai [Tsa61] calculated the contributions from a subset of the diagrams contributing to the radiative corrections for ep scattering neglecting any effects of the structure of the proton. His calculation was applicable to experiments in which only the scattered electrons are detected. Meister and Yennie [MY63] performed a calculation for the case when either, but not both, outgoing particles are detected. In 1969, Mo and Tsai [MT68] extended the original calculation of Ref. [Tsa61]. They compared the result to the result of Meister and Yennie, finding very good agreement. The result given by Mo and Tsai has been applied to almost all experimental data for the unpolarised cross section measurements.

Both of these calculations involve both purely mathematical and physical approximations. The mathematical approximations are made in order to perform the integrations. The physical ones reflect a more complex underlying problem which appears for all diagrams. We discuss this problem using the two-photon diagrams, since two-photon effects beyond the ones included in the calculations discussed so far have been shown to have a large effect on the cross section analysis.

The matrix elements of the box and crossed box diagrams of Figure 4.3 are:

$$M^{2\gamma} = e^4 \int \frac{d^4k}{(2\pi)^4} \left[\frac{N_a(k)}{D_a(k)} + \frac{N_b(k)}{D_b(k)}\right], \tag{4.8}$$

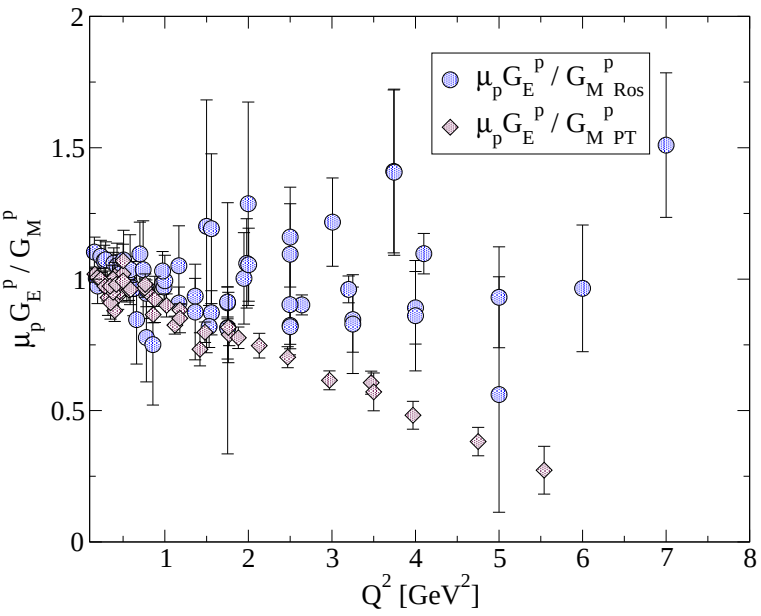

Figure 4.5: World data on the ratio $\mu_p G_E^p / G_M^2$. The circles are the data obtained using the Rosenbluth separation technique. The diamonds are the data obtained using the polarisation transfer technique. The apparent discrepancy between the two techniques has been a subject of intense investigation in recent years, and may be explained by two-photon exchange effects.

where the numerators are

$$N_a(k) = \overline{u}(p_3)\gamma_\mu(\not{p}_1 - \not{k})\gamma_\nu u(p_1)\overline{u}(p_4)\Gamma^\mu(q-k)(\not{p}_2 + \not{k} + M)\Gamma^\nu(k)u(p_2), \quad (4.9)$$
$$N_b(k) = \overline{u}(p_3)\gamma_\nu(\not{p}_3 + \not{k})\gamma_\mu u(p_1)\overline{u}(p_4)\Gamma^\mu(q-k)(\not{p}_2 + \not{k} + M)\Gamma^\nu(k)u(p_2),$$

and the denominators are the products of the scalar propagators,

$$D_a(k) = [k^2 - \lambda^2][(k-q)^2 - \lambda^2][(p_1 - k)^2 - m^2][(p_2 + k)^2 - M^2], \quad (4.10)$$
$$D_b(k) = [k^2 - \lambda^2][(k-q)^2 - \lambda^2][(p_3 + k)^2 - m^2][(p_2 + k)^2 - M^2].$$

Here λ is an infinitesimal photon mass introduced in order to regulate the infrared divergences.

The current $\Gamma^\mu(k)$ entering Eq. (4.9) involves the form factors of the nucleons. It is given in Eq. (2.9). This creates a tautology, since these corrections are used to determine the experimental form factors. Ideally, a dynamic analysis of the form factors could be performed - i.e. the corrections corresponding to a given phenomenological form of the form factors would be computed for each variation of the form factors. The numerical complexity associated with the evaluation of these diagrams, especially the two-photon exchange diagrams, however, makes such an approach not feasible.

In the calculations discussed so far, the effects of the structure of the nucleon were neglected. In a recent re-evaluation of these corrections, Maximon

and Tjon [MT05] have considered the effects of the finite size of the nucleon and removed the mathematical approximations of the original calculation of Mo and Tsai. They found deviations for δ at the 2% order. However, their treatment of the two-photon box and crossed-box diagrams still employs the soft-photon exchange approximation: the detailed effects of the nucleon structure are neglected.

Another important contribution to the radiative corrections are the Coulomb corrections. They arise due to the distortion of the electron scattering waves in the Coulomb field of the proton. In terms of Feynman diagrams, this corresponds to multiple photon exchange between the electron and the proton. The soft photon parts of the two-photon diagrams of Figure 4.3 are a subset of the Coulomb corrections. Therefore, the soft contributions have to be subtracted from the calculations of the Coulomb corrections in order to avoid double counting. Ingo Sick has provided us with numerical results for the Coulomb corrections [Sic06] which we apply to the experimental data for the cross sections in our analyses.

Since the independent calculations with increasing levels of precision agree within a few percent accuracy, a rigorous evaluation of the effects of the two-photon exchange which have been neglected in the calculations discussed has become necessary.

4.4 Two-Photon Exchange

Several recent investigations of the magnitude of the two-photon effects have been performed. In [ABCC05, CABC04], a calculation of the two-photon exchange corrections is performed within the framework of generalised parton distributions. The authors find that the calculated correction only partially resolves the discrepancy between the Rosenbluth and the polarisation transfer techniques. Their result in comparison to the world data on the ratio $\mu_p G_E^p / G_M^p$ is shown on Figure 4.6.

Blunden, Melnitchouk and Tjon have performed a direct analysis of the two-photon box and crossed-box diagrams. Their first analysis [BMT03] included only a proton intermediate state and approximated the proton form factors required for the calculation by a simple monopole. It was further extended to parameterise the form factors with a sum of monopoles [BMT05], and include the contribution of the Δ intermediate state [KBMT05]. The parameterisation of the form factors introduces an unavoidable model dependence into such a calculation.

The results of the calculated corrections applied to the form factor ratio are shown on Figure 4.7. Again, the authors find that the calculated corrections only partially resolve the disagreement between the Rosenbluth and polarisation transfer techniques. Their result is comparable in magnitude to the result of Afanasev *et al.* [ABCC05, CABC04].

In the same analysis, the two-photon effects for the polarisation transfer

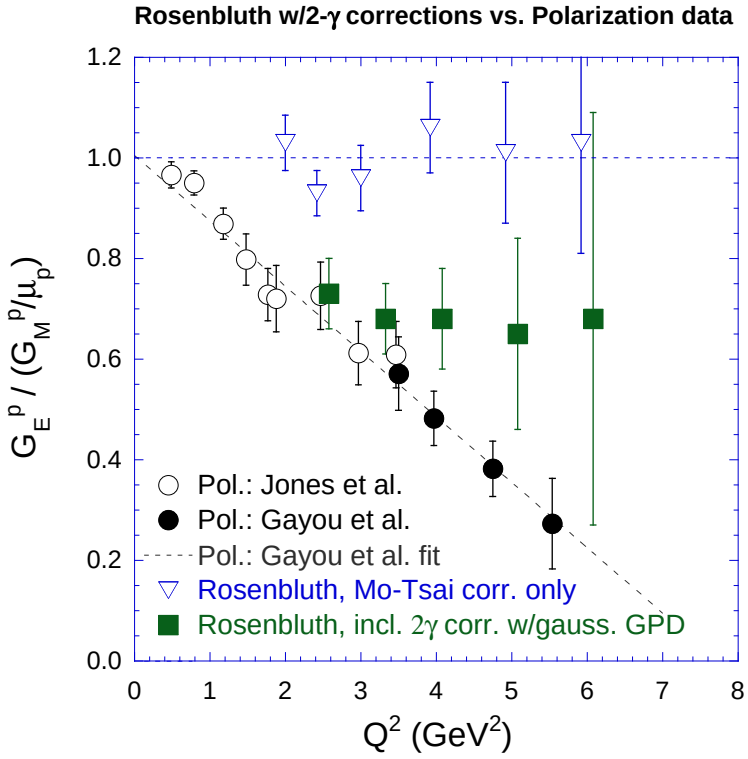

Figure 4.6: The result of Afanasev *et al.* [ABCC05, CABC04] applied to the ratio of the electric and magnetic form factors of the proton in comparison to the world data. Figure taken from Ref. [ABCC05]. The hollow and filled circles show the polarisation transfer results. The hollow triangles show the Rosenbluth technique results. The filled squares are the results obtained after the calculated missing two-photon effect corrections are applied to the Rosenbluth data.

techniques are found to be negligible in magnitude.

We have performed a model-independent estimate of the two-photon corrections by comparing the analysis of the polarisation transfer data to a direct analysis of the elastic unpolarised electron-proton scattering differential cross section data. Assuming the cross section obtained from the form factors measured with polarisation transfer techniques is free of two-photon corrections, as suggested in [BMT05], the difference between it and the unpolarised cross section provides a prediction for the missing two-photon corrections. The results are presented and discussed in detail in Section 7.2.

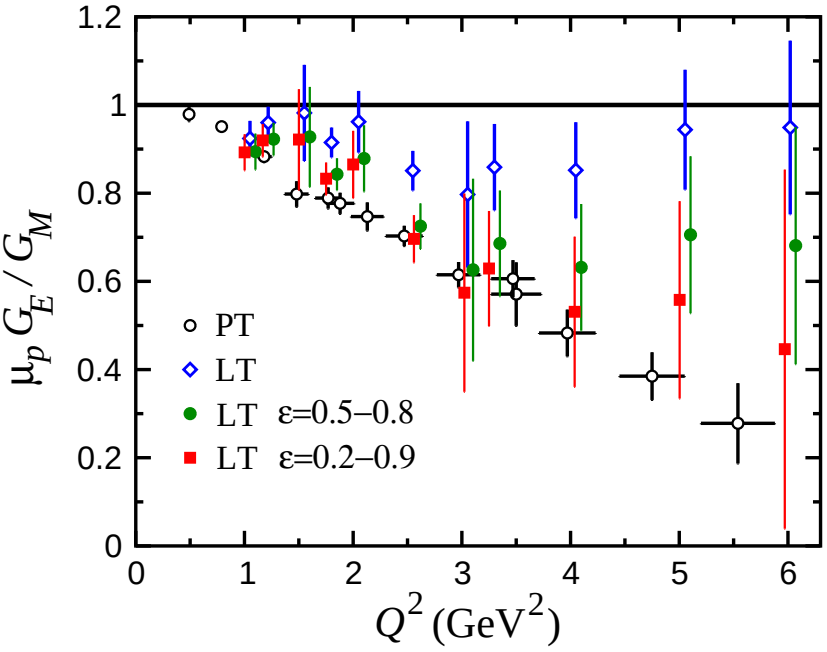

Figure 4.7: The result of Blunden, Melnitchouk and Tjon [BMT05, KBMT05] applied to the ratio of the electric and magnetic form factors of the proton in comparison to the world data. The hollow diamonds are the results of the Rosenbluth analyses, the hollow circles are the results of polarisation transfer experiments. The filled squares and the filled circles show the Rosenbluth results corrected for the calculated two-photon exchange under two different assumptions. Figure taken from Ref. [BMT05].

4.5 Inelastic Scattering

In the timelike region, several scattering processes can be used in order to measure the form factors. For example, the cross section for the process $p\bar{p} \to e^+e^-$ without kinematic prefactors is given by:

$$\frac{d\sigma}{d\Omega} \sim |G_M^p|^2(1+\cos^2(\theta)) + \frac{4M_p^2}{s}|G_E^p|^2\sin^2(\theta)\,. \tag{4.11}$$

Additional Coulomb terms are included in the cross section analysis [Tza70] in order to account for the final state nucleon interactions. These corrections make the cross section non-zero at threshold.

The PS 170 experiment by the LEAR collaboration measured the proton magnetic form factor in the timelike region in the reaction $p\bar{p} \to e^+e^-$ [Bar94]. The reaction $p\bar{p} \to e^+e^-$ was further measured in the E835 experiment [Amb99]. The

BABAR collaboration [Aub05] used the process $e^+e^- \to p\bar{p}\gamma$. The DM2 collaboration [Bis90] measured the proton magnetic form factor in the process $e^+e^- \to p\bar{p}$. Only one measurement of the neutron form factor in the timelike region exists. The pioneering FENICE experiment [Ant93] measured the neutron magnetic form factor in the reaction $e^+e^- \to n\bar{n}$.

The expressions for the cross sections for these reactions do not provide a simple way to separate the electric and the magnetic form factors. For example, in Eq. (4.11) both G_E^p and G_M^p enter with angular dependent prefactors. Therefore, in order to extract the form factors from the measured cross sections, assumptions are made. The form factors are extracted either assuming $|G_E^p| = 0$, or $G_E^p = G_M^p$. This limitation can be overcome only if an analysis of the differential cross section data in the timelike region would be performed. Generally, however, differential cross section data is not readily available.

The world data for the proton and the neutron magnetic form factors in the timelike region is shown on Figure 4.8. The steep threshold behaviour of the proton magnetic form factor has recently been studied. Several interpretations of this enhancement have been given in terms of $N\bar{N}$ bound states or unobserved meson resonances close to threshold. However, it has been shown that an explanation of the enhancement can be given in terms of final-state interactions in the proton-antiproton system [HHMS06]. The results of our analysis do not rule out the possibility of a near-threshold meson resonance, but show that neither is it required to explain the proton magnetic form factor at threshold, nor does the presence of a resonance pole at threshold necessarily provide this behaviour. The results are presented in Chapter 6.

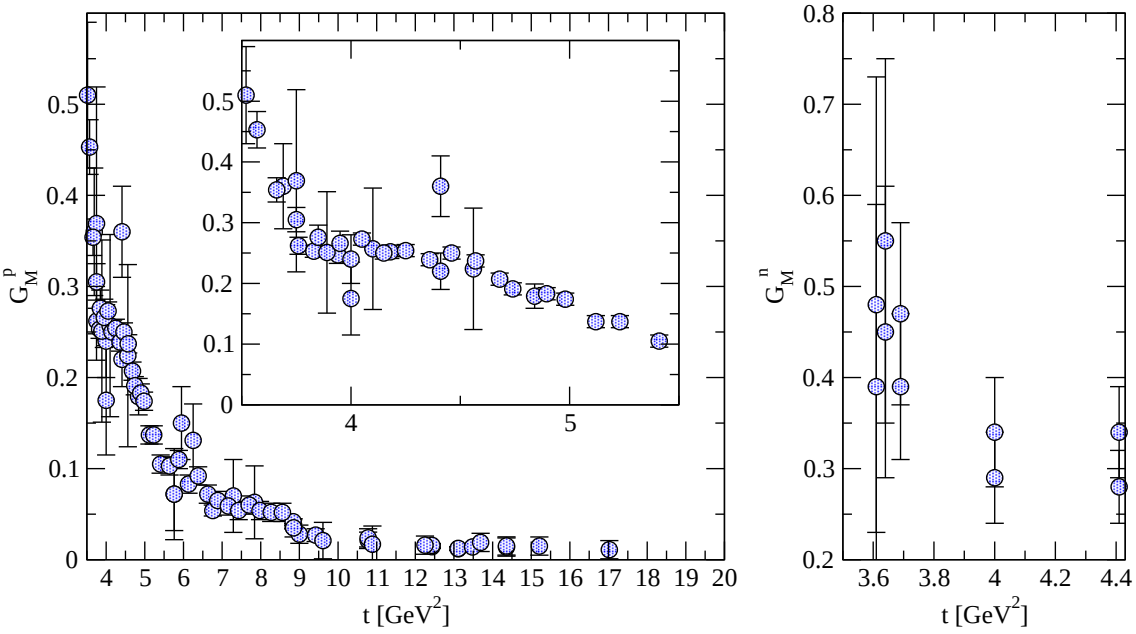

Figure 4.8: The world data for the magnetic form factors of the proton and the neutron in the timelike region. The inset for G_M^p shows the steep threshold behaviour of the proton magnetic form factor.

Chapter 5

Data Analysis

In this chapter, an overview of the mathematical formulation of the problem of the analysis of the experimental data is presented, and the use of Monte-Carlo techniques for generating error estimates on the results is discussed.

5.1 The Experimental Data Sets

The experimental data for the form factors used in the analysis is taken from Ref. [FW03] and in addition includes the new data that have appeared since 2003 and the timelike data. The timelike form factor data for the proton come from CERN [Bas77], Orsay [Del79], the DM2 experiment [Bis90], the FENICE experiment [Ant94], LEAR at CERN [Bar94], the E835 collaboration [Amb99], the CLEO collaboration [Ped05], the BES collaboration [Abl05] and the new high precision data from the BABAR collaboration [Aub05]. The pioneering FENICE experiment measured the neutron form factor in the timelike region [Ant93, Ant98]. The new data in the spacelike region come from the E93-038 collaboration at Jefferson Lab [Pla05], the A1 collaboration at Mainz [Ber03, Gla04], the E93-026 collaboration at Jefferson Lab [War03], the BLAST collaboration at MIT-BATES [Zis05] and the E95-001 collaboration at Jefferson Lab [And06]. The CLAS collaboration at Jefferson Lab has performed measurements of the neutron magnetic form factor for momentum transfers $0.6 \leq Q^2 \leq 5$ GeV^2 [Lac05]. These data are still preliminary, and are therefore generally not included in the fits. Nevertheless, we have performed a combined analysis of these data and the world data. The results of this analysis are discussed in Section 6.6. The data for the elastic electron-proton differential cross sections are a compilation of a wide range of publications. This compilation has been provided by Ingo Sick [Sic06]. In addition, numerical results for the Coulomb corrections for the differential cross section data have been provided to us [Sic06].

Interpolation is performed to obtain the Coulomb corrections for arbitrary values of the incoming electron energy and the electron scattering angle.

In total, there are 210 experimental form factor data points included in the spacelike region and 72 in the timelike region. There are 500 elastic electron-proton differential cross section data points. When Coulomb corrections are included, this number reduces to 374 due to the limited amount of data for the Coulomb corrections for forward and backward scattering. This leads to difficulties with interpolation, and differential cross section data at points where no reliable interpolation of the corrections can be performed are discarded in the analysis. This does not influence the analysis significantly. We have performed a test analysis of the full cross section data set without the inclusion of Coulomb corrections, and the results are in qualitative agreement with the results of the analyses of the smaller data set with the inclusion of Coulomb corrections. The application of the Coulomb corrections to the cross section values brings better agreement with polarisation transfer data compared to the analysis of uncorrected cross section data.

5.2 Formulation of the Mathematical Problem

Let $\vec{P}_{\text{full}}$ be the full space of the free adjustable parameters - the resonance masses, residua, the width parameters for the broad resonance terms in the SC approach, and the explicit pQCD term parameters in the pQCD approach. The dimension $\dim P_{\text{full}} \equiv f$ is the number of free parameters. Physical constraints restrict the possible values of the parameters - for example, the resonance masses must be positive and greater than 1 GeV. Let $\vec{P} \subset \vec{P}_{full}$ denote the physically acceptable parametric space. A vector $\vec{p} \in \vec{P}$ encodes all information necessary to calculate the form factors and cross sections. Therefore, the problem of the analysis of the experimental data is the problem of finding all possible vectors $\vec{p}_i$ for which the agreement between the phenomenological form factors and cross sections and the experimental data is best. In order to discuss the generation of errors, it is convenient to introduce a cuboid $\mathcal{P}$ in the parameter space centred around a point $\vec{p}_0$. Its volume is defined by all possible vectors $\vec{p}_{\text{ell}}$ the components of which satisfy $p^i_{ell} \in [p^i_0 - x^i; p^i_0 + x^i]$, where $\vec{x}$ is a constant vector.

The experimental data is sorted into datasets. There are 6 datasets: $G^n_E(Q^2)$, $G^n_M(Q^2)$, $G^p_E(Q^2)$, $G^p_M(Q^2)$ in the spacelike region, $G^p_M(q^2)$ in the timelike region, and the unpolarised elastic electron-proton scattering differential cross sections $d\sigma/d\Omega(E,\theta)$. It is important to note that the cross section data and the proton form factors in the spacelike region are not independent. In our form factor analyses, only the form factor data are included. In turn, the form factor data for the proton in the spacelike region are excluded from the cross section analyses. Each dataset contains the experimental data points: the measured values at given Q^2 and their errors for the form factors, and the measured values at given E and θ and their errors for the cross section data. A given set of parameters determined by a vector

$\vec{p} \in \vec{P}$ uniquely determines the phenomenological functions corresponding to each dataset.

In order to perform regression, a χ^2 function is constructed following the prescription of Höhler [HPSB76]:

$$\chi^2(\vec{P}) = \frac{N}{r(N-f)} \sum_{\rho=1\ldots r} \sum_{i=1\ldots n_\rho} \frac{1}{n_\rho} \left(\frac{F^\rho(\xi_i) - \Phi_i^\rho}{\epsilon_i^\rho} \right)^2 , \tag{5.1}$$

where r is the number of datasets corresponding to the different form factors and cross section data, N is the total number of experimental data points under consideration, n_ρ is the number of experimental points in a given dataset, f is the number of free parameters, F^ρ are the parameter-dependent phenomenological functions for a given dataset, Φ^ρ are the experimental data points, and ϵ^ρ are their corresponding experimental errors.

The chosen form of the χ^2 function (5.1) differs from the standard form,

$$\chi^2(\vec{P}) = \frac{1}{N-f} \sum_{i=1\ldots N} \left(\frac{F^\rho(\xi_i) - \Phi_i^\rho}{\epsilon_i^\rho} \right)^2 , \tag{5.2}$$

in its sensitivity to the number of experimental points in a given dataset. The sensitivity to data sets in which the number of experimental data points is much smaller than in other data sets is significantly enhanced when using Eq. (5.1). This leads to a better description of all experimental data, while maintaining the probabilistic likelyhood interpretation of the obtained results based on the χ^2 distribution [HPSB76], therefore allowing to introduce the theoretical 1σ uncertainty error bands as described in detail in Section 5.5.2.

The dimensions of the parameter space $\vec{P}$ - the number of free parameters in the problem - is restricted by stability criteria discussed in detail in Ref. [Sab80]. An increase in the number of free parameters eventually leads to large oscillations, which shows the mathematical instability of the problem. In short, we take the minimum number of poles necessary to fit the data. The number of free parameters is also strongly reduced by the normalisation and perturbative QCD constraints discussed in Section 3.3.

5.3 Function Minimisation Methods

In order to minimise the χ^2 function, two function minimisation routines implemented in the GNU Scientific Library (GSL) [GSL] have been used: the Fletcher-Reeves and the Polar-Ribière conjugate gradient algorithms. They feature much higher convergence stability than the traditional method of steepest descent.

In the steepest descent approach, during each iteration a step proportional to the gradient of the function with respect to all independent degrees of

freedom at the current point $\vec{P}_0$ is taken. The path along which the function is minimised is built as a discrete set of points $\vec{p}_i \in \vec{P}$:

$$\vec{p}_{i+1} = \vec{p}_i + \gamma_i \vec{\nabla}\chi^2(\vec{p}_i)\,, \tag{5.3}$$

where the step size, γ_i, is adjusted each iteration such that $\chi^2(\vec{p}_{i+1}) \leq \chi^2(\vec{p}_i)$ along the direction of the gradient. This simple method features poor convergence stability.

Conjugate gradient algorithms are an improvement of the steepest descent method. Whereas steepest descent approaches the minimum asymptotically, conjugate gradient methods find the solution in a finite number of iterations. The direction of minimisation is computed from, but not determined by, the gradient at the current point in parameter space. The path along which the function is minimised is built as a discrete set of points $\vec{p}_i \in \vec{P}$:

$$\begin{aligned} \vec{p}_{i+1} &= \vec{p}_i - \lambda_i \vec{h}_i\,, \\ \vec{h}_i &= \vec{\nabla}\chi^2(\vec{p}_i) + \gamma_{i-1}\vec{h}_{i-1} \\ \gamma_{i-1} &= \frac{\|\vec{\nabla}\chi^2(\vec{p}_i)\|^2}{\|\vec{\nabla}\chi^2(\vec{p}_{i-1})\|^2}\,, \end{aligned} \tag{5.4}$$

where λ_i minimises the χ^2 function in the search direction $\vec{h}_i$.

The Polak-Ribière conjugate gradient algorithm differs only in the selection of the weight parameter γ_i:

$$\gamma_{i-1} = \frac{(\vec{\nabla}\chi^2(\vec{p}_i) - \vec{\nabla}\chi^2(\vec{p}_{i-1}))\vec{\nabla}\chi^2(\vec{p}_i)}{\|\vec{\nabla}\chi^2(\vec{p}_{i-1})\|^2}\,. \tag{5.5}$$

The gradient $\vec{\nabla}\chi^2(\vec{p})$ is computed using an adaptive central difference algorithm for each degree of freedom as implemented in the GSL.

5.4 Implementation of Additional Soft Constraints

Two types of additional constraints can be enforced: error bar reduction constraints and composite soft constraints. Error bar reduction can be used to investigate certain features of the form factors within a narrow Q^2 region. In this approach, the error bars within a given dataset are artificially reduced by an adjustable factor. This simple technique has been used in order to investigate the spectral functions required to reproduce a bump-dip structure in the electric form factor of the neutron in the range $Q^2 \sim 0.25$ GeV^2.

Composite soft constraints allow to enforce a certain range of values for a composite variable x which, in general, may be a complicated function of the

parameters $\vec{p}$. This approach has been employed in order to constrain the radii or enforce resonance mass separation. Let $\langle x \rangle$ be the central value desired for x. A term of the following form is explicitly added to the χ^2 function:

$$\chi^2 \to \chi^2 + \kappa(x - \langle x \rangle)^2 \exp(\kappa(x - \langle x \rangle)^2)\,, \tag{5.6}$$

where x is the value computed for the current parameter set $\vec{p}$, and κ is a variable strength parameter which determines the extent of the acceptable deviation of the constrained variable from the desired central value. The chosen form of the additive term (5.6) has been shown to provide good convergence stability, and the adjustable parameter κ allows for necessary freedom in the selection of the acceptable deviations.

5.5 Monte Carlo Simulations

5.5.1 Sampling of Initial Guess Values

Conjugate gradient methods are sensitive to the initial guess value $\vec{p}_0$ from which the minimisation starts. In order to control the stability of convergence, it is necessary therefore to choose a point $\vec{p}_0$ which is close to a local minimum of $\chi^2(\vec{p})$. In order to find suitable starting points, Monte-Carlo sampling is performed in the parameter space $\vec{P}$: during each iteration, random values for the parameters are chosen within the physically acceptable volume $\vec{P}$, producing a vector $\vec{p}_{\rm MC}$. The value of $\chi^2(\vec{p}_{\rm MC})$ is computed, and, if the condition $\chi^2(\vec{p}_{\rm MC}) \leq \chi^2_{\rm max}$ is satisfied, the parameters are saved as a starting point for minimisation. The optimal value of $\chi^2_{\rm max}$ has been found to be $\chi^2_{\rm max} \sim 100$ based on an analysis of the convergence stability.

5.5.2 Generation of Error Bands

In order to provide a theoretical error estimate on our results, we use the prescription of Ref. [Yao06] to generate the 68% confidence intervals - the 1σ error bands. We start by computing the p-value for a given number of degrees of freedom [Yao06]. The problem is reduced to finding all solutions in the interval $\chi^2 \in [\chi^2_{min}; \chi^2_{min} + \delta]$, where δ is determined by the p-value equations, and χ^2_{min} is the final χ^2 of a fit. In our case, $\delta \approx 1.04$.

A two-step Monte-Carlo simulation process is employed to produce the error bands. Let $\vec{p}_{min}$ be a vector in parameter space $\vec{P}$ corresponding to the χ^2_{min} of a fit. We first start by defining a cuboid $\mathcal{P}$ by varying each component of $\vec{p}_{min}$ by a fixed percent level, $p^j_{min} \to p^j_{min} \pm x p^j_{min}$, where x is the variation parameter, typically $x \sim 0.05$. A sampling is then performed on the surface of $\mathcal{P}$ - random vectors lying on the surface are taken, and the corresponding χ^2 value is computed. If a solution $\chi^2 \in [\chi^2_{min}; \chi^2_{min} + \delta]$ is found, the value of the variational parameter

x is increased, and the simulation is repeated. The iterations continue until such a value of x is found that no solutions on the surface of $\mathcal{P}$ exist.

In the second stage, a simulation within the full volume of the cuboid defined by a given value of x is performed: random parametric vectors belonging within the volume of $\mathcal{P}$ are taken, and the corresponding values of χ^2 are calculated. If $\chi^2 \in [\chi^2_{min}; \chi^2_{min} + \delta]$, the values of the parameters and the form factor and cross section curves are saved. The number of iterations taken is much greater than the number of iterations that would be required to compute the geometrical volume of the region satisfying $\chi^2 \leq \chi^2_{min} + \delta$ lying within the given cuboid with high precision using Monte-Carlo techniques. This ensures a large enough sampling rate. The final result of the simulation gives the lower and upper estimates for the individual parameters and the form factor and cross section curves corresponding to the 1σ confidence interval.

This technique relies on the assumption that the experimental data follow the normal distribution. To test whether this assumption is fulfilled, good knowledge of the theoretical function expected to describe the data is required. Since the phenomenological form factors are our objects of investigation, such a test can not be performed. Generally, one expects experimental data to be normally distributed. If that is not the case, a probabilistic interpretation of the 1σ uncertainty bands is still valid by means of the Chebyshev inequality: at least 50% of the data are within the 1.4σ range. In our analysis, we assume that the experimental data follow the normal distribution.

Chapter 6

Results of the Form Factor Analysis

In this Chapter, our results for the two-pion contribution, the pion cloud of the nucleon, and the nucleon form factors analysed within both the SC and the explicit pQCD approaches are presented. An analysis of the preliminary neutron magnetic form factor data measured by the CLAS collaboration is included. The final fit parameters and the nucleon radii are discussed.

6.1 The Two-Pion Continuum

With the availability of new experimental data from three experimental groups [Akh99, Alo04, Ach05], we have re-analysed the pion form factor [BHM05] in a model-independent way using a Gounaris-Sakurai parameterisation [MMD95, GS68] including $\rho - \omega$ mixing:

$$\begin{aligned} F_\pi(t) = F_\pi^\rho(t)\frac{1+\alpha_\omega F_\pi^\omega(t)}{1+\alpha_\omega}\,,\; F_\pi^R(t) = \frac{m_R^2 + d m_R \Gamma_R}{D_R(t)},\; R = \rho,\omega\,, \\ D_R(t) = (m_R^2 - t) + \Gamma_R(m_R^2/k_R^2)[k^2(h(t) - h(m_R^2)) + \\ k_R^2 h'(m_R^2)(m_R^2 - t)] - i m_R \Gamma_R (k/k_R)^3 (m_R/\sqrt{t})\,, \end{aligned} \tag{6.1}$$

where

$$\begin{aligned} k &= \sqrt{t/4 - m_\pi^2}\,, \\ h(t) &= \frac{2}{\pi}\frac{k}{\sqrt{t}}\ln\frac{\sqrt{t}+2k}{2m_\pi}\,. \end{aligned} \tag{6.2}$$

The result of the analysis is shown in Fig. 6.1. Some discrepancy between the experimental results is evident in the region of the ρ peak. Due to the structure

of the dispersion relations (2.20), however, this only introduces an error at the 1% level in the final calculation, since higher-energy contributions are increasingly suppressed. The resulting sets of parameters used to reproduce the pion form factor results are given in Table 6.1.

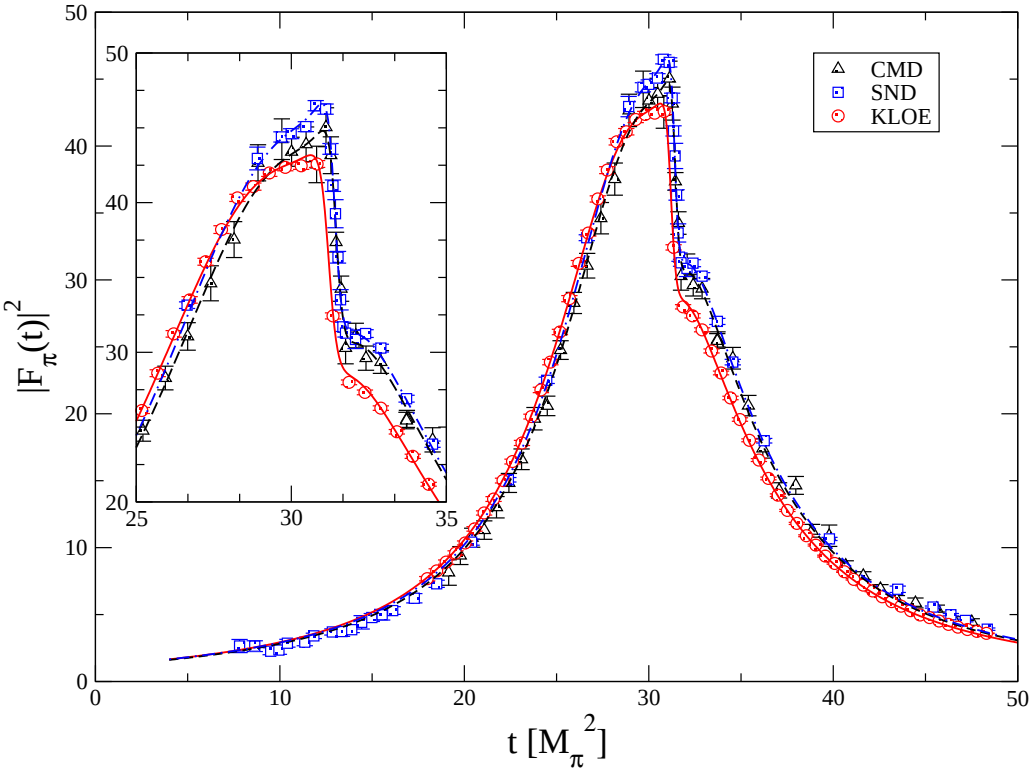

Figure 6.1: The pion electromagnetic form factor in the timelike region. The dashed, solid and dash-dotted lines are our model parameterisations. The inset shows the discrepancy in the $\rho - \omega$ resonance region.

	KLOE	SND	CMD-2
m_ρ [GeV]	0.77079	0.778473	0.778757
Γ_ρ [GeV]	0.14657	0.146781	0.150601
d_ρ	0.89313	1.00281	1.01525
m_ω [GeV]	0.780707	0.781797	0.782215
Γ_ω [GeV]	0.008	0.00822332	0.00906794
d_ω	0.7	1.00863	1.01001
α_ω	0.00190765	0.00151575	0.00171781

Table 6.1: List of parameters for the pion form factor in Eq. (6.1).

The second important ingredient of Eq. (3.1) are the P-wave pion-nucleon

scattering amplitudes. They are tabulated in [Hoh83] (as well as in an independent unpublished analysis [Pie]). We have performed an interpolation for the listed values in order to obtain the contribution to the spectral functions. The resulting two-pion contribution to the spectral functions is shown on Fig. 6.2. There are two important

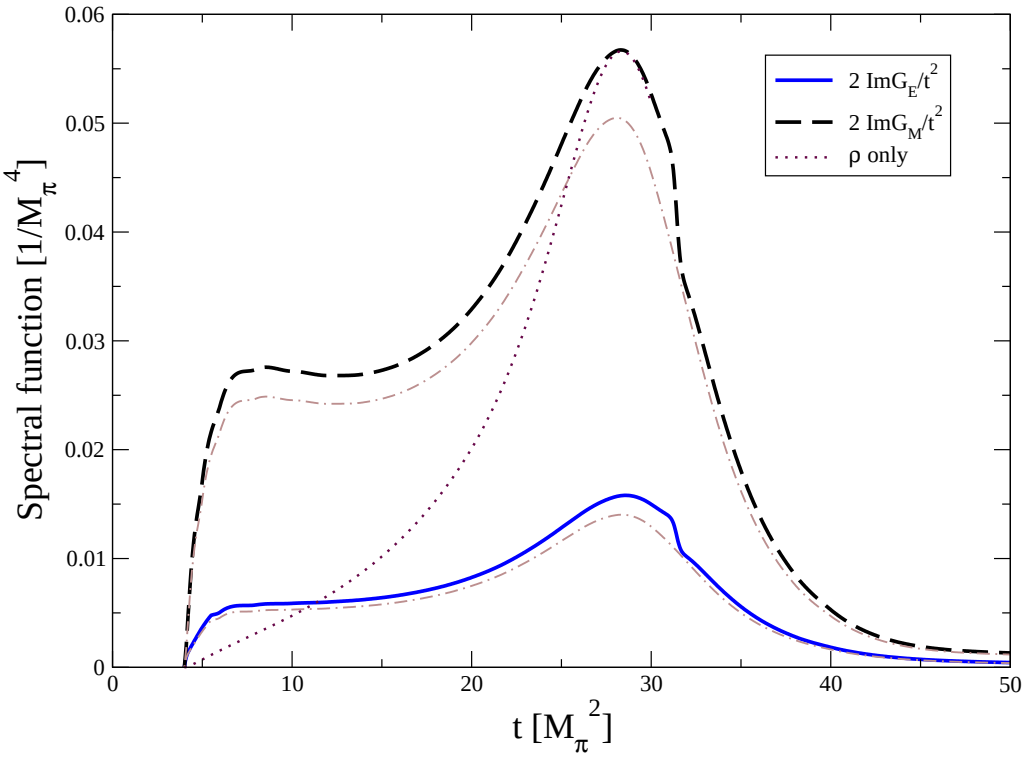

Figure 6.2: The two-pion spectral functions weighted by $1/t^2$ for G_E (solid line) and G_M (dashed line). The previous results by Höhler [Hoh83] without the inclusion of $\rho - \omega$ mixing (gray dash-dotted line), as well as the result for a ρ resonance only contribution (dotted line) are shown.

features of the two-pion contribution to the spectral functions. First, as already pointed out in Ref. [FF59], they contain the contribution of the ρ meson peak at $t \simeq 30 M_\pi^2$. Second, on the left shoulder of the ρ, there is a strong enhancement of the spectral functions. The threshold enhancement comes from the logarithmic singularity on the second Riemann sheet located at $t_c = 4M_\pi^2 - M_\pi^4/M_N^2 = 3.98 M_\pi^2$, very close to the two-pion threshold ($t = 4M_\pi^2$), due to the triangle diagram (Fig. 6.3). If one were to neglect this important unitarity correction, one would severely underestimate the nucleon isovector radii [HP75]. This singularity has also been analysed at leading one-loop order in relativistic chiral perturbation theory (ChPT) [GSS87, Mei91], as well as in heavy baryon chiral perturbation theory [BKM96, Kai03] and in a covariant calculation based on infrared regularisation [KM00, SGS05]. Thus, the most important 2π contribution can be calculated using unitarity or ChPT (in the latter case, the ρ contribution is included in a low-energy constant).

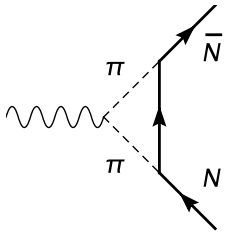

Figure 6.3: The pion-nucleon triangle diagram. The wavy line denotes the photon.

The contribution of the two-pion continuum to the nucleon form factors is obtained by inserting the spectral functions into the dispersion relations (Eq. 2.20) and performing the integration. It is convenient to use a simple parameterisation of the result to save computation time:

$$F_i^{(v),2\pi}(t) = \frac{a_i + b_i(1 - t/c_i)^{-2/i}}{2(1 - t/d_i)}, \quad i = 1, 2\,, \tag{6.3}$$

where $a_1 = 1.10788$, $b_1 = 0.109364$, $c_1 = 0.36963$ GeV^2, $d_1 = 0.553034$ GeV^2, $a_2 = 5.724253$, $b_2 = 1.111128$, $c_2 = 0.27175$ GeV^2, $d_2 = 0.611258$ GeV^2. In our analysis, we use this simple parameterisation for the two-pion contribution to the isovector form factors of the nucleons.

6.2 The Pion Cloud of the Nucleon

In order to obtain information about the spacial distribution of the pion cloud, Eq. (2.13) can be applied to the obtained two-pion spectral functions after the contribution of the ρ resonances has been subtracted. While this procedure introduces a model dependence in the calculation of the charge and magnetisation density distributions due to the pion cloud, it nontheless serves as a good quantitative estimate of these distributions, and allows to determine the ρNN vector and tensor coupling constants. Following Ref. [Kai03], the contribution of the ρ resonance can be parameterised as

$$\mathrm{Im}G_I^{V,\rho}(t) = b_I \frac{M_\rho^2 \sqrt{t}\Gamma_\rho(t)}{(M_\rho^2 - t)^2 + t\Gamma_\rho^2(t)}, \tag{6.4}$$

where $\Gamma_\rho(t) = g^2(t - 4M_\pi^2)^{3/2}/48\pi t$, $M_\rho = 769.3$ MeV, and the coupling $g = 6.03$ is determined from the empirical value $\Gamma_\rho(M_\rho^2) = 150.2$ MeV. The parameters b_I are adjusted to the height of the resonance peak. In order to evaluate the ρNN coupling constants, the same procedure is applied to the Dirac and Pauli form factors, $F_i^{v,2\pi}$, $i = 1, 2$.

The result of our analysis of the charge and magnetisation densities is shown on Figure 6.4. It is in good agreement with alternative determinations - a

recent review is given in Ref. [Mei07]. There is a peak at $r \sim 0.4$ fm, and the distributions fall off smoothly for larger values of r - the pion cloud contribution effectively extends to $r \sim 1.5$ fm. As a result of a similar analysis of the Dirac and Pauli form factors, the following ρNN couplings are obtained: $g^1_{\rho NN} \sim 3.0$, $\kappa_{\rho NN} = 5.9$.

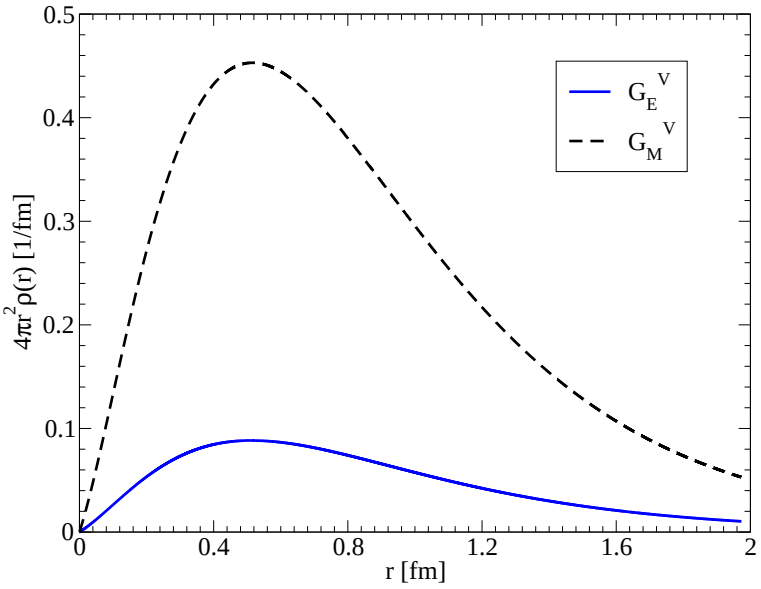

Figure 6.4: The densities of charge and magnetisation due to the pion cloud: $4\pi r^2 \rho(r)$ for the isovector magnetic (dashed line) and electric (solid line) Sachs form factors.

Friedrich and Walcher performed an analysis of the electric form factor of the neutron [FW03] using a modified Galster parameterisation,

$$G_E^n(Q^2) = \frac{aQ^2}{(1 + bQ^2 + cQ^4)^5} + \frac{dQ^2}{(1 + eQ^2)(1 + fQ^2)^2} \,. \tag{6.5}$$

The second term in Eq. (6.5) corresponds to the Galster parameterisation. The first term was added in order to reproduce additional structure in G_E^n around $Q^2 \sim 0.25$ GeV^2. This is the so-called "bump-dip" structure. By applying a Fourier transform to G_E^n, they obtain a prediction for the charge distribution in the neutron attributed to the pion cloud. This leads to a much larger pion cloud range prediction, $r > 2$ fm, which is at odds with the results we have obtained through the analysis of the two-pion contribution to the spectral functions. A detailed analysis of the possibility of additional structure in the neutron electric form factor, and the implications for the pion cloud of the nucleon, is presented in Section 6.5.

6.3 Results for the Superconvergence Approach

The results of the data analysis using superconvergence relations with the inclusion of a broad resonance (3.21) in both the isoscalar and the isovector channels are shown on Figure 6.6 for the form factors in the spacelike region, and on Figure 6.7 for the form factors in the timelike region. The resulting spectral functions corresponding to this analysis are shown on Figure 6.5. This fit has 17 free parameters and a total χ^2/dof of 1.8. The χ^2/dof for the spacelike data alone is $\chi^2_S = 0.99$. The parameters corresponding to this analysis are listed in Table 6.2.

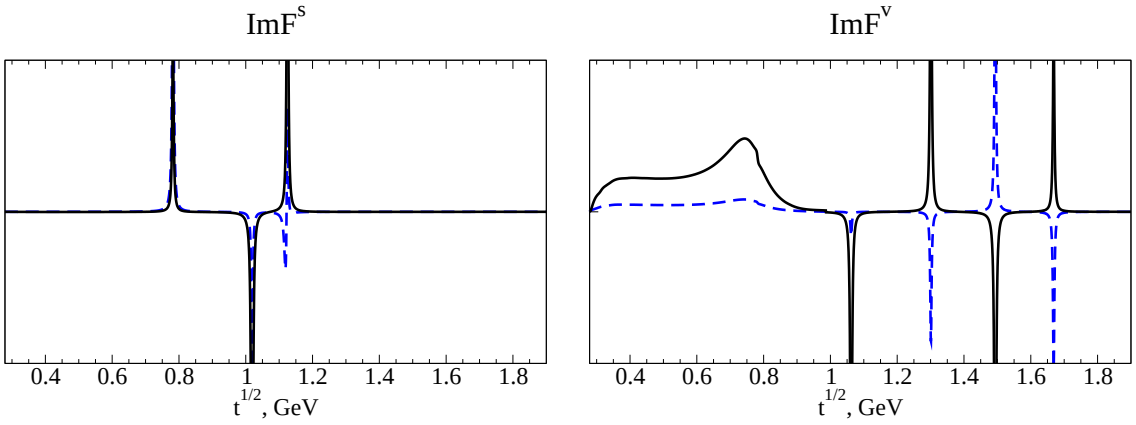

Figure 6.5: The spectral functions corresponding to the form factor analysis using the superconvergence relations approach with the inclusion of a broad resonance. The dashed lines correspond to F_1^I, the solid lines to F_2^I, $I = s, v$.

In addition to the ω and the ϕ meson poles, one additional effective pole term and one broad resonance term are included in the isoscalar channel, and four effective pole terms and one broad resonance term are included in the isovector channel. The spectral functions show a strong interference of the effective isoscalar pole at $M_{s_1} = 1.125$ GeV with the $\rho\pi$ contribution parameterised by a fictious pole at $M_{\omega'} = 1.12$ GeV. In the isovector channel, the mass splitting between the effective resonance poles is larger. The residua are comparable in magnitude and differ in sign between the higher-mass resonances. This leads to a dipole behaviour of the form factors - resonances with close masses and opposite-sign residua produce dipole-like structures. This behaviour is consistent with the previous analyses [HPSB76, MMD95, HMD96, HM03].

The contribution of the broad resonance terms to the spectral functions is very small - it is not visible on the plot - in comparison to the other contributions due to the large value of the width-like parameters Γ_I. This is consistent with the notion of parameterising weak continuum contributions beyond the dominant contributions which we include explicitly.

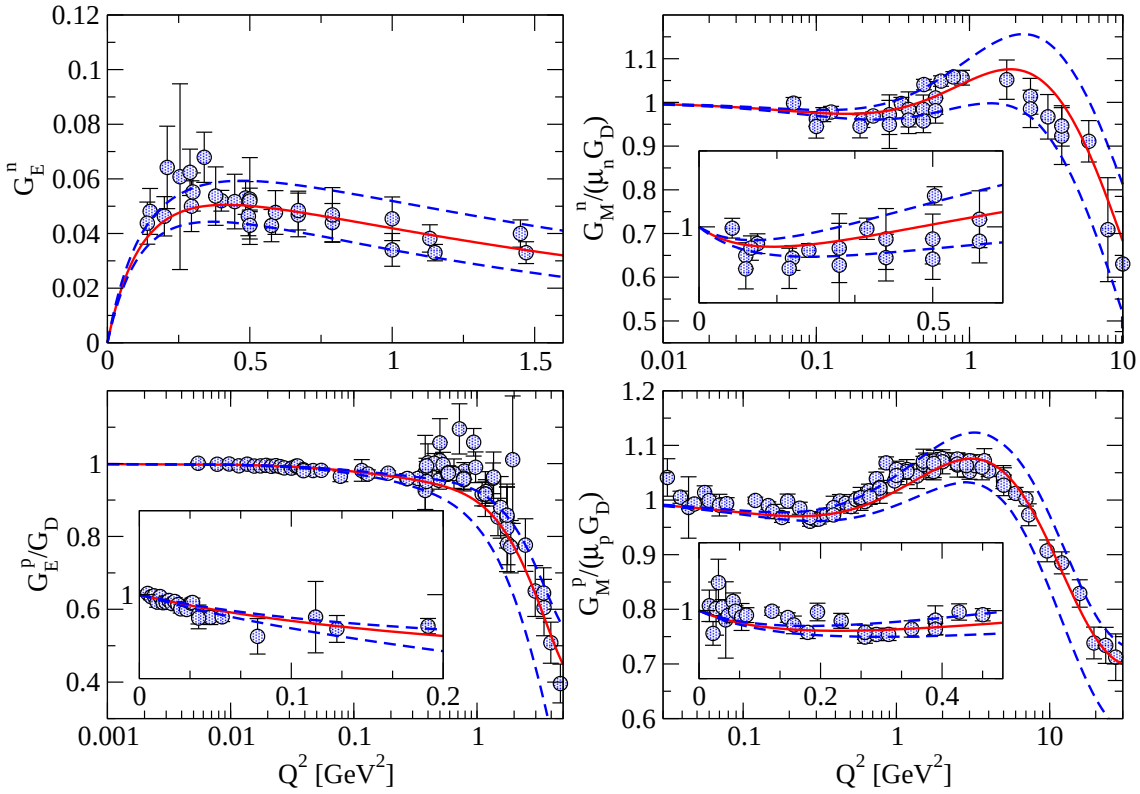

Figure 6.6: Description of the form factors in the spacelike region using the superconvergence relations approach with the inclusion of a broad resonance. The solid lines indicate the best fit result, the dashed lines show the theoretical 1σ uncertainty bands.

A good description of both the space- and the timelike data is obtained. In the spacelike region, the electric form factor of the proton is well described in the low Q^2 range, an important result for the discussion of the proton charge radius, which is directly proportional to the derivative of the electric form factor at the origin (3.10). Some of the experimental data for the proton electric form factor at $Q^2 \sim 1$ GeV^2 do not fall within the 1σ uncertainty bands. Those data are the highest Q^2 data extracted using the Rosenbluth separation technique which are included in the analysis. They are not entirely consistent with the polarisation transfer data in that region, and our analysis favours the polarisation transfer results. The neutron electric form factor is smooth, without any hint of additional structure at low Q^2.

In the timelike region, the proton magnetic form factor is well described, except for the two experimental data points which suggest more enhancement of the form factor at threshold. Both of these points, however, are within our 1σ uncertainty bands. Some additional structure seen at $q^2 \approx 4.5$ GeV^2 by the BABAR collaboration is not reproduced. This behaviour is not suggested by the data obtained by the LEAR collaboration. More experimental data at the threshold region are required in order to resolve this discrepancy, and several promising experiments

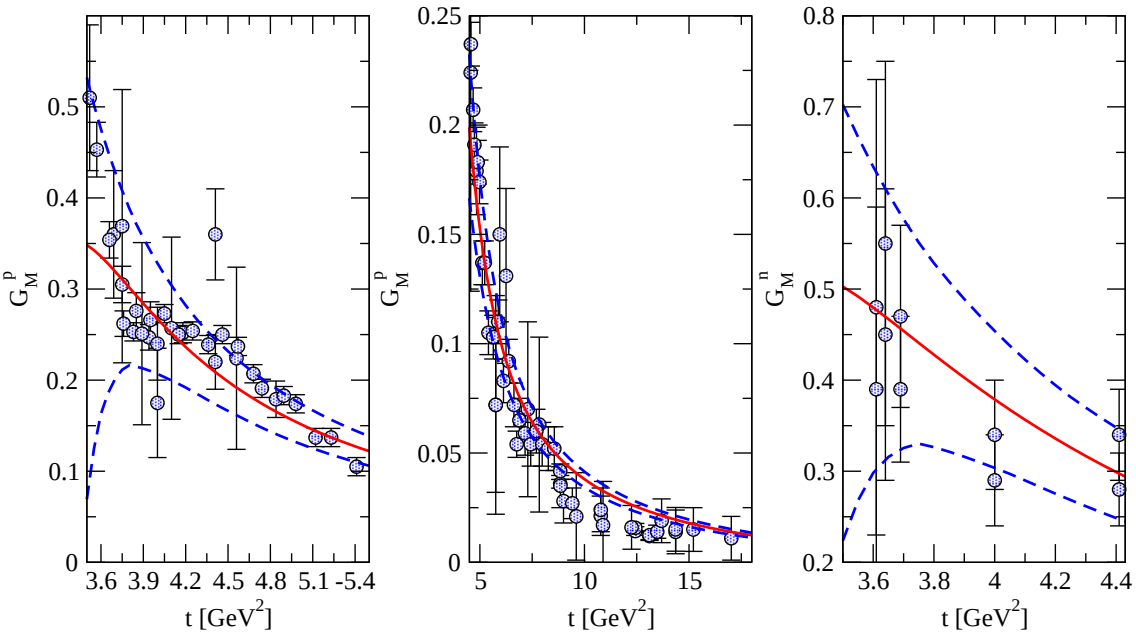

Figure 6.7: Description of the form factors in the timelike region using the superconvergence relations approach with the inclusion of a broad resonance. The solid lines indicate the best fit result, the dashed lines show the theoretical 1σ uncertainty bands.

- PANDA and PAX at GSI - are under preparation. A small discrepancy also exists at $q^2 \approx 10$ GeV^2. The experimental data suggest a faster form factor decrease in that region, but the data points are still largely within the 1σ uncertainty band.

The neutron magnetic form factor in the timelike region does not participate in the analysis since the only available data are the result of one experiment. It is therefore a genuine prediction - the few available experimental data points lie well within our theoretical uncertainty error bands.

The values and error estimates extracted for the nucleon radii are given in Table 6.3. Despite the fact that the proton electric form factor is well described at low Q^2 values, the proton charge radius is significantly smaller than suggested by Lamb shift measurements [Mel99], $r_E^p = 0.883(14)$. The reason for this discrepancy is not fully understood at this time.

The ϕNN residua obtained can not be assigned direct physical significance in this analysis due to the close-lying pole at $M_{s_1} \approx 1.125$ GeV, which strongly influences the residua of the ϕ. The ω residua are comparable to those reported in a previous analysis [HM03], but the tensor coupling differs in size and magnitude from older determinations [MMD95, HMD96].

The analysis of the ratio $Q^2 F_2^p / F_1^p$ corresponding to this fit shows that the onset of pQCD behaviour occurs around $Q^2 \approx 100$ GeV^2. The currently available

Resonance	Mass [GeV]	a_1 [GeV^2]	a_2 [GeV^2]	Γ [GeV^2]
ω	0.782	0.755960	0.370592	–
ϕ	1.019	−0.776537	−2.913229	–
s_1	1.124860	0.902379	2.484859	–
s_2	2.019536	0.022798	−0.130622	5.158635
v_1	1.062128	−0.127290	−2.162533	–
v_2	1.300946	−1.243412	3.704233	–
v_3	1.493630	4.191380	−7.091021	–
v_4	1.668522	−3.176013	3.723858	–
v_5	2.915451	0.048987	0.075965	19.088297

Table 6.2: Fit parameters in the superconvergence relations approach. This fit has 17 free parameters and a total χ^2/dof of 1.8.

Radius	Best value	Error estimate
$(r_E^n)^2$ [fm^2]	−0.117	−0.128 - −0.110
r_E^p [fm]	0.844	0.840 - 0.852
r_M^n [fm]	0.862	0.854 - 0.871
r_M^p [fm]	0.854	0.849 - 0.859

Table 6.3: Radii values and error estimates extracted using the analysis within the SC approach.

experimental data lie very far from this prediction.

6.4 Results for the Explicit pQCD Approach

The results of the analysis with the inclusion of an explicit pQCD term (3.25) in both the isoscalar and the isovector channels are shown on Figure 6.8 for the form factors in the spacelike region, and Figure 6.9 for the form factors in the timelike region. This fit has 14 free parameters and a total χ^2/dof of 2.0. The χ^2 for the spacelike data alone is $\chi^2_{\rm S} = 1.23$. The resonance parameters corresponding to this fit are listed in Table 6.4, and the pQCD term parameters in Table 6.5. In addition to the ω, $\pi\pi$, $K\bar{K}$, the $\rho\pi$ contributions and an explicit ϕ pole, there is one additional resonance pole included in the isoscalar channel, and three resonance poles in the isovector channel. The spectral functions corresponding to this fit are similar in their essential features to the spectral functions obtained in the SC approach. Close-lying effective resonance poles have residua of comparable size and opposite in sign. The effect of the pQCD term on the spectral function is more difficult to calculate rigorously, as the integration cut in the dispersion integral is undefined in this case.

The values of a_i^I, $i = 1, 2$, $I = s, v$ are very small in magnitude, however, and one therefore expects a very weak contribution to the spectral functions in comparison to the continuum contributions we include explicitly.

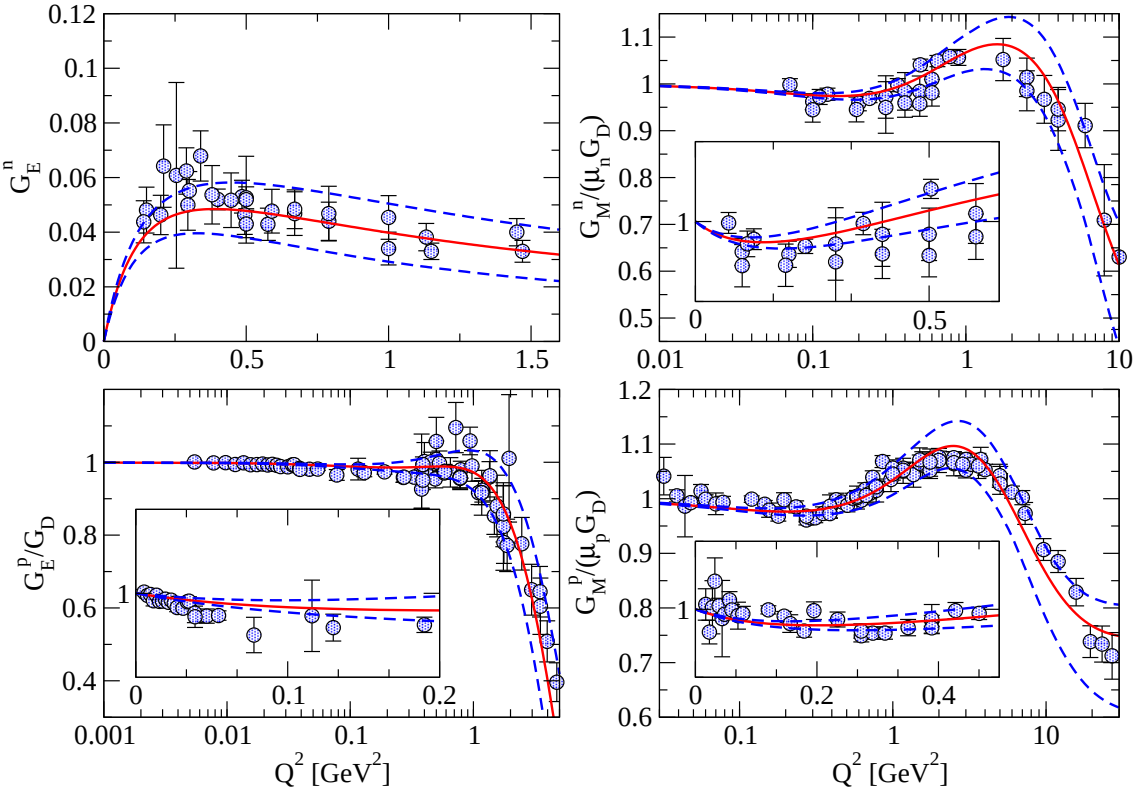

Figure 6.8: Description of the form factors in the spacelike region using the explicit pQCD term approach. The solid lines indicate the best fit result, the dashed lines show the theoretical 1σ uncertainty bands.

Similar to the broad resonance approach, a good description of the data is obtained in both the space- and the timelike regions. More generally, the approaches have been shown to yield similar results under similar constraints. This leads to a very important conclusion: given pQCD constraints are satisfied, the inclusion of a weak parameterisation of continua to provide an imaginary part of the form factors in the timelike region beyond the $N\bar{N}$ threshold is an important ingredient of the form factor analysis, while the actual functional form of the continua does not play a major role.

The ϕ pole in this analysis is free from other close-lying poles, except the explicitly included $K\bar{K}$ and $\rho\pi$ continuum contributions. Therefore, a rough estimate of the ϕNN coupling constants can be made: $g^1_{\phi NN} \approx 2.0$, $\kappa_{\phi NN} \approx -2$. The interpretation of these couplings as the pure ϕ meson couplings, however, is difficult without considering other exchange mechanisms in addition to the $K\bar{K}$ exchange [MMSO97]. Nevertheless, it is useful to compare the explicit ϕ pole strength to

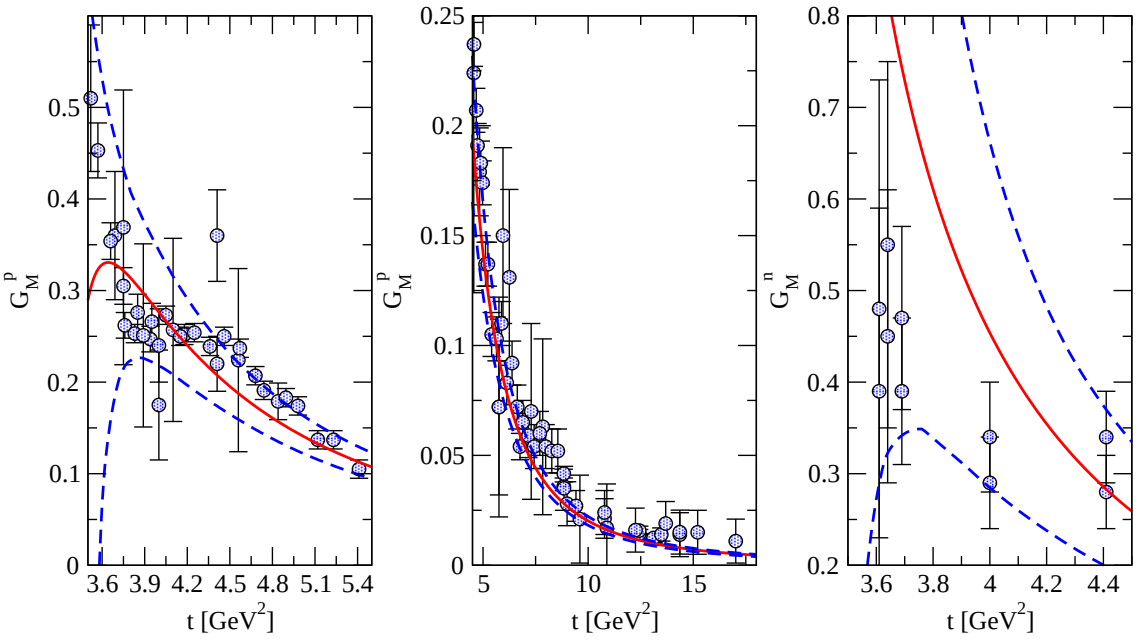

Figure 6.9: Description of the form factors in the timelike region using the explicit pQCD term approach. The solid lines indicate the best fit result, the dashed lines show the theoretical 1σ uncertainty bands.

the contributions included with the $K\bar{K}$ and $\rho\pi$ exchange terms. The strength of each contribution is presented on Figure 6.10. This result can be compared to the result of Ref. [MMSO97]: the contribution to the vector coupling is largely determined by the $K\bar{K}$ contribution; the contribution to the tensor coupling, on the other hand, largely cancels with the contribution from the $K\bar{K}$ continuum due to other processes. In our present analysis, the ϕ contribution indeed largely cancels the $K\bar{K}$ contribution in the case of the Pauli form factor. One therefore expects the vector coupling of the pure ϕ to be somewhat larger than the value obtained in our analysis, and the ratio of the tensor to vector couplings to be significantly smaller.

The radii values corresponding to this analysis are given in Table 6.6. The proton charge radius comes out lower than in the SC approach - this can also be seen from the somewhat poorer description of the low-Q^2 proton electric form factor data. In the timelike region, the threshold behaviour of the proton magnetic form factor remains largely unreproduced, even though there are effective resonance pole contributions close to the $N\bar{N}$ threshold in both the isoscalar and the isovector form factors at $M_V \sim 1.8$ GeV. The neutron magnetic form factor in the timelike region does not participate in the fit, but the available experimental data are still within the theoretical uncertainty bands.

Our results for the ratios $QF_2^p(Q^2)/F_1^p(Q^2)$ and $Q^2F_2^p(Q^2)/F_1^p(Q^2)$ within the pQCD approach are shown on Figure 6.11 in comparison to the JLab data [JLAB00, JLAB01]. The analysis of the ratio $Q^2F_2^p/F_1^p$ corresponding to this fit

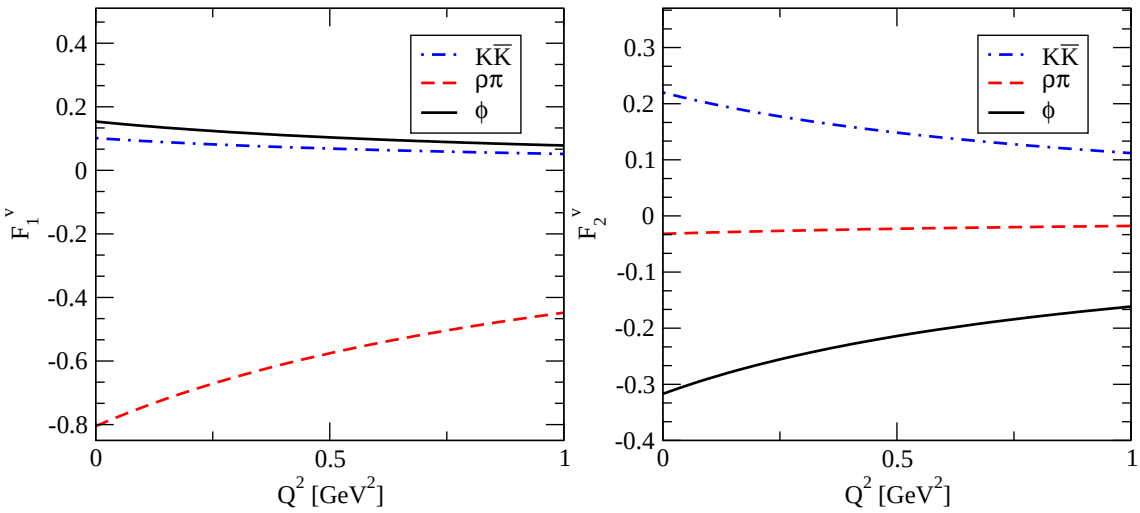

Figure 6.10: Contribution of the $K\bar{K}$, $\rho\pi$ and the explicit ϕ terms to the isovector spectral functions as obtained in the explicit pQCD approach analysis.

Resonance	Mass [GeV]	a_1 [GeV^2]	a_2 [GeV^2]
ω	0.782	0.616384	0.114681
ϕ	1.019	0.159562	−0.329255
s_1	1.799639	0.128654	0.026174
v_1	1.000000	−0.309199	−1.078695
v_2	1.627379	3.695960	−4.301057
v_3	1.779245	−3.693109	3.630255

Table 6.4: Resonance parameters for the fit with explicit pQCD continuum. This fit has 14 free parameters and a total χ^2/dof of 2.0.

a_1^s	a_1^v	b_1 [GeV^{-2}]	c_1 [GeV^{-1}]
0.002321	−0.028391	0.152903	0.161871
a_2^s	a_2^v	b_2 [GeV^{-3}]	c_2 [GeV^{-1}]
−0.126598	−0.011693	1.159998	1.150000

Table 6.5: Parameters of the explicit pQCD term for the fit with explicit pQCD continuum. This fit has 14 free parameters and a total χ^2/dof of 2.0.

predicts the onset of pQCD behaviour at $Q^2_{\mathrm{pQCD}} \approx 40$ GeV^2. As expected, this prediction is smaller than the prediction obtained within the SC approach. This prediction also agrees with the findings of Ref. [MMD95], where an estimate of $Q^2_{\mathrm{pQCD}} \geq 30$ GeV^2 is given. The ratio $QF_2^p(Q^2)/F_1^p(Q^2)$ is consistent with the

Radius	Best value	Error estimate
$(r_E^n)^2$ [fm^2]	-0.118	-0.13 - -0.11
r_E^p [fm]	0.829	0.822 - 0.835
r_M^n [fm]	0.863	0.859 - 0.871
r_M^p [fm]	0.849	0.843 - 0.852

Table 6.6: Radii values and error estimates extracted using the pQCD continuum approach.

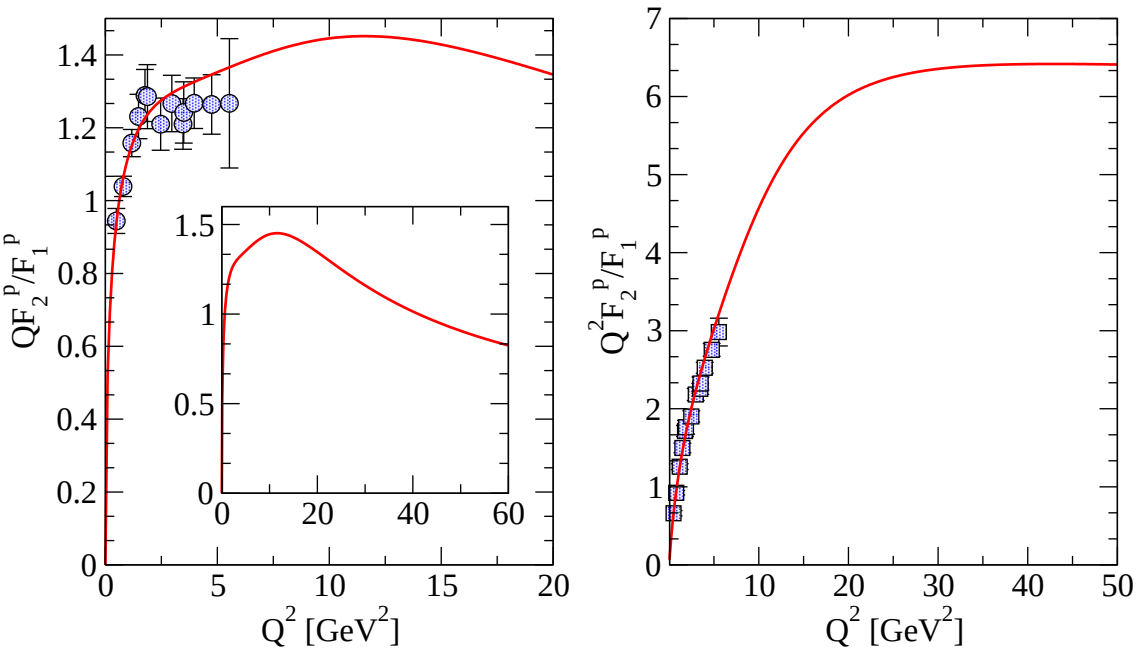

Figure 6.11: The ratios $QF_2^p(Q^2)/F_1^p(Q^2)$ and $Q^2F_2^p(Q^2)/F_1^p(Q^2)$ obtained within the pQCD approach compared to experimental data from JLab [JLAB00, JLAB01]. The inset shows the high-Q^2 behaviour of $QF_2^p(Q^2)/F_1^p(Q^2)$.

available experimental data. It starts to decrease at $Q^2 \approx 15$ GeV^2. The slope changes, and eventually the ratio behaves like $1/Q$, as shown in the inset. The currently available experimental data for the form factors are still far from the asymptotic pQCD regime.

6.5 The G_E^n Bump-Dip Structure

In Ref. [FW03], a very long-range contribution to the nucleon charge distribution in the Breit frame extending to ~ 2 fm was found based on a phenomenological fit to the nucleon form factors using an ansatz for the pion cloud based on the idea

that the proton can be thought of as a virtual neutron - positively charged pion pair. The results produced an extra structure in the electric form factor of the neutron around $Q^2 \sim 0.25$ GeV^2, the so-called bump-dip structure. A first investigation of the pion cloud of the nucleon based on the dispersion-relation analysis of the two-pion contribution to the electromagnetic form factors was undertaken in Ref. [HDM03]. The findings were in disagreement with the results of Friedrich and Walcher [FW03]. The effective extent of the pion cloud was found to be less than 1.5 fm. We have performed an analysis of this problem using the updated two-pion continuum analysis described in Section 6.1.

In order to reproduce the pronounced bump-dip structure suggested by Friedrich and Walcher [FW03] in the neutron electric form factor, constraints of the masses of the effective resonance poles had to be removed. In addition, both the SC and the pQCD continuum approaches were combined. There is no physical motivation for combining the two continuum approaches, but we have found that this allows to increase the number of free parameters in the problem slightly without affecting the convergence stability significantly. Data in the timelike region were excluded from the fit. Experimental error bars for G_E^n in the region $Q^2 \sim 0.25$ GeV^2 as seen by the minimisation routines had to be significantly artificially reduced. The error bar reduction factor was of the order 10. This fit has 22 free parameters and a total χ^2/dof of 0.9 (spacelike data only). The spectral functions resulting from this analysis are shown on Figure 6.12. A strong modification of the two-pion

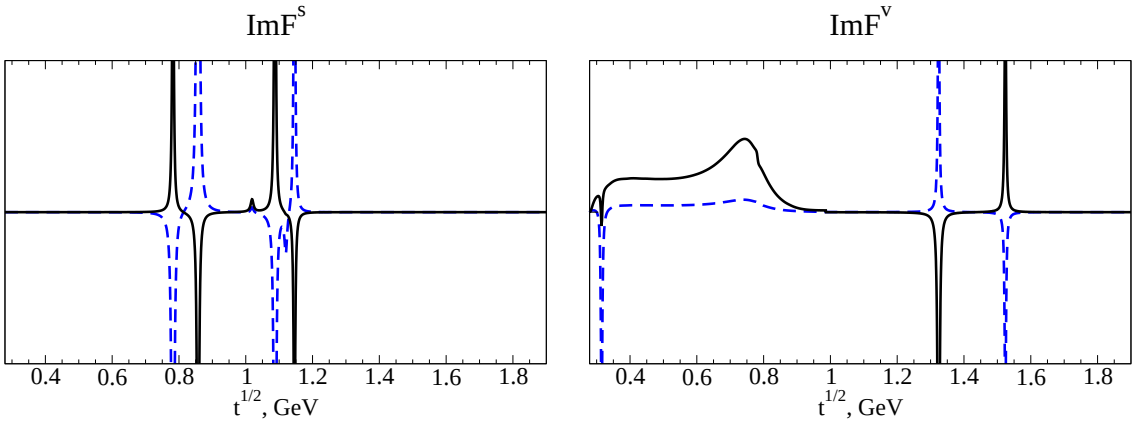

Figure 6.12: The spectral functions corresponding to the form factor analysis reproducing the bump-dip structure in G_E^n. The dashed lines correspond to F_1^I, the solid lines to F_2^I, $I = s, v$.

contribution close to threshold emerges. Another low-lying effective pole appears close to the ω, producing a strong interference in the isoscalar channel. It is not possible to reproduce the bump-dip structure without allowing for these low-mass modifications to the spectral function, which are at odds with what is known about the two-pion continuum from unitarity.

The results for the form factors in the spacelike region are shown on Figure 6.13. The dash-dotted line for G_E^n shows the bump-dip structure proposed by Friedrich and Walcher. It corresponds to the parameterisation:

$$G_E^n(Q^2) = \frac{aQ^2}{(1+bQ^2+cQ^4)^5} + \frac{dQ^2}{(1+eQ^2)(1+fQ^4)^2}\,, \tag{6.6}$$

with $a = 0.37$ GeV^{-2}, $b = 0.39$ GeV^{-2}, $c = 1.68$ GeV^{-4}, $d = 0.12$ GeV^{-2}, $e = f = 0.5$ GeV^{-2} given in [FW03]. A good overall description of the form factors in the

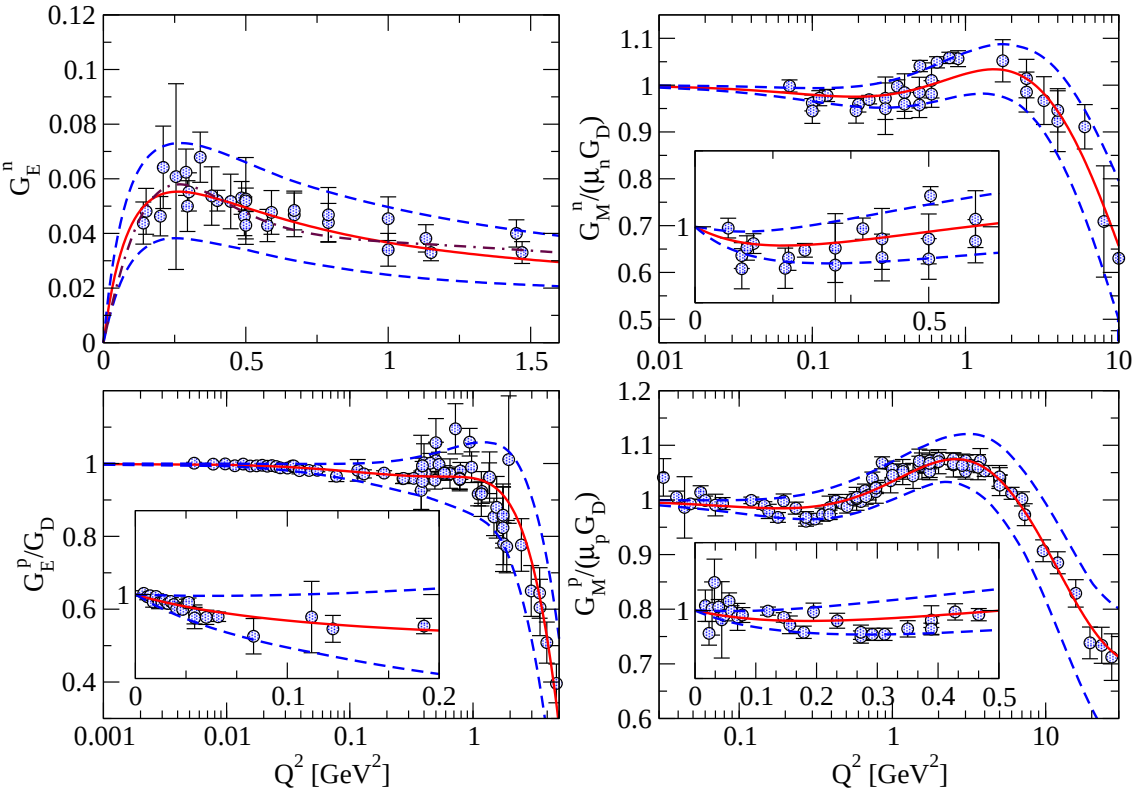

Figure 6.13: Description of the form factors in the spacelike region reproducing the bump-dip structure in G_E^n. The solid lines indicate the best fit result, the dashed lines show the theoretical 1σ uncertainty bands.

spacelike is obtained. Within the 1σ uncertainty bands, some additional structure in G_E^p emerges in the region $Q^2 \approx 2$ GeV^2. This influences the low-Q^2 error bands for the electric form factor of the proton, resulting in a large range of values for the proton charge radius, with the highest value $r_E^p = 0.90$ fm. The central value is comparable to our other fits. The result for the neutron charge radius, however, is lower than in our other analyses, and is not in good agreement with the value $(r_E^n)^2 = -0.115(4)$ fm^2 from an alternative determination [KKRS97]. The radii values and error error estimates are given in Table 6.9.

The results for the form factors in the timelike region are shown on Figure 6.14. Although the timelike data was not included in this analysis, it is non-

theless reasonably well described within the theoretical uncertainty bands. This fit has 22 free parameters and a total χ^2/dof of 0.9 (spacelike data only). The resulting resonance parameters are listed in Table 6.7, and the pQCD term parameters in Table 6.8.

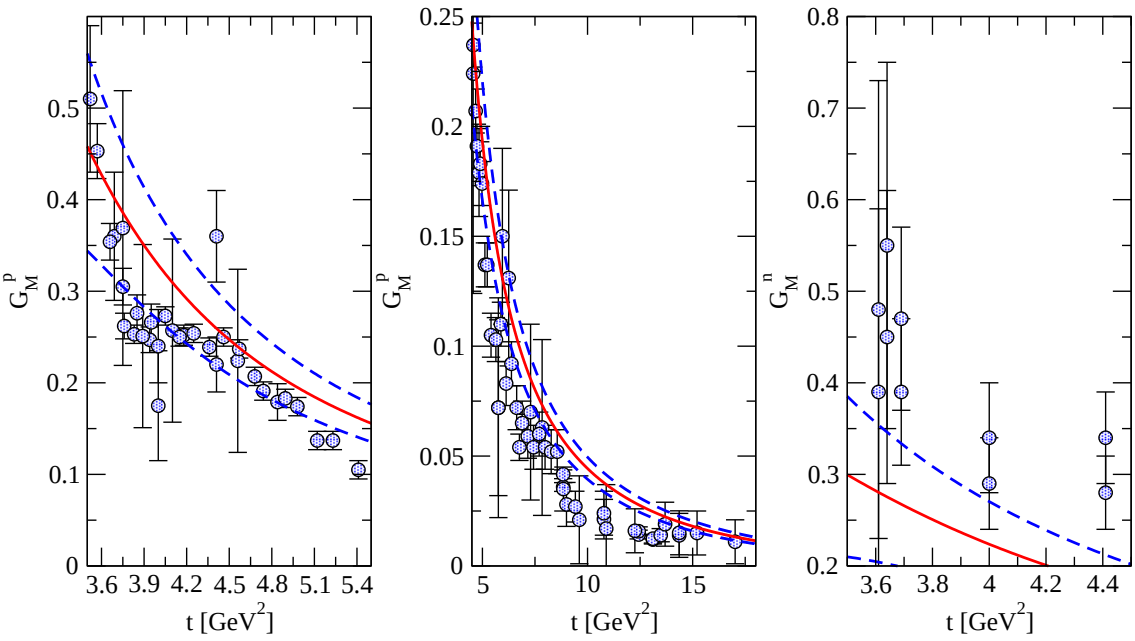

Figure 6.14: Description of the form factors in the timelike region reproducing the bump-dip structure in G_E^n. The experimental data in the timelike region did not participate in the fit. The results obtained in the timelike region are a genuine prediction. The solid lines indicate the best fit result, the dashed lines show the theoretical 1σ uncertainty bands.

To summarise, neither the current experimental data, nor the preliminary results of the measurements of G_E^n at MAMI support any additional structure in the neutron electric form factor in the region $Q^2 \sim 0.25$ GeV^2. The additional strength in the spectral functions required to produce the bump-dip structure suggested by Friedrich and Walcher must indeed originate in the $\pi\pi$ contribution, close to the two-pion threshold. Such a contribution is at odds with what is known about the $\pi\pi$ continuum from unitarity as detailed in Section 6.1.

Resonance	Mass [GeV]	a_1 [GeV^2]	a_2 [GeV^2]	Γ [GeV^2]
ω	0.782	-3.088199	1.516336	–
s_1	1.087524	-9.309347	5.152311	–
s_2	0.857075	7.969599	-3.102716	–
s_3	1.145783	5.332548	-3.754331	–
v_1	0.315028	0.002785	-0.008642	–
v_2	1.523890	-3.257202	3.767630	–
v_3	1.323997	2.770486	-5.497436	–
v_4	2.834388	0.177584	-0.011050	13.477161

Table 6.7: Resonance parameters for the fit with the bump-dip structure in G_E^n. This fit has 22 free parameters and a total χ^2/dof of 0.9 (spacelike data only). Note that s_2 and v_1 are the additional low-mass poles necessary to generate the bump-dip structure.

a_1^s	a_1^v	b_1 [GeV^{-2}]	c_1 [GeV^{-1}]
-0.786259	-0.320320	0.971368	1.235451
a_2^s	a_2^v	b_2 [GeV^{-3}]	c_2 [GeV^{-1}]
-0.000484	0.033410	0.091209	0.994702

Table 6.8: Parameters of the explicit pQCD term for the fit with the bump-dip structure in G_E^n. This fit has 22 free parameters and a total χ^2/dof of 0.9 (spacelike data only).

Radius	Best value	Error estimate
$(r_E^n)^2$ [fm^2]	-0.187	-0.263 - 0.113
r_E^p [fm]	0.854	0.807 - 0.904
r_M^n [fm]	0.845	0.810 - 0.875
r_M^p [fm]	0.828	0.799 - 0.854

Table 6.9: Radii values and error estimates extracted from the G_E^n bump-dip structure fit.

6.6 Analysis of Preliminary CLAS Data for G_M^n

The CLAS collaboration has recently measured the magnetic form factor of the neutron in the spacelike region for momentum transfers $Q^2 = 0.5 \ldots 4.5$ GeV^2. These preliminary results disagree with the world data on G_M^n in the region $Q^2 \sim 1$ GeV^2. In order to analyse the effect of this discrepancy, we have performed a simultaneous analysis of both the world data and the preliminary CLAS data. The result of the analysis for the form factors in the spacelike region is shown on Figure 6.15, and for the form factors in the timelike region on Figure 6.16. This fit has 15 free parameters and a total χ^2/dof of 2.2. The larger χ^2 compared to other fits is explained by the discrepancy between the world data and the preliminary CLAS data. The resulting resonance parameters are listed in Table 6.10, and the pQCD term parameters in Table 6.11. An analysis of both data sets using the SC approach has also been performed. It yields similar results, and is therefore not further discussed here.

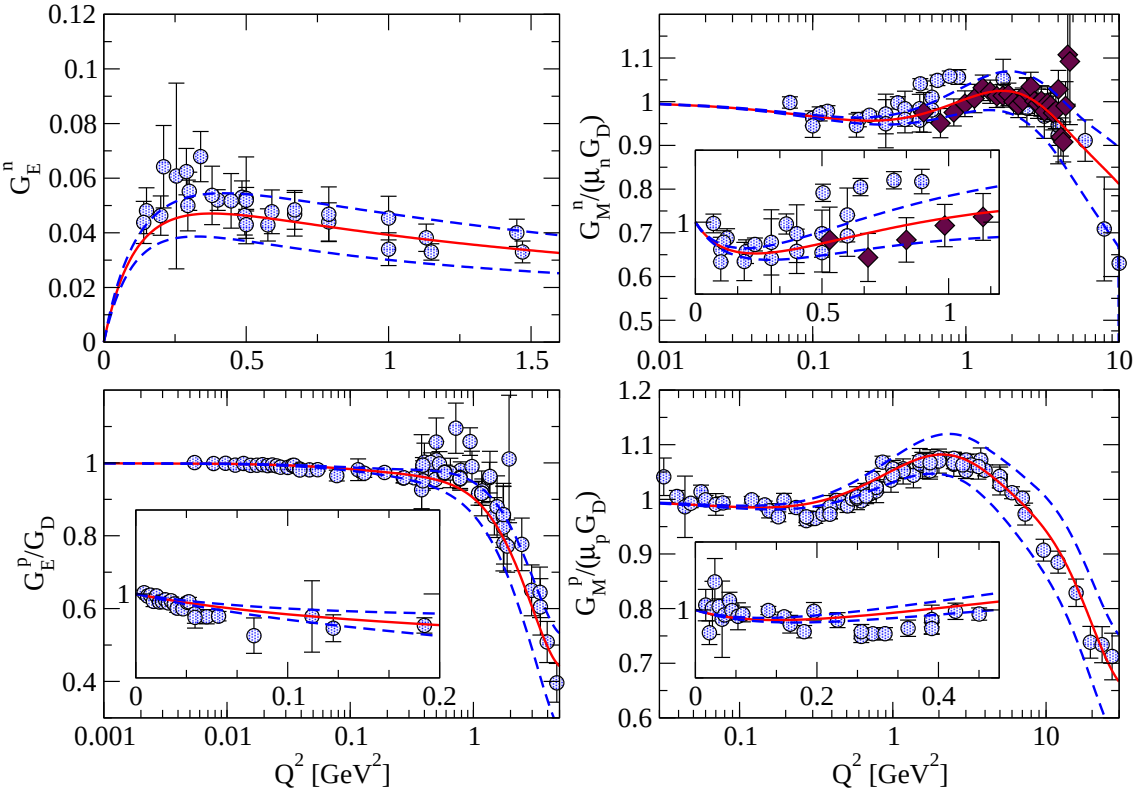

Figure 6.15: Description of the form factors in the spacelike region with the inclusion of preliminary CLAS data for G_M^n. The solid diamonds denote the new CLAS data, the circles show the world data. The solid lines indicate the best fit result, the dashed lines show the theoretical 1σ uncertainty bands.

The initial expectation for the outcome of this analysis was that in the region of the discrepancy between the world data and the preliminary CLAS data the

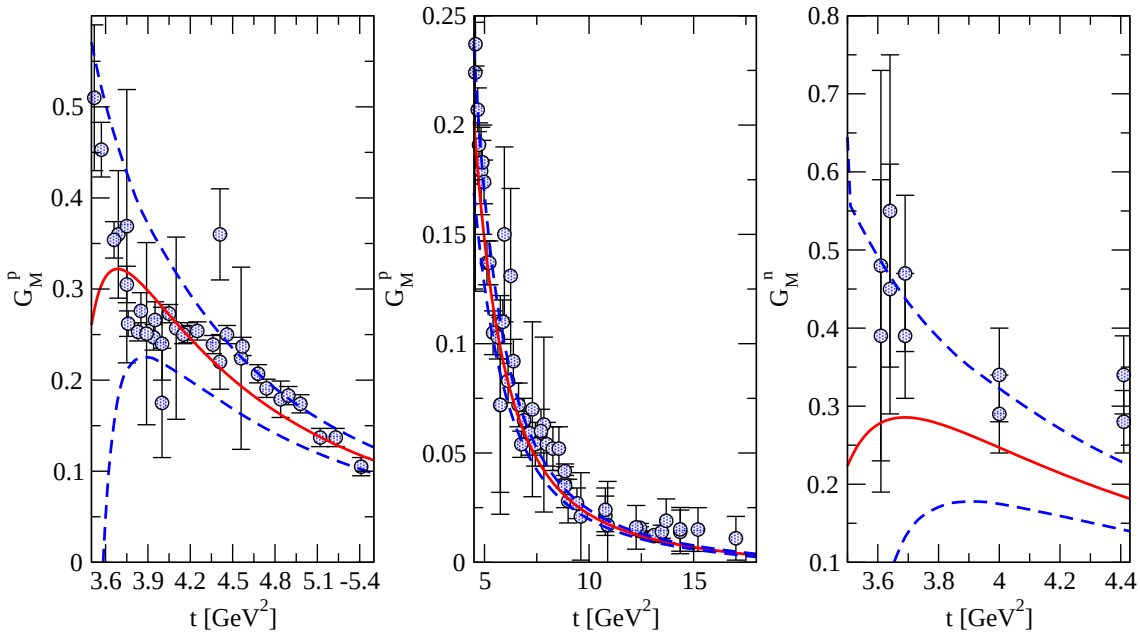

Figure 6.16: Description of the form factors in the timelike region with the inclusion of preliminary CLAS data. The solid lines indicate the best fit result, the dashed lines show the theoretical 1σ uncertainty bands.

phenomenological result for G_M^n would lie between the two datasets. Our analysis clearly strongly favours the preliminary CLAS data. The same result was obtained in the analysis of these two datasets within the SC approach. Some of the world data for G_M^n in the region $Q^2 \approx 0.7$ GeV^2 even lie outside of the theoretical 1σ uncertainty bands. The reason for the discrepancy is not yet understood. In order to further investigate this problem within our approach, an analysis of the differential cross section data would be required.

In the timelike region, the threshold behaviour of the magnetic form factor of the proton is not reproduced. Both experimental points close to threshold lie within our theoretical 1σ uncertainty band, but they are not described by the best fit result. The neutron form factor data, which do not participate in the fit, are mostly within the theoretical uncertainty.

Resonance	Mass [GeV]	a_1 [GeV^2]	a_2 [GeV^2]
ω	0.782	0.669166	−0.135957
s_1	1.045277	−0.025807	0.001144
s_2	1.400423	0.261240	−0.053588
v_1	1.022008	−0.279441	−1.215307
v_2	1.644552	3.823047	−4.561225
v_3	1.770845	−3.849954	4.027035

Table 6.10: Resonance parameters for the fit including the preliminary CLAS data for G_M^n. This fit has 15 free parameters and a total χ^2/dof of 2.2.

a_1^s	a_1^v	b_1 [GeV^{-2}]	c_1 [GeV^{-1}]
−0.000186	−0.026941	0.219241	0.169695
a_2^s	a_2^v	b_2 [GeV^{-3}]	c_2 [GeV^{-1}]
0.000527	−0.001835	0.004155	0.106343

Table 6.11: Parameters of the explicit pQCD term for the fit including the preliminary CLAS data for G_M^n. This fit has 15 free parameters and a total χ^2/dof of 2.2.

6.7 The Proton Charge Radius

In the fits discussed so far, the charge radius of the proton comes out smaller than the result obtained in Lamb shift measurements [Mel99], $r_E^p = 0.883(14)$ fm. Two-photon exchange corrections are not likely to be responsible for this discrepancy [BS05]. In order to investigate this problem, we have performed an analysis of the form factors with the inclusion of a soft constraint (5.6) on r_E^p.

The results for the form factors in the spacelike region are shown on Figure 6.17. Except for G_E^p, a good overall description of the spacelike data is

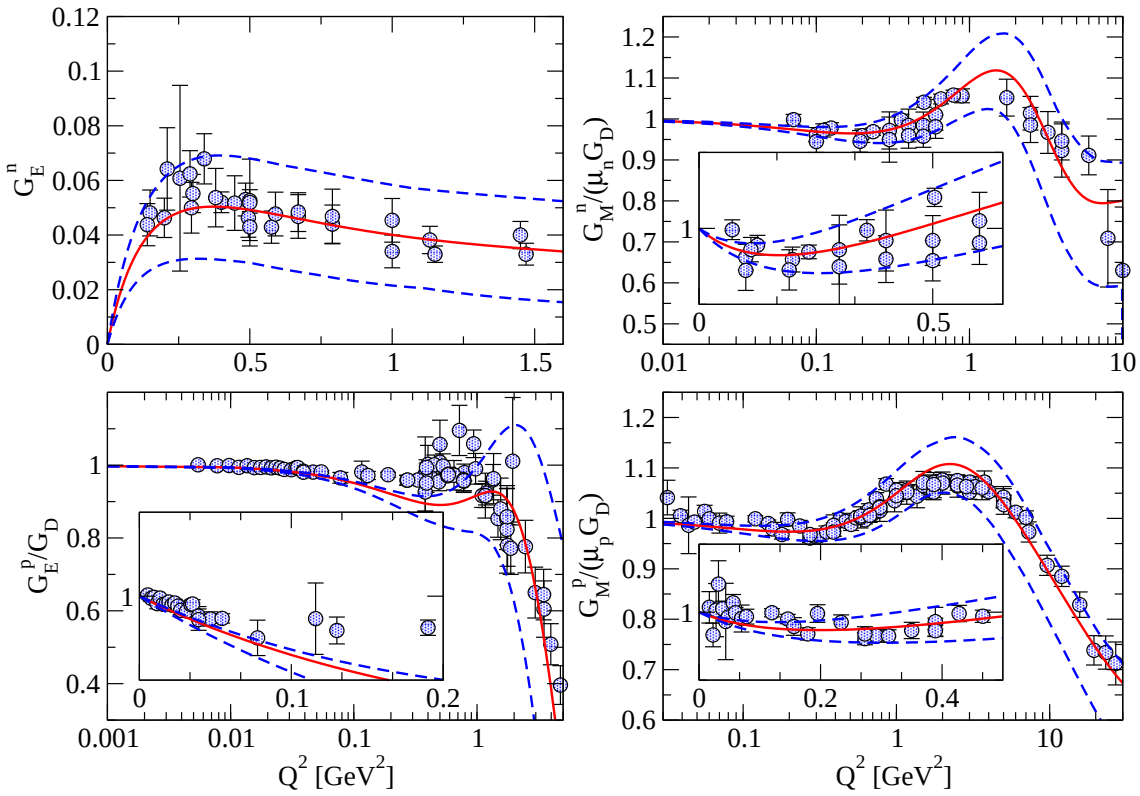

Figure 6.17: Description of the form factors in the spacelike region with the large r_E^p constraint. The solid lines indicate the best fit result, the dashed lines show the theoretical 1σ uncertainty bands.

obtained. No bump-dip structure in G_E^n is observed. Some additional structure in G_E^p appears at $Q^2 \sim 1$ GeV^2. It is not consistent with the experimental data in that range. The low-Q^2 data points for G_E^p are described within the error bars, but the best fit result lies on the lower side of the experimental errors.

The results for the form factors in the timelike region are shown on Figure 6.18. A good description of the proton form factor data is obtained. The neutron form factor data in the timelike region does not participate in the fit. The

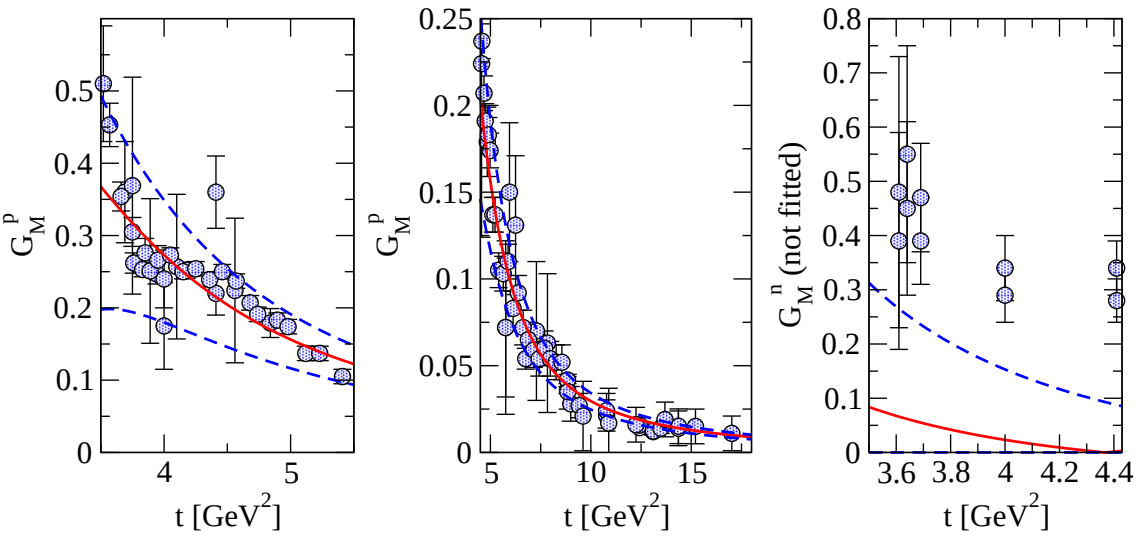

Figure 6.18: Description of the form factors in the timelike region with the large r_E^p constraint. The solid lines indicate the best fit result, the dashed lines show the theoretical 1σ uncertainty bands.

prediction obtained for G_M^n does not describe the FENICE data.

The resonance parameters corresponding to this fit are given in Table 6.12, and the pQCD term parameters in Table 6.13.

Resonance	Mass [GeV]	a_1 [GeV^2]	a_2 [GeV^2]	Γ [GeV^2]
ω	0.782	1.382925	-0.819172	-
ϕ	1.019	-5.879633	7.058426	-
s_1	1.115133	5.829356	-7.428656	-
s_2	1.490044	-0.428048	1.001002	2.701229
v_1	1.000000	1400.860230	-281.350784	-
v_2	1.000266	-1402.617490	280.444607	-
v_3	1.469113	1.507977	-0.951056	-
v_4	4.123999	-0.057065	0.107735	20.876270

Table 6.12: Resonance parameters for the fit with the large r_E^p constraint. This fit has 23 free parameters.

Table 6.14 lists the radii values and error estimates extracted from the analysis. The resulting proton charge radius is comparable to the Lamb shift results. However, the additional structures generated in G_E^p are not supported by the experimental data. In order to reproduce the large r_E^p value, strong soft constraints are required. The determinations of other radii are comparable to the alternative

a_1^s	a_1^v	b_1 [GeV^{-2}]	c_1 [GeV^{-1}]
-0.005412	0.204322	0.538308	0.0
a_2^s	a_2^v	b_2 [GeV^{-3}]	c_2 [GeV^{-1}]
0.085930	-0.074038	0.154637	0.646499

Table 6.13: Parameters of the explicit pQCD term for the fit with the large r_E^p constraint. This fit has 23 free parameters.

Radius	Best value	Error estimate
$(r_E^n)^2$ [fm^2]	-0.118	-0.151 - -0.087
r_E^p [fm]	0.886	0.879 - 0.905
r_M^n [fm]	0.875	0.859 - 0.891
r_M^p [fm]	0.852	0.841 - 0.864

Table 6.14: Radii values and error estimates corresponding to the fit with the large r_E^p constraint.

determinations. Since we perform a global data analysis, we conclude that the current form factor data do not suggest a value of r_E^p as high as predicted in Lamb shift measurements. The inconsistency between the two radii values remains an open question.

6.8 The Meson-Nucleon Coupling Constants

The ωNN and ρNN coupling constants are of great importance, e.g. in the evaluation of isospin violating effects [KL06]. Our model dependent determination of the ρNN coupling constants discussed in Section 6.2, $g^1_{\rho NN} \sim 3.0$ and $\kappa_{\rho NN} \sim 5.9$, is in good agreement with previous results [MMD95] and alternative determinations [Gre77, FW89].

The ωNN coupling constants, however, are not determined so well. Although the vector residua of the ω are fixed relatively well by the fits, $a^1_\omega = 0.60 \ldots 0.83$ GeV^2, even the sign of the tensor residua can not be determined, $a^2_\omega = -0.13 \ldots 0.37$ GeV^2. This leads to the following range for the ωNN coupling constants:

$$g^1_{\omega NN} = 16.7 \ldots 23.1, \text{ and } \mathrm{g}^2_{\omega \mathrm{NN}} = -3.6 \ldots 10.3. \tag{6.7}$$

We have not extracted the coupling of the ϕ to the nucleon because the ϕ strength also appears in the $K\bar{K}$, $\rho\pi$ and other continua such as $\bar{K}^*K - \bar{K}K^*$, $\bar{K}^*K^*$ and $\Sigma\bar{\Sigma} + \Lambda\bar{\Lambda}$ [MMSO97] which are not included in our analysis. The interpretation of the ϕ pole is therefore ambiguous.

Chapter 7

Results of the Cross Section Analysis

In this Chapter, our results of the direct analysis of the elastic unpolarised electron-proton differential cross section data with the inclusion of Coulomb corrections are presented. The results are in better agreement with polarisation transfer data in comparison to the original Rosenbluth analyses which do not include Coulomb corrections. We have employed a comparison of the Rosenbluth cross section data to the phenomenological cross sections obtained using the form factor analyses described in the previous Chapter in order to provide an estimate for the two-photon exchange effects. The results agree with alternative determinations, and explain the discrepancy between the Rosenbluth and the polarisation transfer data when applied to cross section data directly.

7.1 Analysis of the Cross Section Data

We have performed a direct analysis of the unpolarised elastic electron-proton scattering cross sections with the inclusion of Coulomb corrections. Instead of including the spacelike proton form factors, the world data on the differential cross sections was used. The Rosenbluth formula (4.1) was used to construct the differential cross section using our phenomenological form factors, and the same minimisation techniques as for the form factors employed in order to perform the fits.

7.1.1 Superconvergence Approach

Figure 7.1 shows the results obtained in the cross section analysis within the SC approach for several sample cross section ranges - two for fixed electron incoming energies (left panel), and two for fixed electron scattering angles (right panel). A comparison to all experimental data is given in Table 8.1 in the Appendix. Figure 7.2 shows the ratio $\mu_p G_E^p / G_M^p$ extracted from the analysis. The dash-dotted line corresponds to an analysis of all the cross section data without the inclusion of the Coulomb corrections. The timelike data were excluded from the latter analysis. The χ^2 for the spacelike data corresponding to the fit without Coulomb corrections is $\chi^2_s = 1.1$, and the parameter values are only slightly different than the parameter values corresponding to the best fit discussed in this Section. The result is in qualitative agreement with the analysis that includes the Coulomb corrections, but shows larger deviations in comparison to the polarisation transfer data.

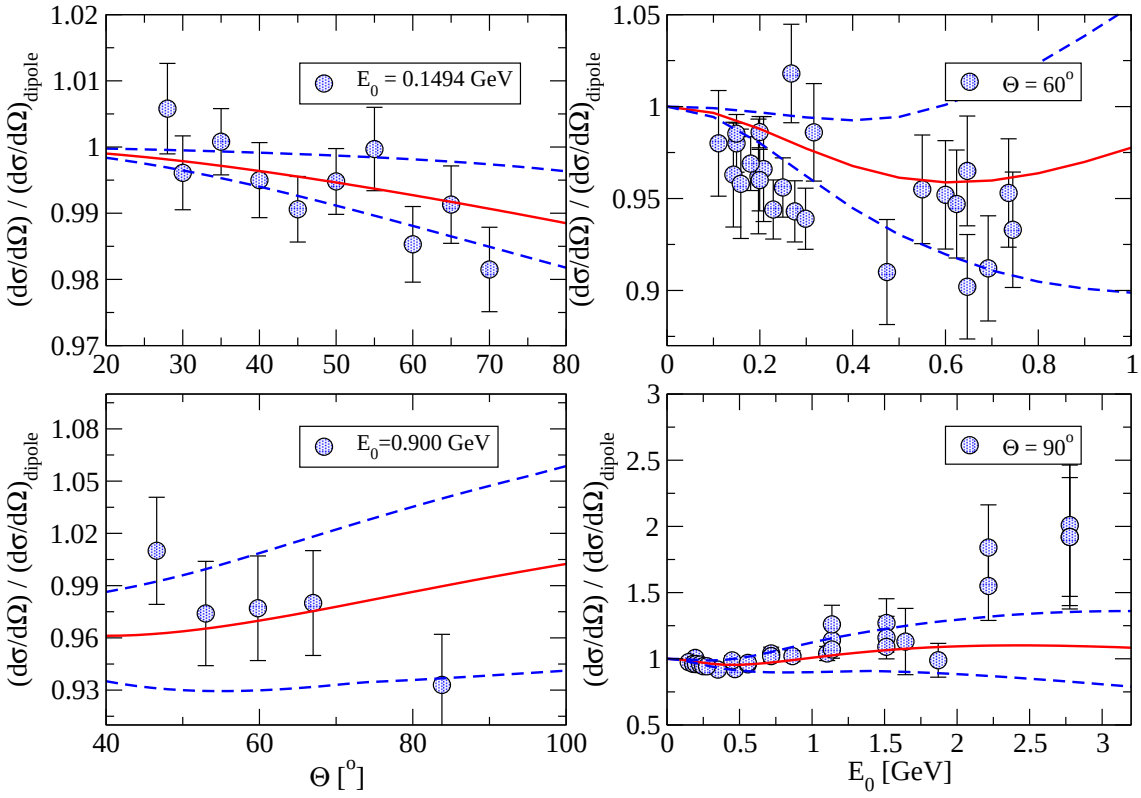

Figure 7.1: The differential cross section normalised to the dipole cross section obtained from the cross section analysis in the SC approach compared to experimental data. The solid lines indicate the best fit result, the dashed lines are the theoretical uncertainty estimates.

Figure 7.3 shows the results for the form factors in the spacelike region and Figure 7.4 the results for the form factors in the timelike region. This fit has 12

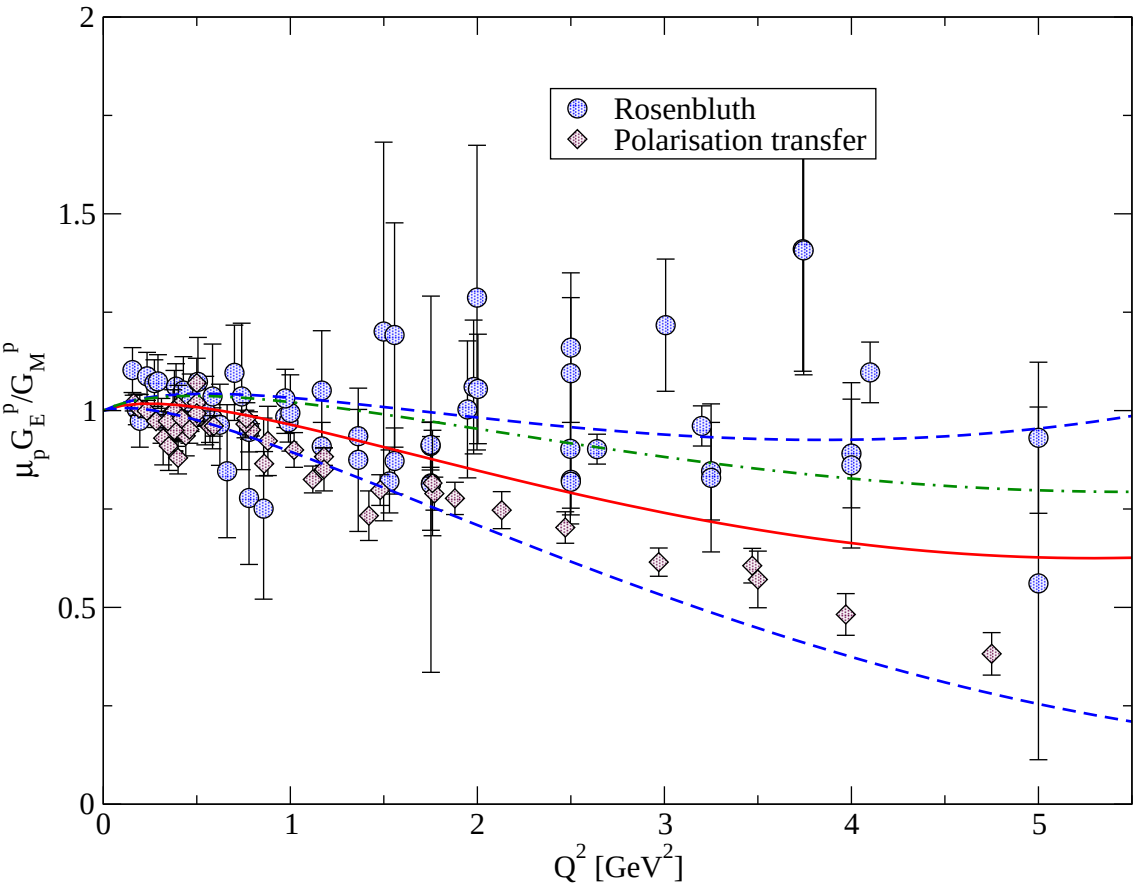

Figure 7.2: The ratio $\mu_p G_E^p / G_M^p$ extracted from the cross section analysis in the SC approach. The solid lines indicate the best fit result, the dashed lines are the theoretical uncertainty estimates. The dash-dotted line corresponds to a cross section analysis within the SC approach without the inclusion of Coulomb corrections. The time-like data were not included in the latter analysis.

free parameters and a total χ^2/dof of 1.4. The χ^2/dof for spacelike data only (cross section data and the neutron form factor data) is 0.86.

The first important - and unexpected - result is the ratio of the electric and magnetic form factors. While the discrepancy between the Rosenbluth and the polarisation transfer experiments has long been known, our analysis of the form factor data within the Rosenbluth framework produces a result which is in much better agreement with the polarisation transfer data than the original Rosenbluth form factor analyses suggest. Some of the $\mu_p G_E^p / G_M^p$ data extracted using the Rosenbluth technique lie outside our theoretical uncertainty band. The reasons for this discrepancy are two-fold. First, the inclusion of the Coulomb corrections is an important factor for the analysis of the cross section data. Secondly, our approach to the analysis does not have an explicit problem of the dominance of the magnetic form factor at large momentum transfers - the sensitivity to small changes in the

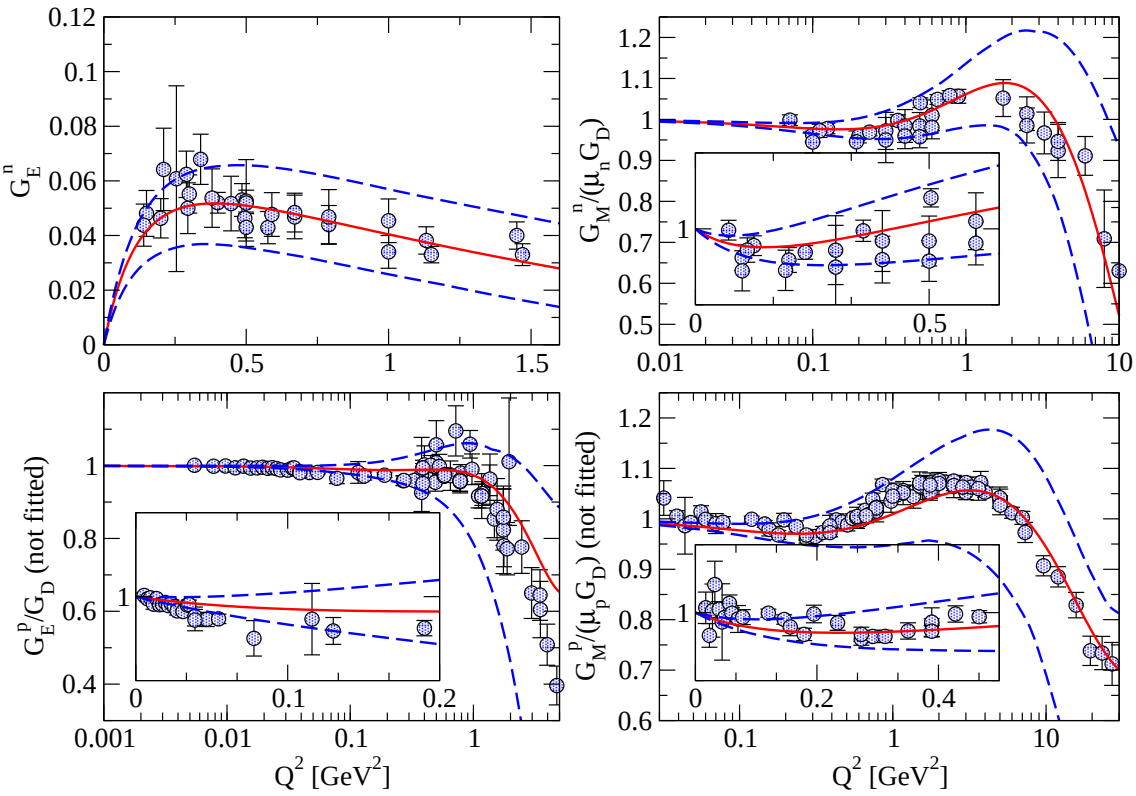

Figure 7.3: Description of the form factors in the spacelike region from a direct cross section analysis within the SC approach. The form factors of the proton in the spacelike region did not participate in the fit. The solid lines indicate the best fit result, the dashed lines show the theoretical 1σ uncertainty bands.

electric form factors is improved when analysing all available data in the full range of the outgoing electron angles θ, and no additional uncertainties are introduced.

The extracted form factors in the spacelike region are also in much better agreement with the polarisation transfer results than the original Rosenbluth analyses suggest. Moreover, the polarisation transfer data lie within the 1σ theoretical uncertainty bands obtained by the analysis of the cross section data.

These results are a first indication that the discrepancy that is attributed to two-photon corrections is not as dramatic as previously thought. Secondly, by analysing the difference between the cross sections obtained from the form factors describing the polarisation transfer form factor data and the cross section analysis performed here one can obtain a model-independent theoretical estimates for the magnitude of the two-photon effects.

The interference between the Born and the two-photon exchange amplitudes changes sign when the charge of one of the particles if flipped. An experiment aimed at measuring the two-photon exchange effects through the asymme-

try in electron-proton and positron-proton scattering is in preparation at Jefferson Lab, experiment E04-116, and a similar experiment has been proposed at VEPP-3. Therefore, a theoretical prediction in addition to the model-dependent calculations discussed in Section 4.4 is a very important step.

Resonance	Mass [GeV]	a_1 [GeV^2]	a_2 [GeV^2]	Γ [GeV^2]
ω	0.782	0.589337	0.459612	-
ϕ	1.019	0.183528	−2.659541	-
s_1	1.163239	0.084414	2.115484	-
s_2	2.339565	0.047321	−0.103954	17.038504
v_1	1.008434	−0.757949	−0.849667	-
v_2	1.281405	16.226588	−5.205650	-
v_3	1.304220	−15.725391	4.143527	-
v_4	2.922907	−0.049596	0.162292	23.6932

Table 7.1: Resonance parameters for the fit to cross section data within the SC approach. This fit has 12 free parameters and a total χ^2/dof of 1.4.

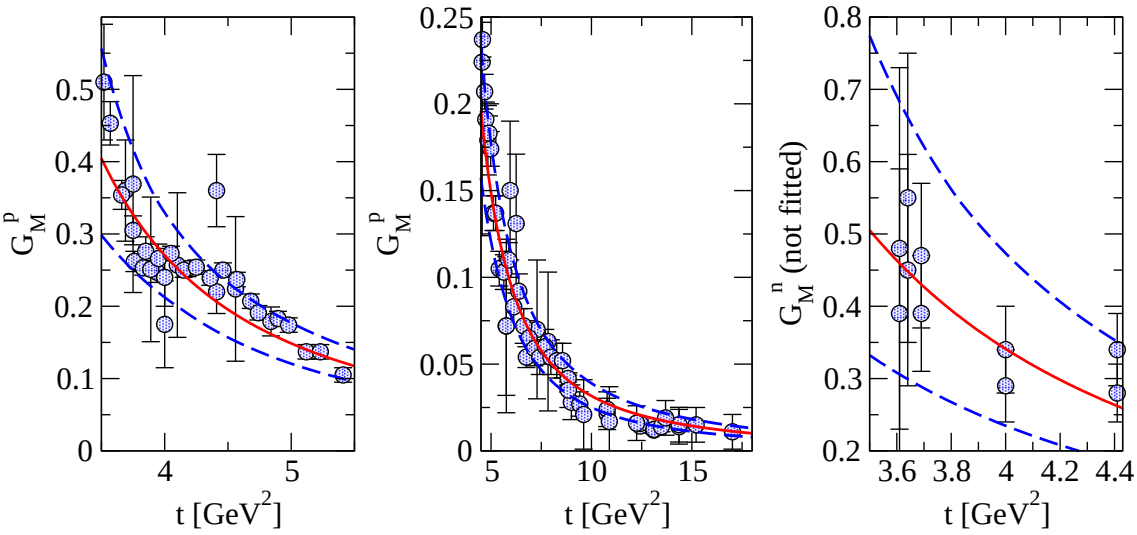

Figure 7.4: Description of the form factors in the timelike region from a direct cross section analysis within the SC approach. The solid lines indicate the best fit result, the dashed lines show the theoretical 1σ uncertainty bands.

7.1.2 pQCD Approach

We have also performed an analysis of the cross section data within the pQCD approach. We have additionally investigated the sensitivity of the solution to the high-Q^2 behaviour of G_E^p as follows:

- We impose a soft constraint on the high-Q^2 behaviour of G_E^p using Eq. (5.6). We start by setting a central value $(G_E^p(Q^2)/G_D(Q^2))\,|_{Q^2=7\,\mathrm{GeV}^2} \sim 1$, which corresponds to the dipole behaviour of G_E^p. After performing a fit with this constraint in place, we vary the constrained value slowly down to $(G_E^p(Q^2)/G_D(Q^2))\,|_{Q^2=7\,\mathrm{GeV}^2} \sim 0.7$, which favours the polarisation transfer data.
- We study the response of the χ^2 function in response to varying the strength parameter κ of the constraint as the central constraint value varies. The strength parameter is adjusted in such a way that the contribution of the constraint to the χ^2 value does not exceed $\approx 1\%$ of the χ^2.

We find that variations of G_E^p as large as 20% at $Q^2 \approx 7$ GeV^2 do not affect the χ^2 - variations of the χ^2 function are less than 1%. The main reason for this result are the large errors on the high-Q^2 experimental data points for the cross sections. We stress that a global analysis features improved sensitivity to the ϵ dependence when compared to analyses of the individual experiments.

As in the SC approach, we find a final result which is more compatible with the polarisation transfer data than the world Rosenbluth data suggest. Figure 7.5 shows the results obtained in the cross section analysis within the pQCD approach for several sample cross section ranges - two for fixed electron incoming energies (left panel), and two for fixed electron scattering angles (right panel). A comparison to all experimental data is given in Table 8.2 in the Appendix. Figure 7.6 shows the ratio $\mu_p G_E^p/G_M^p$ extracted from the analysis. The results for the ratio $\mu_p G_E^p/G_M^p$ are again closer to the polarisation transfer results than the original Rosenbluth data suggest. Figure 7.7 shows the results for the form factors in the spacelike region and Figure 7.8 the results for the form factors in the timelike region. This fit has 20 free parameters and a total χ^2/dof of 1.14. The χ^2/dof for spacelike data only (cross section data and the neutron form factor data) is 0.91, slightly higher than in the SC approach.

By comparing Figures 7.6 and 7.2, we observe that the SC approach result is much more compatible with the polarisation transfer data, while featuring a marginally larger χ^2 value. The deviations of the pQCD approach results from the polarisation transfer data become more significant at increasing Q^2 values. In the following section, we compare both of these results to the results of our analyses of the form factors in order to obtain a model-independent estimate of the magnitude of the corrections not present in the treatment of Mo and Tsai. Due to the fact that

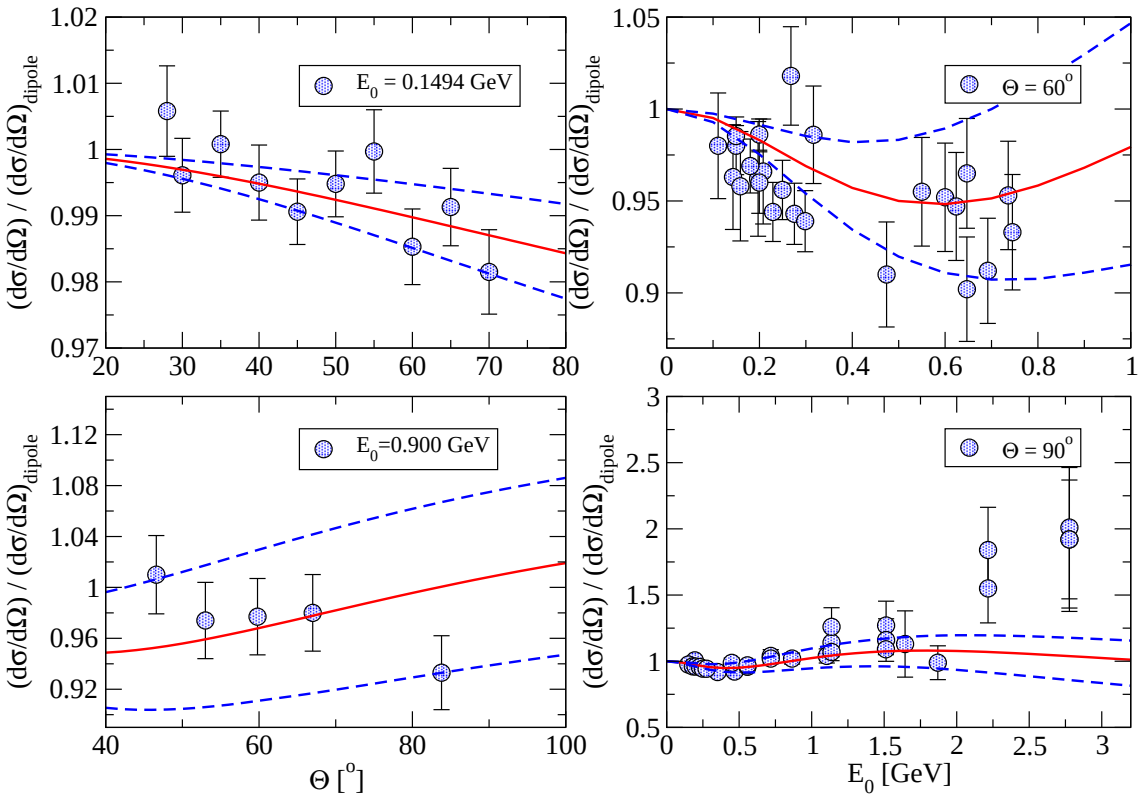

Figure 7.5: The differential cross section normalised to the dipole cross section obtained from the cross section analysis in the pQCD approach compared to experimental data. The solid lines indicate the best fit result, the dashed lines are the theoretical uncertainty estimates.

Resonance	Mass [GeV]	a_1 [GeV^2]	a_2 [GeV^2]
ω	0.782	0.922627	0.542880
ϕ	1.019	−4.669677	−6.351886
s_1	1.076079	5.040852	5.817876
s_2	1.829403	−0.389202	−0.197270
v_1	0.950331	−0.170927	−0.886366
v_3	1.691873	5.201568	−10.000607
v_2	1.764510	−5.336988	9.137475

Table 7.2: Resonance parameters for the fit to the cross section data within the pQCD approach. This fit has 20 free parameters and a total χ^2/dof of 1.14.

the pQCD results deviate from the polarisation transfer results more strongly, we expect a larger estimate to emerge from this analysis.

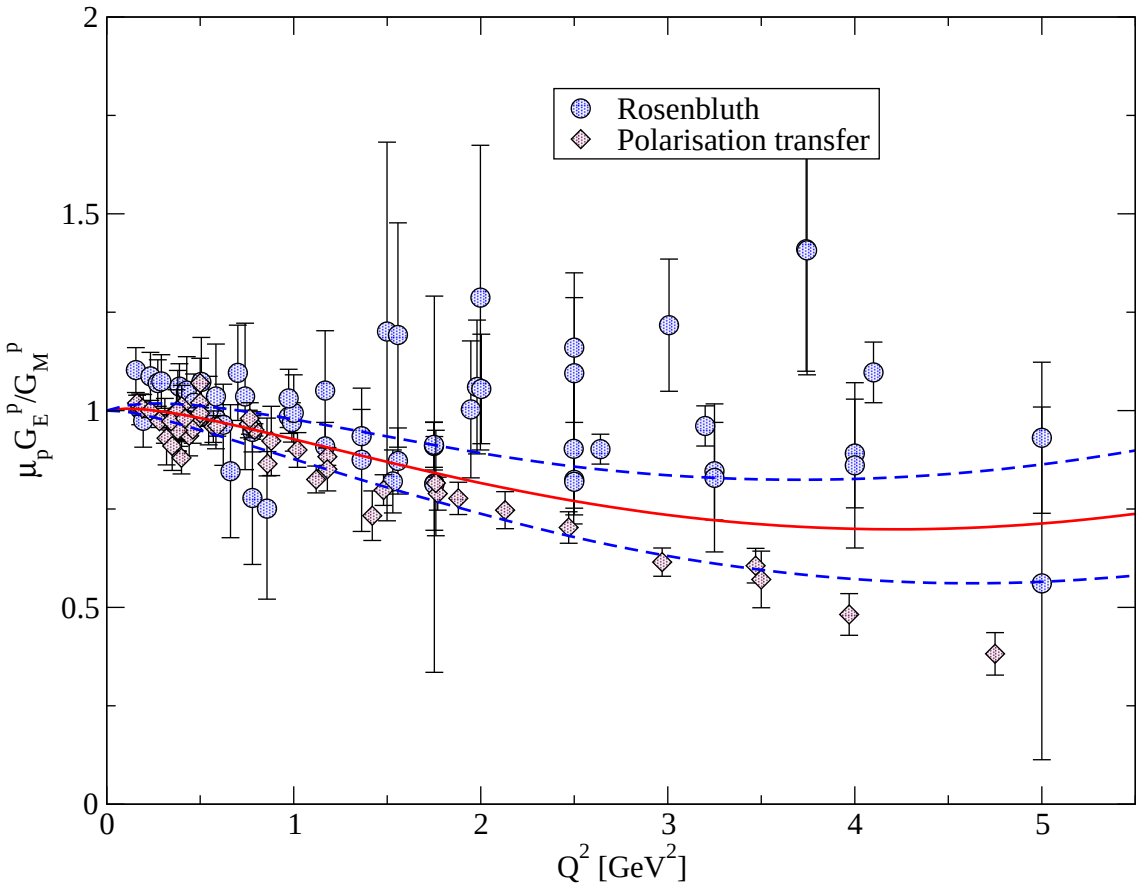

Figure 7.6: The ratio $\mu_p G_E^p/G_M^p$ extracted from the cross section analysis in the pQCD approach. The solid lines indicate the best fit result, the dashed lines are the theoretical uncertainty estimates. The uncertainty comes out somewhat smaller than in the SC approach due to the particular configuration of the parameter space in the vicinity of the minimum. Both approaches agree well within the theoretical 1σ uncertainty bands.

a_1^s	a_1^v	b_1 [GeV^{-2}]	c_1 [GeV^{-1}]
-0.044889	-0.022396	0.254491	0.426109
a_2^s	a_2^v	b_2 [GeV^{-3}]	c_2 [GeV^{-1}]
0.016038	-0.027308	0.000104	0.727139

Table 7.3: Parameters of the explicit pQCD term for the fit to the cross section data within the pQCD approach. This fit has 20 free parameters and a total χ^2/dof of 1.14.

7.2 Two-Photon Exchange Effects

At present, the difference between the form factors extracted using the Rosenbluth and the polarisation transfer methods provides indirect access to two-photon ex-

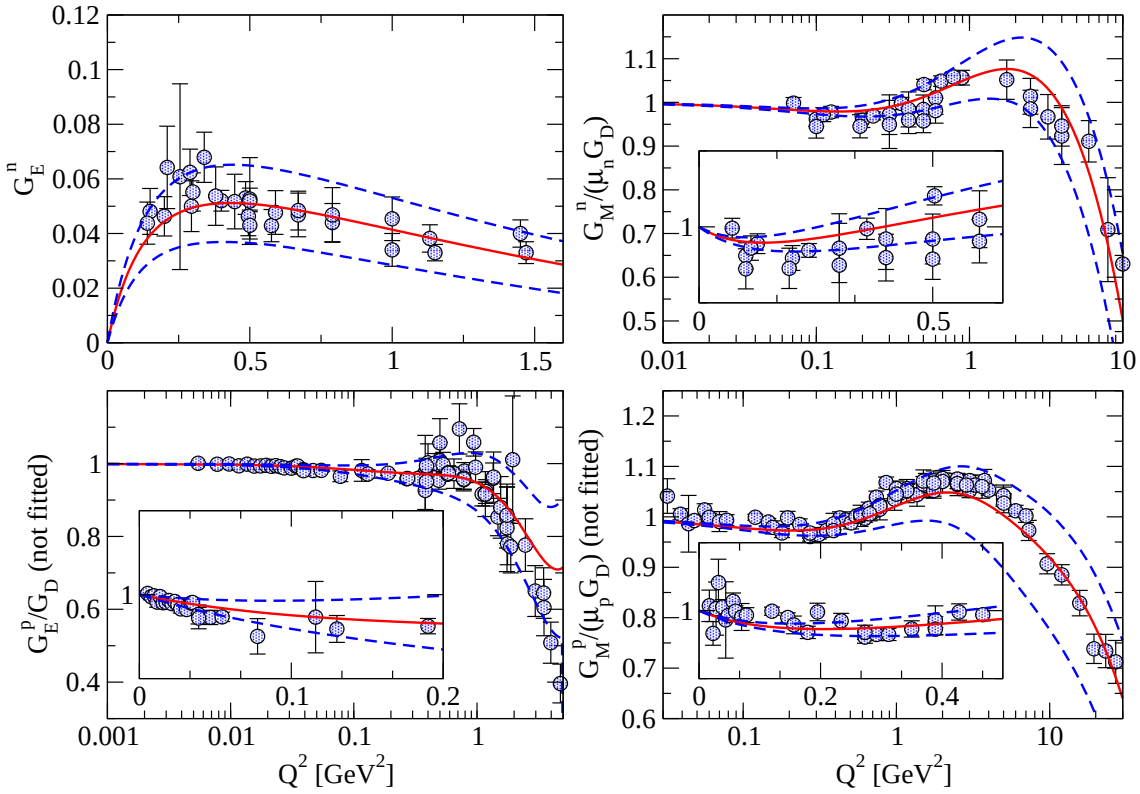

Figure 7.7: Description of the form factors in the spacelike region from a direct cross section analysis within the pQCD approach. The form factors of the proton in the spacelike region did not participate in the fit. The solid lines indicate the best fit result, the dashed lines show the theoretical 1σ uncertainty bands.

change effects. Other higher-order corrections may be responsible for some part of this problem, however.

In order to evaluate the two-photon and other corrections not present in the treatment of Mo and Tsai, we compare out results of the analysis of the polarisation transfer form factor data with our results of the unpolarised elastic electron-proton differential cross section analysis. Because the two-photon effects are negligible in the polarisation transfer technique [BMT05], we construct the cross section using our analysis of the polarisation transfer data for the form factors,

$$\left(\frac{d\sigma}{d\Omega}\right)_{\mathrm{PT}} = \left(\frac{d\sigma}{d\Omega}\right)_{\mathrm{Mott}} \left[\frac{G_E^2 + \tau G_M^2}{1+\tau} + 2\tau G_M^2 \tan^2(\theta/2)\right] , \tag{7.1}$$

using the Rosenbluth expression. $(d\sigma/d\Omega)_{\mathrm{PT}}$ is then the cross section in the one-photon exchange approximation free of two-photon effects.

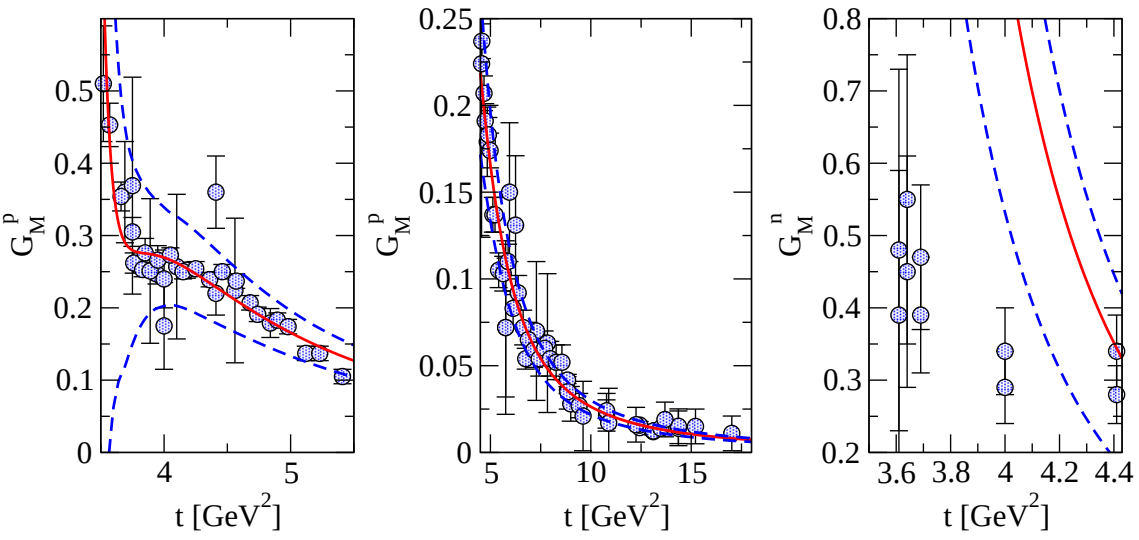

Figure 7.8: Description of the form factors in the timelike region from a direct cross section analysis within the pQCD approach. The solid lines indicate the best fit result, the dashed lines show the theoretical 1σ uncertainty bands.

7.2.1 Results of the Superconvergence Approach

We use our results $(d\sigma/d\Omega)_{\rm Ros}$ of the direct ep cross section analysis of Section 7.1.1 in order to obtain an estimate of the additional two-photon effects not included in the standard correction given by Mo and Tsai [MT68]. We use Eq. (4.7) to now relate $(d\sigma/d\Omega)_{\rm PT}$ and $(d\sigma/d\Omega)_{\rm Ros}$:

$$\left(\frac{d\sigma}{d\Omega}\right)_{\rm Ros} = \left(\frac{d\sigma}{d\Omega}\right)_{\rm PT} (1+\Delta^{2\gamma})\,, \tag{7.2}$$

where $\Delta^{2\gamma}$ are the missing corrections responsible for the discrepancy. In what follows, we assume that two-photon exchange is responsible for the difference. Therefore,

$$\Delta^{2\gamma} = \left(\frac{d\sigma}{d\Omega}\right)_{\rm Ros} \Big/ \left(\frac{d\sigma}{d\Omega}\right)_{\rm PT} - 1\,. \tag{7.3}$$

The propagation of errors for $\Delta^{2\gamma}$ is performed in the standard manner. Using a short-hand notation, $\sigma_1 \equiv \left(\frac{d\sigma}{d\Omega}\right)_{\rm Ros}$, $\sigma_2 \equiv \left(\frac{d\sigma}{d\Omega}\right)_{\rm PT}$,

$$\delta\Delta^{2\gamma} = \sqrt{\left(\frac{\partial\Delta^{2\gamma}}{\partial\sigma_1}\delta\sigma_1\right)^2 + \left(\frac{\partial\Delta^{2\gamma}}{\partial\sigma_2}\delta\sigma_2\right)^2 + 2\frac{\partial\Delta^{2\gamma}}{\partial\sigma_1}\frac{\partial\Delta^{2\gamma}}{\partial\sigma_2}{\rm cov}(\sigma_1,\sigma_2)}\,, \tag{7.4}$$

where ${\rm cov}(\sigma_1,\sigma_2) = \langle\sigma_1\sigma_2\rangle - \langle\sigma_1\rangle\langle\sigma_2\rangle$. In our approach, the cross sections are not treated as independent random variables. For a known $\Delta^{2\gamma}$, i.e. taken from future experimental results or the analysis of [BMT05], the knowledge of one cross section

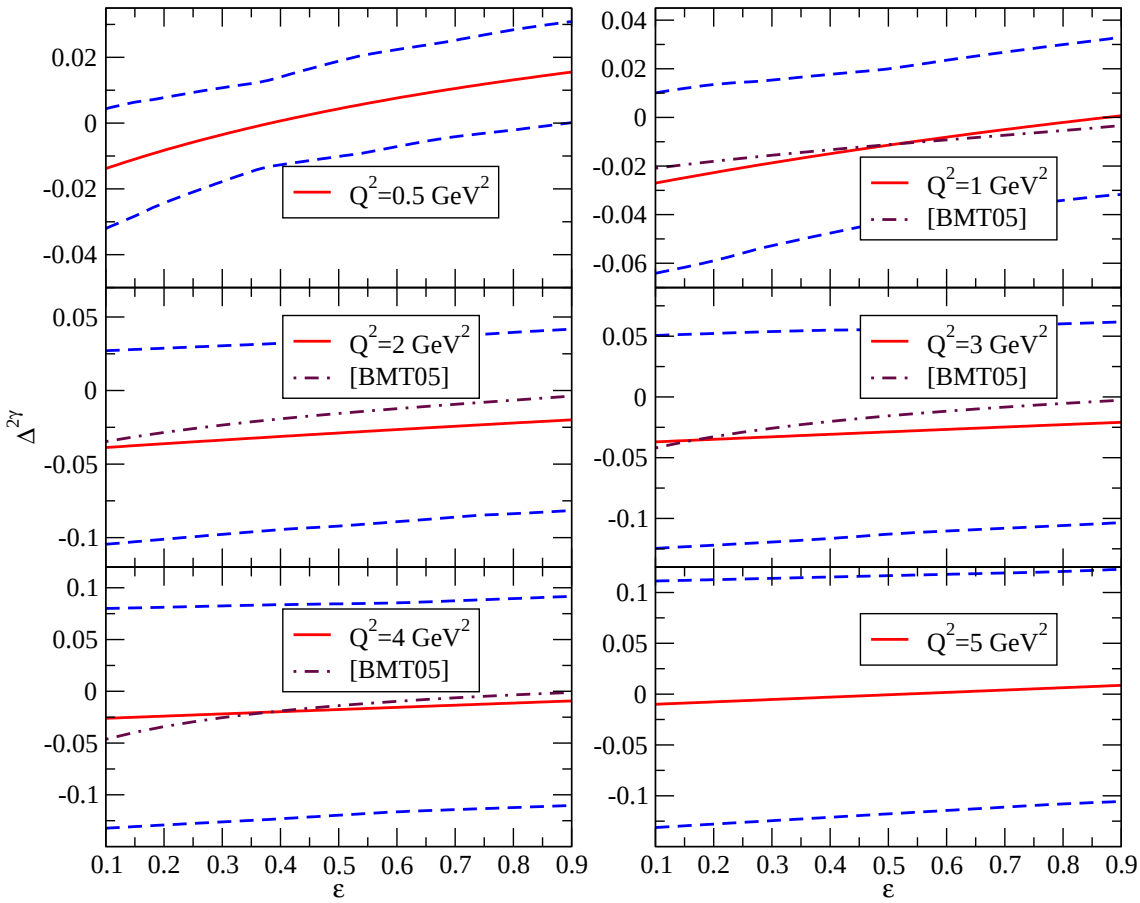

Figure 7.9: Results for $\Delta^{2\gamma}$ within the SC approach for several values of Q^2. The solid lines indicate the best fit result, the dashed lines are the theoretical uncertainty bands. The dash-dotted line corresponds to the analysis of Ref. [BMT05].

uniquely determines the other. Therefore, we include the covariance tensor element in Eq. (7.4). Since the cross sections are connected via Eq. (7.2), the covariance tensor element can be calculated explicitly,

$$\mathrm{cov}(\sigma_1, \sigma_2) = (\delta\sigma_2)^2(1 + \Delta^{2\gamma})\,. \tag{7.5}$$

Our results for $\Delta^{2\gamma}$ can be directly compared to the results of the calculation of Blunden, Melnitchouk and Tjon [BMT05] and Afanasev *et al.* [ABCC05, CABC04].

Our result for $\Delta^{2\gamma}(Q^2, \epsilon)$ are shown on Figure 7.9. Numerical results are given in Table 8.3 in the Appendix. The correction depends linearly on ϵ, which is in agreement with the linear discrepancy between the form factor ratios (Figure 4.5) since the reduced cross section depends linearly on ϵ.

Our determination is in very good agreement with the determinations of

Blunden *et al.* [BMT05]. Our results agree well with the calculation of Afanasev *et al.* [ABCC05, CABC04]. At $Q^2 = 5$ GeV^2, the $\Delta^{2\gamma}$ correction to the differential cross section crosses zero at $\epsilon \sim 0.5$, and becomes positive at larger values of ϵ.

7.2.2 Results of the pQCD Approach

We use the results of the form factor analysis discussed in Section 6.4 and the results of the cross section analysis detailed in Section 7.1.2 in order to obtain an estimate for $\Delta^{2\gamma}$ within the pQCD approach. The results are shown on Figure 7.10. The numerical results are given in Table 8.3 in the Appendix.

As already discussed, estimates significantly larger than the results of the SC approach for high Q^2 values are obtained. At $Q^2 < 2$ GeV^2, the analysis is still in good agreement with the findings of Ref. [BMT05]. The results indicate that the possibility of further corrections, i.e. from the inclusion of excited intermediate nucleon states in the calculation of the two-photon exchange diagrams and higher order corrections, is not ruled out, and could have a significant impact on $\Delta^{2\gamma}$.

Overall, our estimate of the two-photon effects is in qualitative and quantitative agreement with alternative determinations. It is derived directly from cross section data. Applying the two-photon exchange corrections to the unpolarised cross section data has the potential to resolve the discrepancy between the Rosenbluth and the polarisation transfer techniques within experimental errors. In order to apply the corrections to the form factors, a careful reanalysis of the Rosenbluth results with the inclusion of the Coulomb corrections to the cross section data is required. It is important to stress that a global reanalysis of all the available unpolarised cross section data is required, since, as already mentioned, these data are consistent with each other only within one given experiment [Arr03]. It is also important to further investigate the sensitivity of such a global analysis to the variation of G_E^p - the estimates of the missing corrections within the SC approach show that good agreement between the Rosenbluth and the polarisation transfer techniques can be achieved with the current state of the experimental data if the two-photon corrections are applied to cross section data.

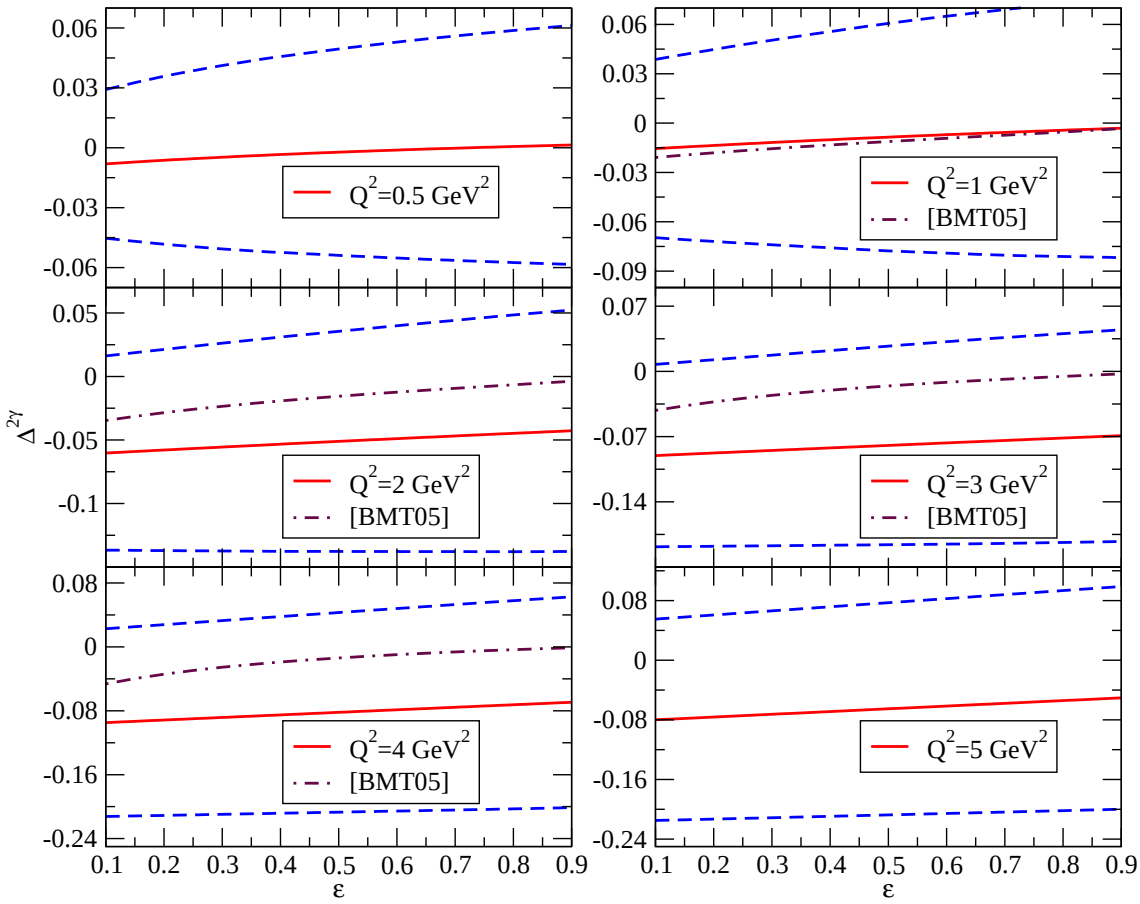

Figure 7.10: Results for $\Delta^{2\gamma}$ within the pQCD approach for several values of Q^2. The solid lines indicate the best fit result, the dashed lines are the theoretical uncertainty bands. The dash-dotted line corresponds to the analysis of Ref. [BMT05].

Chapter 8

Summary and Outlook

We have investigated the problem of the structure of the nucleons using dispersion relation techniques. Our analysis differs from the previous analyses in several ways:

- We have explicitly included the two-pion, $K\bar{K}$ and $\rho\pi$ continua all together as fixed contributions. The two-pion and the $K\bar{K}$ contribution are determined from unitarity and experimental data, and the $\rho\pi$ contribution comes from a model calculation.
- Two models to enforce the correct asymptotic form factor behaviour and, at the same time, to provide a parameterisation of the continua which are not explicitly included have been developed as part of this work.
- We have analysed all four form factors simultaneously in both the spacelike and the timelike regions.
- A rigorous investigation of the possibility of additional structure in G_E^n, the bump-dip structure, has been performed in our analysis.
- The preliminary CLAS data for G_M^n have been included for the first time.
- Our analysis of the elastic unpolarised electron-proton scattering cross section data has produced results which suggest the discrepancy between the Rosenbluth and the polarisation transfer techniques is not as dramatic as the original data suggest.
- The cross section analysis has allowed us to provide model-independent estimates of the two-photon exchange effects, which are in agreement with other calculations. The two-photon corrections are indeed capable of resolving the discrepancy between the Rosenbluth and the polarisation transfer techniques within the experimental errors.

- For the first time, we have developed a consistent method for generating the 1σ error bands on the results of our analyses.
- Our approach complies with the Phragmen-Lindeloff theorem, which states that the asymptotic limit of an analytic function on the complex plane is the same regardless of the direction in which it is taken. The superconvergence relations ensure that the form factors in the space- and the timelike regions are asymptotically real and equal.

Our analyses of the form factors within both the SC and the pQCD approaches have provided results which are in very good agreement with the available experimental data. We have given all the parameters required to reproduce the form factors, as well as error estimates for both the form factors and the nucleon radii. Our results can be easily incorporated into other calculations which depend on the knowledge of the form factors of the nucleons - for example, the analysis of the structure of the deuteron. We have investigated the threshold behaviour of the magnetic form factor of the proton in the timelike region, and conclude that while a resonance just below threshold is not excluded, it is neither required nor does its presence necessarily generate the steep threshold enhancement. We have also given a prediction for the Q^2 range where the asymptotic behaviour of the form factors becomes apparent, and have presented results consistent with the experimental data for the ratio $QF_2(Q^2)/F_1(Q^2)$. Our results for the nucleon radii and their error estimates are consistent with alternative determinations, with the exception of the proton charge radius, r_E^p, which comes out significantly smaller than the result given by Lamb shift measurements. The reason for this discrepancy is not yet understood.

Our analysis of the possibility of additional structure in G_E^n at low momentum transfers has given results consistent with the results of Friedrich and Walcher. A significant modification of the two-pion pion contribution is required to reproduce this behaviour. Such a modification, however, is at odds with unitarity. Moreover, preliminary data for the neutron electric form factor from MAMI do not support the bump-dip structure hypothesis. We conclude that the neutron electric form factor is smooth, and our best fits within both the SC and the pQCD approaches provide correct results for its low-Q^2 behaviour.

The investigation of the preliminary data for G_M^n from the CLAS collaboration that we have undertaken has provided results which favour the CLAS data. Some of the world data do not even fall within our 1σ error bands in the region of the discrepancy. The physical meaning of this result is not yet well understood. A combined analysis of all the original cross section data within our approach could give an insight into this problem.

We have also extended the investigation of the structure of the nucleons to a direct analysis of the unpolarised elastic electron-proton differential cross section data. The Coulomb corrections have been included. Our results indicate that a good description of the cross section data can be obtained with form factors which are in much better agreement with polarisation transfer data than the previous

results of the analysis of the data from individual experiments suggest. To this end, a global reanalysis of the Rosenbluth technique data with the inclusion of the Coulomb corrections is required in order to obtain the data for the form factors.

Using our results, we have also presented a model-independent estimate of the two-photon exchange effects. We find values for the two-photon exchange corrections which are consistent with previous model calculations if we use the Coulomb-corrected global analysis of the cross section data. We conclude that the two-photon effects indeed explain the long-standing problem of the discrepancy between the two techniques, but one must compare to the original data for the cross sections, or reanalyse the form factors extracted using the Rosenbluth technique globally.

There are several areas in which future improvement of our approach can be made.

- The number of free parameters in the fits should further be reduced. This may be possible through a detailed analysis of our results for the unknown continuum contributions in order to provide fixed estimates for use in future fits. The development of more efficient Monte-Carlo sampling techniques may also help reduce the number of effective poles required to reproduce the data.

- The current method of generating the error bands on our results does not take into account the fact that some of the experimental form factor data are strongly correlated. This can be solved by introducing an explicit correlation function into the Monte-Carlo sampling technique. This requires the calculation of the covariance tensor for those experimental data points which are correlated, and including it in the computation of the errors in a similar way as described by Eq. (7.4).

- Two-photon exchange corrections should be further investigated. The results of Blunden *et al.* and Afanasev *et al.* should be independently applied to the unpolarised elastic electron-proton differential cross section data, and a global analysis of the resulting cross sections performed. The result of the analysis should be compared to polarisation transfer data, as well as the experimental results for the two-photon effects when they appear.

- The difference between the results of the form factor analyses and the Lamb shift measurements for the proton charge radius remains a mystery, and is not explained by two-photon effects. It is important to eventually understand the reasons for this discrepancy.

- The threshold enhancement of the proton magnetic form factor in the timelike region is not well described with the current amount of available experimental data. It should be reanalysed when new data from experiments currently in preparation arrives.

- The difference between the CLAS data for G_M^n and the world data for the magnetic form factor of the neutron should be further investigated through a cross section analysis.
- Finally, when a compilation of all available experimental information for the cross sections and polarisation observables becomes available, fits to cross sections for the proton and polarisation observables for the proton and the neutron should be performed in the space- and timelike regions. This provides a global data analysis, and removes any model assumptions in the extraction of the form factors.

Although a large number of good results have been obtained, and a number of long standing problems resolved, many open questions still remain. With new experiments in preparation aimed at measuring the form factors with high precision at higher and higher Q^2 values, this analysis should be compared to, and updated with, the upcoming results. Results from future experiments on two-photon physics should also be included in the analysis. Cross section data is also vital for the continuation of this work. Analysis of cross sections not only provides a gateway into two-photon physics, but may also help explain and resolve certain discrepancies in the data coming from different experiments.

Appendix

Results of the fit to cross section data within the SC approach

Table 8.1 gives the numerical results of the analysis of the cross section data for unpolarised elastic electron-proton scattering within the SC approach compared to the experimental data.

Q^2 [GeV^2]	E [GeV]	θ [^{o}]	$\left(\frac{d\sigma}{d\Omega}\right)_{\rm exp}$ / $\left(\frac{d\sigma}{d\Omega}\right)_{\rm dipole}$	$\left(\frac{d\sigma}{d\Omega}\right)_{\rm SC}$ / $\left(\frac{d\sigma}{d\Omega}\right)_{\rm dipole}$
0.006	0.149	30.000	0.996 ± 0.006	$0.998^{+0.001}_{-0.001}$
0.008	0.149	35.000	1.001 ± 0.005	$0.997^{+0.001}_{-0.001}$
0.010	0.149	40.000	0.995 ± 0.006	$0.996^{+0.001}_{-0.001}$
0.011	0.082	85.190	1.000 ± 0.010	$0.995^{+0.001}_{-0.001}$
0.012	0.082	85.180	0.995 ± 0.006	$0.995^{+0.001}_{-0.001}$
0.012	0.111	60.000	0.980 ± 0.029	$0.996^{+0.001}_{-0.001}$
0.012	0.144	45.000	1.012 ± 0.025	$0.996^{+0.001}_{-0.001}$
0.012	0.149	45.000	0.991 ± 0.005	$0.995^{+0.001}_{-0.001}$
0.013	0.150	45.000	0.974 ± 0.016	$0.995^{+0.001}_{-0.001}$
0.013	0.090	84.780	0.996 ± 0.006	$0.995^{+0.001}_{-0.002}$
0.014	0.200	35.000	1.000 ± 0.006	$0.995^{+0.001}_{-0.001}$
0.015	0.149	50.000	0.995 ± 0.005	$0.994^{+0.002}_{-0.002}$
0.015	0.096	84.450	1.010 ± 0.006	$0.994^{+0.002}_{-0.002}$
0.015	0.150	50.000	0.977 ± 0.016	$0.994^{+0.002}_{-0.002}$
0.015	0.096	84.410	0.995 ± 0.006	$0.994^{+0.002}_{-0.002}$
0.017	0.102	84.090	0.994 ± 0.006	$0.994^{+0.002}_{-0.002}$
0.018	0.200	40.000	0.987 ± 0.004	$0.994^{+0.002}_{-0.002}$
0.018	0.149	55.000	1.000 ± 0.006	$0.993^{+0.002}_{-0.002}$
0.018	0.150	55.000	0.977 ± 0.016	$0.993^{+0.002}_{-0.002}$

Q^2 [GeV^2]	E [GeV]	θ [^{o}]	$\left(\frac{d\sigma}{d\Omega}\right)_{\rm exp} / \left(\frac{d\sigma}{d\Omega}\right)_{\rm dipole}$	$\left(\frac{d\sigma}{d\Omega}\right)_{\rm SC} / \left(\frac{d\sigma}{d\Omega}\right)_{\rm dipole}$
0.018	0.180	45.000	0.970 ± 0.016	$0.994^{+0.002}_{-0.002}$
0.019	0.143	60.000	0.963 ± 0.028	$0.993^{+0.002}_{-0.002}$
0.019	0.109	83.730	0.987 ± 0.008	$0.993^{+0.002}_{-0.002}$
0.021	0.090	115.330	0.988 ± 0.018	$0.991^{+0.002}_{-0.002}$
0.021	0.149	60.000	0.985 ± 0.006	$0.992^{+0.002}_{-0.002}$
0.021	0.150	60.000	0.980 ± 0.016	$0.992^{+0.002}_{-0.002}$
0.022	0.180	50.000	0.980 ± 0.016	$0.992^{+0.002}_{-0.002}$
0.022	0.200	45.000	0.982 ± 0.004	$0.992^{+0.002}_{-0.002}$
0.022	0.200	45.000	0.972 ± 0.017	$0.992^{+0.002}_{-0.002}$
0.023	0.159	60.000	0.958 ± 0.030	$0.991^{+0.003}_{-0.003}$
0.023	0.206	45.000	1.006 ± 0.026	$0.992^{+0.002}_{-0.002}$
0.023	0.086	150.000	0.943 ± 0.028	$0.986^{+0.002}_{-0.002}$
0.024	0.149	65.000	0.991 ± 0.006	$0.991^{+0.003}_{-0.003}$
0.024	0.150	65.000	0.987 ± 0.016	$0.991^{+0.003}_{-0.003}$
0.026	0.180	55.000	0.965 ± 0.015	$0.991^{+0.003}_{-0.003}$
0.026	0.119	93.230	0.984 ± 0.008	$0.990^{+0.003}_{-0.003}$
0.026	0.200	50.000	0.988 ± 0.006	$0.991^{+0.003}_{-0.003}$
0.026	0.200	50.000	0.959 ± 0.018	$0.991^{+0.003}_{-0.003}$
0.027	0.149	70.000	0.982 ± 0.006	$0.990^{+0.003}_{-0.003}$
0.027	0.150	70.000	0.965 ± 0.017	$0.990^{+0.003}_{-0.003}$
0.027	0.250	40.000	0.971 ± 0.018	$0.991^{+0.003}_{-0.003}$
0.029	0.229	45.000	0.955 ± 0.017	$0.990^{+0.003}_{-0.003}$
0.030	0.180	60.000	0.969 ± 0.015	$0.990^{+0.003}_{-0.003}$
0.030	0.150	75.000	0.956 ± 0.017	$0.989^{+0.003}_{-0.003}$
0.030	0.298	35.000	0.958 ± 0.016	$0.990^{+0.003}_{-0.003}$
0.031	0.129	92.640	0.991 ± 0.008	$0.988^{+0.003}_{-0.003}$
0.031	0.200	55.000	0.977 ± 0.007	$0.989^{+0.003}_{-0.003}$
0.033	0.150	80.000	0.980 ± 0.016	$0.988^{+0.003}_{-0.003}$
0.033	0.275	40.000	0.963 ± 0.017	$0.989^{+0.003}_{-0.003}$
0.034	0.180	65.000	0.963 ± 0.015	$0.988^{+0.003}_{-0.003}$
0.034	0.250	45.000	0.966 ± 0.017	$0.989^{+0.003}_{-0.004}$
0.034	0.229	50.000	0.957 ± 0.017	$0.988^{+0.004}_{-0.004}$
0.035	0.197	60.000	0.962 ± 0.031	$0.988^{+0.003}_{-0.004}$
0.036	0.200	60.000	0.986 ± 0.008	$0.988^{+0.004}_{-0.004}$
0.036	0.200	60.000	0.960 ± 0.017	$0.988^{+0.004}_{-0.004}$
0.038	0.180	70.000	0.966 ± 0.017	$0.987^{+0.004}_{-0.004}$
0.039	0.150	90.000	0.975 ± 0.016	$0.986^{+0.004}_{-0.004}$
0.039	0.298	40.000	0.956 ± 0.017	$0.987^{+0.004}_{-0.004}$

Q^2 [GeV^2]	E [GeV]	θ [^{o}]	$\left(\frac{d\sigma}{d\Omega}\right)_{\rm exp}$ / $\left(\frac{d\sigma}{d\Omega}\right)_{\rm dipole}$	$\left(\frac{d\sigma}{d\Omega}\right)_{\rm SC}$ / $\left(\frac{d\sigma}{d\Omega}\right)_{\rm dipole}$
0.039	0.113	150.000	0.989 ± 0.029	$0.980^{+0.003}_{-0.003}$
0.039	0.208	60.000	0.966 ± 0.029	$0.987^{+0.004}_{-0.004}$
0.039	0.269	45.000	0.972 ± 0.025	$0.987^{+0.004}_{-0.004}$
0.040	0.229	55.000	0.936 ± 0.017	$0.987^{+0.004}_{-0.004}$
0.041	0.139	104.000	0.976 ± 0.029	$0.984^{+0.004}_{-0.004}$
0.041	0.250	50.000	0.955 ± 0.019	$0.987^{+0.004}_{-0.004}$
0.041	0.275	45.000	0.949 ± 0.017	$0.987^{+0.004}_{-0.004}$
0.042	0.180	75.000	0.965 ± 0.017	$0.985^{+0.004}_{-0.004}$
0.044	0.150	100.000	0.976 ± 0.016	$0.983^{+0.004}_{-0.004}$
0.046	0.200	70.000	0.955 ± 0.017	$0.985^{+0.004}_{-0.004}$
0.046	0.180	80.000	0.963 ± 0.019	$0.984^{+0.004}_{-0.004}$
0.047	0.229	60.000	0.944 ± 0.016	$0.985^{+0.005}_{-0.005}$
0.048	0.250	55.000	0.952 ± 0.019	$0.985^{+0.005}_{-0.005}$
0.048	0.298	45.000	0.951 ± 0.016	$0.985^{+0.005}_{-0.005}$
0.049	0.275	50.000	0.954 ± 0.016	$0.984^{+0.005}_{-0.005}$
0.050	0.150	110.000	0.968 ± 0.016	$0.981^{+0.004}_{-0.004}$
0.054	0.150	120.000	0.982 ± 0.016	$0.978^{+0.005}_{-0.005}$
0.054	0.180	90.000	0.961 ± 0.018	$0.981^{+0.005}_{-0.005}$
0.055	0.250	60.000	0.956 ± 0.016	$0.983^{+0.005}_{-0.005}$
0.056	0.200	80.000	0.954 ± 0.019	$0.981^{+0.005}_{-0.005}$
0.057	0.298	50.000	0.949 ± 0.017	$0.982^{+0.006}_{-0.006}$
0.057	0.275	55.000	0.949 ± 0.016	$0.982^{+0.006}_{-0.006}$
0.058	0.180	95.000	0.960 ± 0.018	$0.979^{+0.005}_{-0.005}$
0.058	0.150	130.000	0.982 ± 0.016	$0.975^{+0.005}_{-0.005}$
0.059	0.229	70.000	0.952 ± 0.016	$0.981^{+0.006}_{-0.006}$
0.061	0.166	111.600	1.016 ± 0.031	$0.977^{+0.005}_{-0.005}$
0.062	0.161	120.000	1.048 ± 0.033	$0.975^{+0.005}_{-0.005}$
0.062	0.180	100.000	0.960 ± 0.018	$0.978^{+0.005}_{-0.006}$
0.062	0.152	135.000	1.017 ± 0.031	$0.973^{+0.005}_{-0.005}$
0.062	0.250	65.000	0.966 ± 0.019	$0.981^{+0.006}_{-0.006}$
0.063	0.194	90.000	1.007 ± 0.027	$0.979^{+0.006}_{-0.006}$
0.063	0.268	60.000	1.018 ± 0.027	$0.981^{+0.006}_{-0.006}$
0.066	0.200	90.000	0.960 ± 0.019	$0.978^{+0.006}_{-0.006}$
0.066	0.180	105.000	0.962 ± 0.018	$0.976^{+0.006}_{-0.006}$
0.066	0.229	75.000	0.954 ± 0.016	$0.979^{+0.006}_{-0.006}$
0.066	0.275	60.000	0.943 ± 0.017	$0.980^{+0.006}_{-0.006}$
0.067	0.298	55.000	0.941 ± 0.017	$0.980^{+0.006}_{-0.006}$
0.069	0.180	110.000	0.942 ± 0.018	$0.974^{+0.006}_{-0.006}$

Q^2 [GeV^2]	E [GeV]	θ [^{o}]	$\left(\frac{d\sigma}{d\Omega}\right)_{\rm exp} / \left(\frac{d\sigma}{d\Omega}\right)_{\rm dipole}$	$\left(\frac{d\sigma}{d\Omega}\right)_{\rm SC} / \left(\frac{d\sigma}{d\Omega}\right)_{\rm dipole}$
0.070	0.250	70.000	0.954 ± 0.017	$0.978^{+0.006}_{-0.007}$
0.072	0.229	80.000	0.956 ± 0.018	$0.977^{+0.006}_{-0.007}$
0.072	0.180	115.000	0.952 ± 0.018	$0.973^{+0.006}_{-0.006}$
0.075	0.200	100.000	0.965 ± 0.018	$0.974^{+0.006}_{-0.006}$
0.076	0.180	120.000	0.948 ± 0.018	$0.971^{+0.006}_{-0.006}$
0.077	0.298	60.000	0.939 ± 0.017	$0.977^{+0.007}_{-0.007}$
0.077	0.250	75.000	0.963 ± 0.018	$0.977^{+0.007}_{-0.007}$
0.078	0.230	84.000	0.946 ± 0.028	$0.976^{+0.007}_{-0.007}$
0.078	0.167	150.000	0.964 ± 0.029	$0.965^{+0.006}_{-0.007}$
0.079	0.200	105.000	0.951 ± 0.019	$0.972^{+0.006}_{-0.007}$
0.079	0.390	45.000	0.978 ± 0.029	$0.978^{+0.008}_{-0.008}$
0.081	0.180	130.000	0.953 ± 0.016	$0.968^{+0.006}_{-0.006}$
0.083	0.200	110.000	0.945 ± 0.017	$0.970^{+0.007}_{-0.007}$
0.084	0.275	70.000	0.950 ± 0.016	$0.975^{+0.008}_{-0.008}$
0.084	0.229	90.000	0.957 ± 0.018	$0.973^{+0.007}_{-0.007}$
0.084	0.250	80.000	0.929 ± 0.019	$0.974^{+0.007}_{-0.008}$
0.086	0.180	140.000	0.970 ± 0.020	$0.965^{+0.007}_{-0.007}$
0.086	0.316	60.000	0.986 ± 0.027	$0.976^{+0.008}_{-0.008}$
0.087	0.298	65.000	0.940 ± 0.017	$0.975^{+0.008}_{-0.008}$
0.087	0.200	115.000	0.943 ± 0.017	$0.969^{+0.007}_{-0.007}$
0.091	0.200	120.000	0.955 ± 0.017	$0.967^{+0.007}_{-0.007}$
0.097	0.298	70.000	0.940 ± 0.016	$0.972^{+0.009}_{-0.009}$
0.097	0.200	130.000	0.948 ± 0.016	$0.963^{+0.007}_{-0.007}$
0.098	0.250	90.000	0.944 ± 0.019	$0.970^{+0.008}_{-0.009}$
0.101	0.275	80.000	0.937 ± 0.016	$0.971^{+0.009}_{-0.009}$
0.102	0.200	140.000	0.939 ± 0.017	$0.960^{+0.008}_{-0.008}$
0.106	0.229	110.000	0.949 ± 0.019	$0.966^{+0.008}_{-0.008}$
0.111	0.229	115.000	0.951 ± 0.018	$0.964^{+0.009}_{-0.009}$
0.111	0.250	100.000	0.937 ± 0.021	$0.966^{+0.009}_{-0.009}$
0.115	0.229	120.000	0.949 ± 0.018	$0.962^{+0.009}_{-0.009}$
0.116	0.210	150.000	0.972 ± 0.031	$0.955^{+0.009}_{-0.010}$
0.117	0.249	105.000	0.977 ± 0.029	$0.965^{+0.009}_{-0.009}$
0.117	0.275	90.000	0.943 ± 0.016	$0.967^{+0.010}_{-0.010}$
0.120	0.605	35.200	0.909 ± 0.048	$0.971^{+0.011}_{-0.011}$
0.123	0.229	130.000	0.952 ± 0.019	$0.959^{+0.009}_{-0.010}$
0.123	0.250	110.000	0.941 ± 0.021	$0.963^{+0.010}_{-0.010}$
0.129	0.229	140.000	0.968 ± 0.018	$0.956^{+0.010}_{-0.010}$
0.132	0.275	100.000	0.934 ± 0.016	$0.963^{+0.010}_{-0.011}$

Q^2 [GeV^2]	E [GeV]	θ [^{o}]	$\left(\frac{d\sigma}{d\Omega}\right)_{\rm exp}$ / $\left(\frac{d\sigma}{d\Omega}\right)_{\rm dipole}$	$\left(\frac{d\sigma}{d\Omega}\right)_{\rm SC}$ / $\left(\frac{d\sigma}{d\Omega}\right)_{\rm dipole}$
0.134	0.250	120.000	0.932 ± 0.020	$0.959^{+0.010}_{-0.010}$
0.142	0.250	130.000	0.939 ± 0.018	$0.956^{+0.011}_{-0.011}$
0.146	0.275	110.000	0.939 ± 0.016	$0.959^{+0.011}_{-0.011}$
0.148	0.242	150.000	0.928 ± 0.035	$0.951^{+0.012}_{-0.012}$
0.149	0.545	45.000	0.961 ± 0.031	$0.967^{+0.013}_{-0.014}$
0.150	0.250	140.000	0.968 ± 0.019	$0.953^{+0.011}_{-0.012}$
0.156	0.368	75.000	0.955 ± 0.030	$0.963^{+0.013}_{-0.013}$
0.156	0.259	135.000	0.895 ± 0.028	$0.953^{+0.012}_{-0.012}$
0.156	0.559	45.000	0.999 ± 0.031	$0.967^{+0.014}_{-0.014}$
0.158	0.275	120.000	0.948 ± 0.016	$0.955^{+0.012}_{-0.012}$
0.168	0.275	130.000	0.953 ± 0.016	$0.952^{+0.013}_{-0.013}$
0.176	0.275	140.000	0.956 ± 0.016	$0.949^{+0.013}_{-0.014}$
0.179	0.603	45.000	0.948 ± 0.029	$0.964^{+0.016}_{-0.016}$
0.179	0.351	90.000	0.918 ± 0.029	$0.959^{+0.014}_{-0.014}$
0.179	0.474	60.000	0.910 ± 0.029	$0.963^{+0.015}_{-0.016}$
0.179	0.297	120.000	0.906 ± 0.028	$0.952^{+0.013}_{-0.014}$
0.179	0.399	75.000	0.930 ± 0.029	$0.960^{+0.014}_{-0.015}$
0.179	0.282	135.000	0.945 ± 0.029	$0.950^{+0.013}_{-0.014}$
0.179	0.275	145.000	0.916 ± 0.029	$0.948^{+0.014}_{-0.015}$
0.183	0.275	150.000	0.952 ± 0.016	$0.947^{+0.014}_{-0.015}$
0.194	0.296	135.000	0.985 ± 0.030	$0.948^{+0.014}_{-0.015}$
0.195	0.418	75.000	1.020 ± 0.031	$0.960^{+0.015}_{-0.016}$
0.195	0.690	40.600	0.941 ± 0.029	$0.964^{+0.017}_{-0.017}$
0.211	0.311	135.000	0.942 ± 0.034	$0.947^{+0.016}_{-0.017}$
0.211	0.438	75.000	0.960 ± 0.033	$0.959^{+0.017}_{-0.017}$
0.212	0.304	145.000	0.992 ± 0.036	$0.945^{+0.016}_{-0.017}$
0.212	0.328	120.000	0.994 ± 0.035	$0.951^{+0.015}_{-0.016}$
0.233	0.690	45.500	1.020 ± 0.031	$0.962^{+0.020}_{-0.020}$
0.233	0.331	135.000	0.910 ± 0.029	$0.947^{+0.017}_{-0.018}$
0.234	0.464	75.000	0.938 ± 0.029	$0.958^{+0.018}_{-0.019}$
0.234	0.550	60.000	0.955 ± 0.030	$0.960^{+0.019}_{-0.020}$
0.272	0.364	135.000	0.884 ± 0.028	$0.947^{+0.020}_{-0.021}$
0.273	0.434	95.000	0.854 ± 0.027	$0.954^{+0.020}_{-0.020}$
0.273	0.449	90.000	0.988 ± 0.036	$0.955^{+0.020}_{-0.020}$
0.273	0.600	60.000	0.952 ± 0.029	$0.959^{+0.021}_{-0.022}$
0.273	0.356	145.000	0.927 ± 0.029	$0.946^{+0.021}_{-0.022}$
0.273	0.508	75.000	0.954 ± 0.030	$0.957^{+0.021}_{-0.021}$
0.291	0.380	135.000	0.908 ± 0.029	$0.947^{+0.021}_{-0.023}$

Q^2 [GeV^2]	E [GeV]	θ [^{o}]	$\left(\frac{d\sigma}{d\Omega}\right)_{\rm exp} / \left(\frac{d\sigma}{d\Omega}\right)_{\rm dipole}$	$\left(\frac{d\sigma}{d\Omega}\right)_{\rm SC} / \left(\frac{d\sigma}{d\Omega}\right)_{\rm dipole}$
0.292	0.399	120.000	0.879 ± 0.028	$0.949^{+0.021}_{-0.022}$
0.292	0.528	75.000	0.936 ± 0.029	$0.957^{+0.022}_{-0.023}$
0.292	0.624	60.000	0.947 ± 0.029	$0.959^{+0.023}_{-0.024}$
0.292	0.468	90.000	0.922 ± 0.029	$0.955^{+0.022}_{-0.022}$
0.311	0.396	135.000	0.901 ± 0.028	$0.947^{+0.023}_{-0.024}$
0.311	0.647	60.000	0.965 ± 0.030	$0.959^{+0.024}_{-0.025}$
0.311	0.647	60.000	0.902 ± 0.028	$0.959^{+0.024}_{-0.025}$
0.311	0.387	145.000	0.957 ± 0.030	$0.947^{+0.023}_{-0.025}$
0.311	0.690	55.300	0.894 ± 0.028	$0.960^{+0.024}_{-0.025}$
0.312	0.549	75.000	0.925 ± 0.029	$0.957^{+0.023}_{-0.024}$
0.312	0.416	120.000	0.973 ± 0.036	$0.950^{+0.022}_{-0.024}$
0.350	0.692	60.000	0.912 ± 0.029	$0.960^{+0.026}_{-0.028}$
0.350	0.588	75.000	0.932 ± 0.029	$0.958^{+0.026}_{-0.026}$
0.350	0.427	135.000	0.942 ± 0.029	$0.950^{+0.026}_{-0.027}$
0.388	1.249	31.700	0.916 ± 0.044	$0.964^{+0.031}_{-0.032}$
0.389	0.736	60.000	0.953 ± 0.029	$0.961^{+0.029}_{-0.030}$
0.389	0.457	135.000	0.927 ± 0.029	$0.953^{+0.028}_{-0.030}$
0.389	0.557	90.000	0.969 ± 0.036	$0.958^{+0.028}_{-0.028}$
0.389	0.557	90.000	0.958 ± 0.030	$0.958^{+0.028}_{-0.028}$
0.389	1.009	40.600	1.010 ± 0.137	$0.963^{+0.030}_{-0.032}$
0.389	1.009	40.600	0.967 ± 0.133	$0.963^{+0.030}_{-0.032}$
0.389	0.696	64.700	0.940 ± 0.043	$0.960^{+0.029}_{-0.030}$
0.389	0.447	145.000	0.941 ± 0.029	$0.952^{+0.029}_{-0.030}$
0.389	0.848	50.100	0.923 ± 0.044	$0.962^{+0.030}_{-0.031}$
0.389	0.556	90.300	0.956 ± 0.044	$0.958^{+0.028}_{-0.028}$
0.390	0.627	75.000	0.941 ± 0.029	$0.960^{+0.028}_{-0.029}$
0.390	0.479	120.000	0.926 ± 0.029	$0.954^{+0.027}_{-0.029}$
0.390	1.231	32.300	0.939 ± 0.044	$0.964^{+0.031}_{-0.032}$
0.390	0.900	46.600	1.010 ± 0.031	$0.962^{+0.030}_{-0.031}$
0.390	1.142	35.200	0.944 ± 0.044	$0.964^{+0.031}_{-0.032}$
0.397	0.745	60.000	0.933 ± 0.031	$0.962^{+0.030}_{-0.031}$
0.397	0.485	120.000	0.957 ± 0.040	$0.954^{+0.028}_{-0.030}$
0.428	0.486	135.000	0.959 ± 0.030	$0.955^{+0.031}_{-0.033}$
0.429	0.664	75.000	0.951 ± 0.029	$0.962^{+0.031}_{-0.031}$
0.429	0.950	46.600	1.010 ± 0.031	$0.964^{+0.032}_{-0.034}$
0.467	0.900	53.000	0.974 ± 0.030	$0.965^{+0.034}_{-0.036}$
0.467	0.950	49.500	0.993 ± 0.030	$0.966^{+0.034}_{-0.036}$
0.467	0.504	145.000	0.969 ± 0.030	$0.958^{+0.034}_{-0.036}$

Q^2 [GeV^2]	E [GeV]	θ [^{o}]	$\left(\frac{d\sigma}{d\Omega}\right)_{\rm exp}$ / $\left(\frac{d\sigma}{d\Omega}\right)_{\rm dipole}$	$\left(\frac{d\sigma}{d\Omega}\right)_{\rm SC}$ / $\left(\frac{d\sigma}{d\Omega}\right)_{\rm dipole}$
0.468	0.515	135.000	0.955 ± 0.030	$0.959^{+0.033}_{-0.036}$
0.468	0.700	75.000	0.947 ± 0.029	$0.964^{+0.033}_{-0.034}$
0.487	0.717	75.000	0.923 ± 0.029	$0.965^{+0.034}_{-0.035}$
0.506	0.950	52.500	1.010 ± 0.031	$0.968^{+0.037}_{-0.038}$
0.506	0.543	135.000	0.942 ± 0.029	$0.963^{+0.036}_{-0.038}$
0.507	0.735	75.000	0.918 ± 0.029	$0.967^{+0.036}_{-0.036}$
0.545	0.570	135.000	0.958 ± 0.030	$0.967^{+0.038}_{-0.041}$
0.545	0.950	55.600	1.050 ± 0.032	$0.970^{+0.039}_{-0.040}$
0.545	0.900	59.800	0.977 ± 0.030	$0.970^{+0.039}_{-0.040}$
0.545	0.769	75.000	0.923 ± 0.029	$0.969^{+0.038}_{-0.038}$
0.546	0.559	145.000	1.020 ± 0.031	$0.967^{+0.039}_{-0.041}$
0.579	1.171	44.500	0.943 ± 0.044	$0.973^{+0.041}_{-0.044}$
0.583	1.629	30.200	0.989 ± 0.045	$0.973^{+0.043}_{-0.045}$
0.583	0.597	135.000	0.988 ± 0.030	$0.971^{+0.040}_{-0.044}$
0.584	0.886	64.700	0.959 ± 0.044	$0.972^{+0.041}_{-0.042}$
0.584	0.647	110.000	0.959 ± 0.046	$0.972^{+0.039}_{-0.042}$
0.584	0.802	75.000	0.928 ± 0.029	$0.972^{+0.040}_{-0.040}$
0.584	0.718	90.000	1.020 ± 0.040	$0.972^{+0.039}_{-0.041}$
0.584	0.718	90.000	1.040 ± 0.048	$0.972^{+0.039}_{-0.041}$
0.584	1.522	32.700	0.953 ± 0.044	$0.973^{+0.043}_{-0.045}$
0.584	0.645	111.000	0.981 ± 0.046	$0.972^{+0.039}_{-0.043}$
0.585	0.717	90.300	0.973 ± 0.044	$0.972^{+0.039}_{-0.041}$
0.585	1.072	50.100	0.951 ± 0.044	$0.973^{+0.041}_{-0.043}$
0.585	0.950	58.800	1.050 ± 0.032	$0.973^{+0.041}_{-0.042}$
0.585	0.718	90.100	0.972 ± 0.044	$0.972^{+0.039}_{-0.041}$
0.585	0.892	64.200	0.971 ± 0.044	$0.973^{+0.041}_{-0.042}$
0.585	1.042	52.000	0.977 ± 0.045	$0.973^{+0.041}_{-0.043}$
0.585	1.540	32.300	0.968 ± 0.044	$0.973^{+0.043}_{-0.045}$
0.586	1.431	35.200	0.975 ± 0.044	$0.973^{+0.043}_{-0.045}$
0.621	1.520	34.100	0.927 ± 0.085	$0.975^{+0.045}_{-0.047}$
0.623	0.624	135.000	0.974 ± 0.030	$0.975^{+0.043}_{-0.046}$
0.623	0.835	75.000	0.919 ± 0.029	$0.976^{+0.042}_{-0.043}$
0.623	1.652	31.000	1.040 ± 0.109	$0.976^{+0.045}_{-0.047}$
0.623	1.652	31.000	1.020 ± 0.107	$0.976^{+0.045}_{-0.047}$
0.623	0.900	67.000	0.980 ± 0.030	$0.975^{+0.043}_{-0.044}$
0.623	0.950	62.000	0.979 ± 0.030	$0.976^{+0.043}_{-0.044}$
0.623	0.802	80.000	0.996 ± 0.030	$0.975^{+0.042}_{-0.043}$
0.623	0.612	145.000	0.990 ± 0.030	$0.975^{+0.043}_{-0.047}$

Q^2 [GeV^2]	E [GeV]	θ [^{o}]	$\left(\frac{d\sigma}{d\Omega}\right)_{\rm exp} / \left(\frac{d\sigma}{d\Omega}\right)_{\rm dipole}$	$\left(\frac{d\sigma}{d\Omega}\right)_{\rm SC} / \left(\frac{d\sigma}{d\Omega}\right)_{\rm dipole}$
0.661	0.867	75.000	0.973 ± 0.030	$0.979^{+0.045}_{-0.045}$
0.662	0.950	65.400	1.010 ± 0.031	$0.979^{+0.045}_{-0.046}$
0.662	0.651	135.000	1.050 ± 0.032	$0.980^{+0.045}_{-0.049}$
0.664	1.190	48.200	1.040 ± 0.072	$0.978^{+0.046}_{-0.048}$
0.665	1.680	31.700	0.981 ± 0.090	$0.978^{+0.047}_{-0.050}$
0.670	0.805	86.000	0.952 ± 0.033	$0.980^{+0.044}_{-0.046}$
0.681	0.883	75.000	1.010 ± 0.031	$0.980^{+0.046}_{-0.046}$
0.701	0.899	75.000	1.020 ± 0.031	$0.982^{+0.047}_{-0.047}$
0.701	0.864	80.000	0.970 ± 0.030	$0.982^{+0.046}_{-0.048}$
0.701	0.950	68.900	1.060 ± 0.032	$0.982^{+0.047}_{-0.048}$
0.701	0.677	135.000	0.977 ± 0.030	$0.984^{+0.047}_{-0.052}$
0.701	0.664	145.000	0.991 ± 0.030	$0.984^{+0.048}_{-0.052}$
0.739	0.930	75.000	1.110 ± 0.033	$0.986^{+0.049}_{-0.050}$
0.740	0.950	72.600	1.030 ± 0.031	$0.985^{+0.049}_{-0.050}$
0.740	0.703	135.000	1.040 ± 0.031	$0.989^{+0.050}_{-0.054}$
0.766	1.104	59.900	1.030 ± 0.041	$0.987^{+0.051}_{-0.052}$
0.778	0.784	110.000	1.010 ± 0.045	$0.992^{+0.050}_{-0.055}$
0.778	0.961	75.000	1.080 ± 0.032	$0.989^{+0.051}_{-0.052}$
0.778	0.728	135.000	1.180 ± 0.035	$0.993^{+0.052}_{-0.056}$
0.779	0.865	90.000	1.020 ± 0.041	$0.990^{+0.050}_{-0.053}$
0.779	0.900	83.800	0.933 ± 0.029	$0.990^{+0.050}_{-0.053}$
0.779	0.950	76.500	1.110 ± 0.033	$0.989^{+0.051}_{-0.052}$
0.779	1.789	32.700	0.981 ± 0.045	$0.985^{+0.053}_{-0.056}$
0.779	0.925	80.000	0.937 ± 0.029	$0.989^{+0.051}_{-0.053}$
0.779	0.865	90.100	1.010 ± 0.046	$0.990^{+0.050}_{-0.053}$
0.779	0.715	145.000	1.020 ± 0.031	$0.993^{+0.052}_{-0.057}$
0.780	1.064	64.200	0.964 ± 0.046	$0.988^{+0.051}_{-0.052}$
0.780	1.392	44.500	1.000 ± 0.045	$0.986^{+0.052}_{-0.055}$
0.780	1.683	35.200	0.985 ± 0.050	$0.986^{+0.053}_{-0.056}$
0.784	1.190	55.000	1.040 ± 0.111	$0.988^{+0.052}_{-0.054}$
0.852	1.250	55.100	1.060 ± 0.090	$0.993^{+0.056}_{-0.057}$
0.856	0.764	145.000	1.160 ± 0.034	$1.002^{+0.057}_{-0.062}$
0.857	1.022	75.000	1.160 ± 0.034	$0.996^{+0.055}_{-0.057}$
0.857	1.975	31.000	1.110 ± 0.115	$0.990^{+0.057}_{-0.060}$
0.857	0.779	135.000	1.210 ± 0.035	$1.002^{+0.056}_{-0.061}$
0.857	0.950	85.100	1.010 ± 0.031	$0.997^{+0.054}_{-0.058}$
0.973	1.003	90.100	1.040 ± 0.048	$1.008^{+0.060}_{-0.065}$
0.973	0.915	110.000	1.000 ± 0.053	$1.011^{+0.061}_{-0.067}$

Q^2 [GeV^2]	E [GeV]	θ [^{o}]	$\left(\frac{d\sigma}{d\Omega}\right)_{\rm exp}$ / $\left(\frac{d\sigma}{d\Omega}\right)_{\rm dipole}$	$\left(\frac{d\sigma}{d\Omega}\right)_{\rm SC}$ / $\left(\frac{d\sigma}{d\Omega}\right)_{\rm dipole}$
0.973	1.718	40.200	1.060 ± 0.046	$0.999^{+0.062}_{-0.065}$
0.974	1.224	64.200	1.030 ± 0.046	$1.004^{+0.061}_{-0.062}$
0.975	1.913	35.200	1.020 ± 0.045	$0.999^{+0.063}_{-0.066}$
1.002	1.048	86.000	1.050 ± 0.037	$1.010^{+0.061}_{-0.066}$
1.012	0.862	145.000	1.100 ± 0.033	$1.019^{+0.065}_{-0.071}$
1.090	0.910	145.000	1.060 ± 0.032	$1.027^{+0.069}_{-0.075}$
1.120	1.104	90.000	1.040 ± 0.053	$1.021^{+0.067}_{-0.073}$
1.167	1.135	90.100	1.050 ± 0.048	$1.025^{+0.069}_{-0.075}$
1.167	1.040	110.000	1.090 ± 0.068	$1.030^{+0.071}_{-0.077}$
1.167	1.162	86.000	1.050 ± 0.034	$1.024^{+0.069}_{-0.075}$
1.168	1.910	40.300	1.070 ± 0.059	$1.012^{+0.071}_{-0.074}$
1.168	1.375	64.200	1.080 ± 0.047	$1.019^{+0.070}_{-0.072}$
1.169	0.958	145.000	1.030 ± 0.031	$1.034^{+0.073}_{-0.080}$
1.169	2.358	31.000	1.160 ± 0.123	$1.009^{+0.071}_{-0.075}$
1.169	2.358	31.000	1.170 ± 0.122	$1.009^{+0.071}_{-0.075}$
1.169	2.358	31.000	1.070 ± 0.116	$1.009^{+0.071}_{-0.075}$
1.169	1.137	90.000	1.260 ± 0.144	$1.026^{+0.069}_{-0.076}$
1.169	1.137	90.000	1.140 ± 0.136	$1.026^{+0.069}_{-0.076}$
1.169	1.137	90.000	1.070 ± 0.036	$1.026^{+0.069}_{-0.076}$
1.362	1.512	64.700	1.090 ± 0.055	$1.032^{+0.078}_{-0.082}$
1.363	1.263	90.300	1.070 ± 0.053	$1.041^{+0.078}_{-0.085}$
1.364	1.160	111.000	1.060 ± 0.057	$1.046^{+0.080}_{-0.088}$
1.364	1.790	50.100	1.030 ± 0.049	$1.027^{+0.078}_{-0.081}$
1.501	1.383	86.000	1.070 ± 0.040	$1.049^{+0.083}_{-0.092}$
1.514	1.700	59.900	0.914 ± 0.101	$1.039^{+0.084}_{-0.088}$
1.516	1.870	51.800	1.100 ± 0.103	$1.036^{+0.084}_{-0.087}$
1.517	2.250	40.000	0.954 ± 0.100	$1.031^{+0.084}_{-0.088}$
1.518	1.520	72.700	1.090 ± 0.094	$1.045^{+0.083}_{-0.090}$
1.518	1.520	72.700	1.160 ± 0.103	$1.045^{+0.083}_{-0.090}$
1.525	2.710	31.600	0.980 ± 0.088	$1.028^{+0.085}_{-0.089}$
1.525	2.710	31.600	1.030 ± 0.141	$1.028^{+0.085}_{-0.089}$
1.525	1.710	59.800	1.060 ± 0.092	$1.040^{+0.084}_{-0.089}$
1.557	1.282	110.000	1.110 ± 0.055	$1.060^{+0.089}_{-0.097}$
1.557	1.389	90.100	1.070 ± 0.060	$1.054^{+0.086}_{-0.095}$
1.558	1.661	64.200	1.140 ± 0.058	$1.044^{+0.085}_{-0.091}$
1.751	1.512	90.000	1.090 ± 0.041	$1.065^{+0.094}_{-0.103}$
1.752	1.597	80.000	1.160 ± 0.064	$1.061^{+0.092}_{-0.102}$
1.752	1.789	64.700	1.100 ± 0.053	$1.054^{+0.091}_{-0.099}$

Q^2 [GeV^2]	E [GeV]	θ [^{o}]	$\left(\frac{d\sigma}{d\Omega}\right)_{\rm exp} / \left(\frac{d\sigma}{d\Omega}\right)_{\rm dipole}$	$\left(\frac{d\sigma}{d\Omega}\right)_{\rm SC} / \left(\frac{d\sigma}{d\Omega}\right)_{\rm dipole}$
1.752	1.513	90.000	1.160 ± 0.161	$1.065^{+0.094}_{-0.103}$
1.752	1.513	90.000	1.270 ± 0.183	$1.065^{+0.094}_{-0.103}$
1.753	1.544	86.000	1.090 ± 0.034	$1.064^{+0.093}_{-0.103}$
1.753	1.511	90.300	1.150 ± 0.061	$1.065^{+0.094}_{-0.103}$
1.753	2.988	31.000	1.300 ± 0.136	$1.037^{+0.093}_{-0.097}$
1.753	2.988	31.000	1.370 ± 0.141	$1.037^{+0.093}_{-0.097}$
1.753	2.988	31.000	1.190 ± 0.136	$1.037^{+0.093}_{-0.097}$
1.753	2.988	31.000	1.180 ± 0.124	$1.037^{+0.093}_{-0.097}$
1.754	1.397	111.000	1.090 ± 0.077	$1.072^{+0.096}_{-0.106}$
1.946	1.632	90.100	1.060 ± 0.069	$1.075^{+0.101}_{-0.111}$
1.964	1.644	90.000	1.130 ± 0.250	$1.075^{+0.101}_{-0.112}$
1.995	2.998	34.100	1.080 ± 0.044	$1.047^{+0.100}_{-0.104}$
2.001	1.699	86.000	1.090 ± 0.037	$1.075^{+0.102}_{-0.113}$
2.001	1.699	86.000	1.100 ± 0.034	$1.075^{+0.102}_{-0.113}$
2.330	1.670	129.000	1.230 ± 0.208	$1.100^{+0.117}_{-0.129}$
2.331	1.901	86.000	1.140 ± 0.042	$1.087^{+0.112}_{-0.125}$
2.331	2.630	47.100	1.110 ± 0.139	$1.065^{+0.108}_{-0.117}$
2.334	2.220	62.500	0.901 ± 0.120	$1.074^{+0.108}_{-0.120}$
2.335	2.670	46.100	1.040 ± 0.095	$1.064^{+0.108}_{-0.117}$
2.336	1.904	86.000	1.080 ± 0.035	$1.087^{+0.112}_{-0.125}$
2.337	1.870	90.000	0.989 ± 0.128	$1.089^{+0.113}_{-0.125}$
2.338	1.880	88.900	1.470 ± 0.139	$1.088^{+0.113}_{-0.125}$
2.341	3.460	32.100	1.050 ± 0.097	$1.055^{+0.108}_{-0.115}$
2.342	2.220	62.800	0.865 ± 0.086	$1.075^{+0.108}_{-0.121}$
2.497	3.294	36.200	1.060 ± 0.044	$1.061^{+0.112}_{-0.121}$
2.498	2.998	41.400	1.060 ± 0.044	$1.064^{+0.112}_{-0.122}$
2.499	3.296	36.200	1.050 ± 0.045	$1.061^{+0.112}_{-0.121}$
2.922	2.216	90.000	1.550 ± 0.261	$1.099^{+0.128}_{-0.144}$
2.922	2.216	90.000	1.840 ± 0.323	$1.099^{+0.128}_{-0.144}$
2.922	4.070	31.000	1.380 ± 0.184	$1.062^{+0.120}_{-0.133}$
3.000	2.300	86.000	1.090 ± 0.047	$1.098^{+0.129}_{-0.146}$
3.000	2.300	86.000	1.100 ± 0.036	$1.098^{+0.129}_{-0.146}$
3.112	3.470	41.200	0.944 ± 0.102	$1.071^{+0.124}_{-0.141}$
3.117	4.120	32.200	1.100 ± 0.115	$1.064^{+0.124}_{-0.139}$
3.121	2.670	65.200	1.050 ± 0.134	$1.088^{+0.127}_{-0.146}$
3.743	3.996	40.000	1.040 ± 0.045	$1.069^{+0.133}_{-0.157}$
3.895	2.777	90.000	1.920 ± 0.544	$1.097^{+0.145}_{-0.172}$
3.895	2.777	90.000	1.920 ± 0.449	$1.097^{+0.145}_{-0.172}$

Q^2 [GeV^2]	E [GeV]	θ [^{o}]	$\left(\frac{d\sigma}{d\Omega}\right)_{\rm exp} / \left(\frac{d\sigma}{d\Omega}\right)_{\rm dipole}$	$\left(\frac{d\sigma}{d\Omega}\right)_{\rm SC} / \left(\frac{d\sigma}{d\Omega}\right)_{\rm dipole}$
3.895	2.777	90.000	2.010 ± 0.608	$1.097^{+0.145}_{-0.172}$
3.896	4.874	31.000	1.320 ± 0.154	$1.061^{+0.134}_{-0.158}$
3.896	4.874	31.000	1.330 ± 0.203	$1.061^{+0.134}_{-0.158}$
3.896	4.874	31.000	1.340 ± 0.241	$1.061^{+0.134}_{-0.158}$
4.142	3.870	47.300	1.020 ± 0.114	$1.071^{+0.139}_{-0.169}$
4.188	3.110	76.500	1.000 ± 0.112	$1.087^{+0.146}_{-0.177}$
4.275	3.460	61.500	1.180 ± 0.157	$1.078^{+0.144}_{-0.175}$
4.895	4.340	47.600	0.940 ± 0.106	$1.058^{+0.149}_{-0.184}$
5.879	4.960	47.500	0.975 ± 0.110	$1.033^{+0.159}_{-0.199}$
6.830	5.540	47.500	0.840 ± 0.098	$1.003^{+0.164}_{-0.209}$
7.826	6.130	47.600	0.894 ± 0.102	$0.970^{+0.167}_{-0.215}$
8.774	5.710	75.100	0.927 ± 0.283	$0.939^{+0.173}_{-0.231}$
9.560	6.130	75.700	1.040 ± 0.419	$0.910^{+0.173}_{-0.233}$

Table 8.1: Comparison of the fit to the cross section data within the SC approach to the experimental results. Here Q^2 is the invariant four-momentum transfer squared, E is the incoming electron energy, θ is the electron scattering angle, $\left(\frac{d\sigma}{d\Omega}\right)_{\rm exp} / \left(\frac{d\sigma}{d\Omega}\right)_{\rm dipole}$ is the experimental cross section data normalised to the dipole cross section, and $\left(\frac{d\sigma}{d\Omega}\right)_{\rm SC} / \left(\frac{d\sigma}{d\Omega}\right)_{\rm dipole}$ is the Coulomb-corrected cross section obtained in the cross section fit within the SC approach.

Results of the fit to cross section data within the pQCD approach

Table 8.2 gives the numerical results of the analysis of the cross section data for unpolarised elastic electron-proton scattering within the pQCD approach compared to the experimental data.

Q^2 [GeV^2]	E [GeV]	θ [^{o}]	$\left(\frac{d\sigma}{d\Omega}\right)_{\rm exp} / \left(\frac{d\sigma}{d\Omega}\right)_{\rm dipole}$	$\left(\frac{d\sigma}{d\Omega}\right)_{\rm pQCD} / \left(\frac{d\sigma}{d\Omega}\right)_{\rm dipole}$
0.006	0.149	30.000	0.996 ± 0.006	$0.997^{+0.002}_{-0.002}$
0.008	0.149	35.000	1.001 ± 0.005	$0.996^{+0.002}_{-0.002}$
0.010	0.149	40.000	0.995 ± 0.006	$0.994^{+0.003}_{-0.003}$
0.011	0.082	85.190	1.000 ± 0.010	$0.993^{+0.003}_{-0.003}$
0.012	0.082	85.180	0.995 ± 0.006	$0.993^{+0.003}_{-0.003}$

Q^2 [GeV^2]	E [GeV]	θ [^{o}]	$\left(\frac{d\sigma}{d\Omega}\right)_{\rm exp} / \left(\frac{d\sigma}{d\Omega}\right)_{\rm dipole}$	$\left(\frac{d\sigma}{d\Omega}\right)_{\rm pQCD} / \left(\frac{d\sigma}{d\Omega}\right)_{\rm dipole}$
0.012	0.111	60.000	0.980 ± 0.029	$0.994^{+0.003}_{-0.003}$
0.012	0.144	45.000	1.012 ± 0.025	$0.994^{+0.003}_{-0.003}$
0.012	0.149	45.000	0.991 ± 0.005	$0.993^{+0.003}_{-0.003}$
0.013	0.150	45.000	0.974 ± 0.016	$0.993^{+0.003}_{-0.003}$
0.013	0.090	84.780	0.996 ± 0.006	$0.992^{+0.004}_{-0.003}$
0.014	0.200	35.000	1.000 ± 0.006	$0.993^{+0.003}_{-0.003}$
0.015	0.149	50.000	0.995 ± 0.005	$0.992^{+0.004}_{-0.004}$
0.015	0.096	84.450	1.010 ± 0.006	$0.992^{+0.004}_{-0.003}$
0.015	0.150	50.000	0.977 ± 0.016	$0.992^{+0.004}_{-0.004}$
0.015	0.096	84.410	0.995 ± 0.006	$0.992^{+0.004}_{-0.004}$
0.017	0.102	84.090	0.994 ± 0.006	$0.991^{+0.004}_{-0.004}$
0.018	0.200	40.000	0.987 ± 0.004	$0.991^{+0.004}_{-0.004}$
0.018	0.149	55.000	1.000 ± 0.006	$0.991^{+0.005}_{-0.004}$
0.018	0.150	55.000	0.977 ± 0.016	$0.991^{+0.005}_{-0.004}$
0.018	0.180	45.000	0.970 ± 0.016	$0.991^{+0.005}_{-0.004}$
0.019	0.143	60.000	0.963 ± 0.028	$0.990^{+0.005}_{-0.005}$
0.019	0.109	83.730	0.987 ± 0.008	$0.990^{+0.005}_{-0.004}$
0.021	0.090	115.330	0.988 ± 0.018	$0.988^{+0.005}_{-0.004}$
0.021	0.149	60.000	0.985 ± 0.006	$0.989^{+0.005}_{-0.005}$
0.021	0.150	60.000	0.980 ± 0.016	$0.989^{+0.005}_{-0.005}$
0.022	0.180	50.000	0.980 ± 0.016	$0.989^{+0.005}_{-0.005}$
0.022	0.200	45.000	0.982 ± 0.004	$0.989^{+0.005}_{-0.005}$
0.022	0.200	45.000	0.972 ± 0.017	$0.989^{+0.005}_{-0.005}$
0.023	0.159	60.000	0.958 ± 0.030	$0.988^{+0.006}_{-0.005}$
0.023	0.206	45.000	1.006 ± 0.026	$0.989^{+0.006}_{-0.005}$
0.023	0.086	150.000	0.943 ± 0.028	$0.985^{+0.004}_{-0.004}$
0.024	0.149	65.000	0.991 ± 0.006	$0.988^{+0.006}_{-0.005}$
0.024	0.150	65.000	0.987 ± 0.016	$0.988^{+0.006}_{-0.006}$
0.026	0.180	55.000	0.965 ± 0.015	$0.987^{+0.006}_{-0.006}$
0.026	0.119	93.230	0.984 ± 0.008	$0.987^{+0.006}_{-0.006}$
0.026	0.200	50.000	0.988 ± 0.006	$0.987^{+0.006}_{-0.006}$
0.026	0.200	50.000	0.959 ± 0.018	$0.987^{+0.006}_{-0.006}$
0.027	0.149	70.000	0.982 ± 0.006	$0.986^{+0.007}_{-0.006}$
0.027	0.150	70.000	0.965 ± 0.017	$0.986^{+0.007}_{-0.006}$
0.027	0.250	40.000	0.971 ± 0.018	$0.987^{+0.007}_{-0.006}$
0.029	0.229	45.000	0.955 ± 0.017	$0.986^{+0.007}_{-0.006}$
0.030	0.180	60.000	0.969 ± 0.015	$0.985^{+0.007}_{-0.007}$
0.030	0.150	75.000	0.956 ± 0.017	$0.985^{+0.007}_{-0.007}$

Q^2 [GeV^2]	E [GeV]	θ [^{o}]	$\left(\frac{d\sigma}{d\Omega}\right)_{\rm exp} / \left(\frac{d\sigma}{d\Omega}\right)_{\rm dipole}$	$\left(\frac{d\sigma}{d\Omega}\right)_{\rm pQCD} / \left(\frac{d\sigma}{d\Omega}\right)_{\rm dipole}$
0.030	0.298	35.000	0.958 ± 0.016	$0.986^{+0.007}_{-0.007}$
0.031	0.129	92.640	0.991 ± 0.008	$0.985^{+0.007}_{-0.006}$
0.031	0.200	55.000	0.977 ± 0.007	$0.985^{+0.007}_{-0.007}$
0.033	0.150	80.000	0.980 ± 0.016	$0.984^{+0.008}_{-0.007}$
0.033	0.275	40.000	0.963 ± 0.017	$0.984^{+0.008}_{-0.007}$
0.034	0.180	65.000	0.963 ± 0.015	$0.984^{+0.008}_{-0.007}$
0.034	0.250	45.000	0.966 ± 0.017	$0.984^{+0.008}_{-0.007}$
0.034	0.229	50.000	0.957 ± 0.017	$0.984^{+0.008}_{-0.008}$
0.035	0.197	60.000	0.962 ± 0.031	$0.983^{+0.008}_{-0.008}$
0.036	0.200	60.000	0.986 ± 0.008	$0.983^{+0.008}_{-0.008}$
0.036	0.200	60.000	0.960 ± 0.017	$0.983^{+0.008}_{-0.008}$
0.038	0.180	70.000	0.966 ± 0.017	$0.982^{+0.009}_{-0.008}$
0.039	0.150	90.000	0.975 ± 0.016	$0.981^{+0.009}_{-0.008}$
0.039	0.298	40.000	0.956 ± 0.017	$0.982^{+0.009}_{-0.008}$
0.039	0.113	150.000	0.989 ± 0.029	$0.979^{+0.006}_{-0.005}$
0.039	0.208	60.000	0.966 ± 0.029	$0.982^{+0.009}_{-0.008}$
0.039	0.269	45.000	0.972 ± 0.025	$0.982^{+0.009}_{-0.009}$
0.040	0.229	55.000	0.936 ± 0.017	$0.981^{+0.009}_{-0.009}$
0.041	0.139	104.000	0.976 ± 0.029	$0.980^{+0.009}_{-0.008}$
0.041	0.250	50.000	0.955 ± 0.019	$0.981^{+0.010}_{-0.009}$
0.041	0.275	45.000	0.949 ± 0.017	$0.981^{+0.010}_{-0.009}$
0.042	0.180	75.000	0.965 ± 0.017	$0.980^{+0.010}_{-0.009}$
0.044	0.150	100.000	0.976 ± 0.016	$0.979^{+0.009}_{-0.009}$
0.046	0.200	70.000	0.955 ± 0.017	$0.979^{+0.010}_{-0.009}$
0.046	0.180	80.000	0.963 ± 0.019	$0.979^{+0.010}_{-0.009}$
0.047	0.229	60.000	0.944 ± 0.016	$0.979^{+0.011}_{-0.010}$
0.048	0.250	55.000	0.952 ± 0.019	$0.979^{+0.011}_{-0.010}$
0.048	0.298	45.000	0.951 ± 0.016	$0.979^{+0.011}_{-0.010}$
0.049	0.275	50.000	0.954 ± 0.016	$0.978^{+0.011}_{-0.010}$
0.050	0.150	110.000	0.968 ± 0.016	$0.977^{+0.010}_{-0.009}$
0.054	0.150	120.000	0.982 ± 0.016	$0.974^{+0.010}_{-0.009}$
0.054	0.180	90.000	0.961 ± 0.018	$0.975^{+0.011}_{-0.010}$
0.055	0.250	60.000	0.956 ± 0.016	$0.976^{+0.012}_{-0.011}$
0.056	0.200	80.000	0.954 ± 0.019	$0.975^{+0.012}_{-0.011}$
0.057	0.298	50.000	0.949 ± 0.017	$0.975^{+0.013}_{-0.012}$
0.057	0.275	55.000	0.949 ± 0.016	$0.975^{+0.013}_{-0.012}$
0.058	0.180	95.000	0.960 ± 0.018	$0.974^{+0.012}_{-0.011}$
0.058	0.150	130.000	0.982 ± 0.016	$0.972^{+0.009}_{-0.009}$

Q^2 [GeV^2]	E [GeV]	θ [^{o}]	$\left(\frac{d\sigma}{d\Omega}\right)_{\rm exp} / \left(\frac{d\sigma}{d\Omega}\right)_{\rm dipole}$	$\left(\frac{d\sigma}{d\Omega}\right)_{\rm pQCD} / \left(\frac{d\sigma}{d\Omega}\right)_{\rm dipole}$
0.059	0.229	70.000	0.952 ± 0.016	$0.975^{+0.013}_{-0.012}$
0.061	0.166	111.600	1.016 ± 0.031	$0.972^{+0.011}_{-0.010}$
0.062	0.161	120.000	1.048 ± 0.033	$0.972^{+0.011}_{-0.010}$
0.062	0.180	100.000	0.960 ± 0.018	$0.972^{+0.012}_{-0.011}$
0.062	0.152	135.000	1.017 ± 0.031	$0.971^{+0.009}_{-0.009}$
0.062	0.250	65.000	0.966 ± 0.019	$0.974^{+0.014}_{-0.012}$
0.063	0.194	90.000	1.007 ± 0.027	$0.973^{+0.013}_{-0.012}$
0.063	0.268	60.000	1.018 ± 0.027	$0.974^{+0.014}_{-0.013}$
0.066	0.200	90.000	0.960 ± 0.019	$0.972^{+0.013}_{-0.012}$
0.066	0.180	105.000	0.962 ± 0.018	$0.971^{+0.012}_{-0.011}$
0.066	0.229	75.000	0.954 ± 0.016	$0.972^{+0.014}_{-0.013}$
0.066	0.275	60.000	0.943 ± 0.017	$0.972^{+0.014}_{-0.013}$
0.067	0.298	55.000	0.941 ± 0.017	$0.972^{+0.015}_{-0.013}$
0.069	0.180	110.000	0.942 ± 0.018	$0.970^{+0.012}_{-0.011}$
0.070	0.250	70.000	0.954 ± 0.017	$0.971^{+0.015}_{-0.013}$
0.072	0.229	80.000	0.956 ± 0.018	$0.970^{+0.015}_{-0.013}$
0.072	0.180	115.000	0.952 ± 0.018	$0.968^{+0.012}_{-0.011}$
0.075	0.200	100.000	0.965 ± 0.018	$0.968^{+0.014}_{-0.013}$
0.076	0.180	120.000	0.948 ± 0.018	$0.967^{+0.012}_{-0.011}$
0.077	0.298	60.000	0.939 ± 0.017	$0.969^{+0.016}_{-0.015}$
0.077	0.250	75.000	0.963 ± 0.018	$0.969^{+0.016}_{-0.014}$
0.078	0.230	84.000	0.946 ± 0.028	$0.969^{+0.015}_{-0.014}$
0.078	0.167	150.000	0.964 ± 0.029	$0.965^{+0.009}_{-0.009}$
0.079	0.200	105.000	0.951 ± 0.019	$0.967^{+0.014}_{-0.013}$
0.079	0.390	45.000	0.978 ± 0.029	$0.969^{+0.017}_{-0.016}$
0.081	0.180	130.000	0.953 ± 0.016	$0.965^{+0.012}_{-0.011}$
0.083	0.200	110.000	0.945 ± 0.017	$0.965^{+0.014}_{-0.013}$
0.084	0.275	70.000	0.950 ± 0.016	$0.967^{+0.017}_{-0.016}$
0.084	0.229	90.000	0.957 ± 0.018	$0.967^{+0.016}_{-0.015}$
0.084	0.250	80.000	0.929 ± 0.019	$0.967^{+0.017}_{-0.015}$
0.086	0.180	140.000	0.970 ± 0.020	$0.963^{+0.011}_{-0.010}$
0.086	0.316	60.000	0.986 ± 0.027	$0.967^{+0.018}_{-0.016}$
0.087	0.298	65.000	0.940 ± 0.017	$0.966^{+0.018}_{-0.016}$
0.087	0.200	115.000	0.943 ± 0.017	$0.964^{+0.014}_{-0.013}$
0.091	0.200	120.000	0.955 ± 0.017	$0.962^{+0.014}_{-0.013}$
0.097	0.298	70.000	0.940 ± 0.016	$0.964^{+0.019}_{-0.017}$
0.097	0.200	130.000	0.948 ± 0.016	$0.960^{+0.013}_{-0.012}$
0.098	0.250	90.000	0.944 ± 0.019	$0.963^{+0.018}_{-0.016}$

Q^2 [GeV^2]	E [GeV]	θ [^{o}]	$\left(\frac{d\sigma}{d\Omega}\right)_{\rm exp} / \left(\frac{d\sigma}{d\Omega}\right)_{\rm dipole}$	$\left(\frac{d\sigma}{d\Omega}\right)_{\rm pQCD} / \left(\frac{d\sigma}{d\Omega}\right)_{\rm dipole}$
0.101	0.275	80.000	0.937 ± 0.016	$0.963^{+0.019}_{-0.017}$
0.102	0.200	140.000	0.939 ± 0.017	$0.958^{+0.013}_{-0.011}$
0.106	0.229	110.000	0.949 ± 0.019	$0.961^{+0.017}_{-0.015}$
0.111	0.229	115.000	0.951 ± 0.018	$0.959^{+0.017}_{-0.015}$
0.111	0.250	100.000	0.937 ± 0.021	$0.960^{+0.018}_{-0.017}$
0.115	0.229	120.000	0.949 ± 0.018	$0.958^{+0.016}_{-0.015}$
0.116	0.210	150.000	0.972 ± 0.031	$0.955^{+0.013}_{-0.012}$
0.117	0.249	105.000	0.977 ± 0.029	$0.959^{+0.019}_{-0.017}$
0.117	0.275	90.000	0.943 ± 0.016	$0.959^{+0.020}_{-0.018}$
0.120	0.605	35.200	0.909 ± 0.048	$0.960^{+0.024}_{-0.022}$
0.123	0.229	130.000	0.952 ± 0.019	$0.956^{+0.016}_{-0.014}$
0.123	0.250	110.000	0.941 ± 0.021	$0.958^{+0.019}_{-0.017}$
0.129	0.229	140.000	0.968 ± 0.018	$0.955^{+0.015}_{-0.014}$
0.132	0.275	100.000	0.934 ± 0.016	$0.956^{+0.021}_{-0.019}$
0.134	0.250	120.000	0.932 ± 0.020	$0.955^{+0.018}_{-0.017}$
0.142	0.250	130.000	0.939 ± 0.018	$0.954^{+0.018}_{-0.016}$
0.146	0.275	110.000	0.939 ± 0.016	$0.954^{+0.021}_{-0.019}$
0.148	0.242	150.000	0.928 ± 0.035	$0.952^{+0.015}_{-0.014}$
0.149	0.545	45.000	0.961 ± 0.031	$0.956^{+0.028}_{-0.026}$
0.150	0.250	140.000	0.968 ± 0.019	$0.952^{+0.017}_{-0.015}$
0.156	0.368	75.000	0.955 ± 0.030	$0.954^{+0.027}_{-0.024}$
0.156	0.259	135.000	0.895 ± 0.028	$0.952^{+0.018}_{-0.016}$
0.156	0.559	45.000	0.999 ± 0.031	$0.955^{+0.029}_{-0.027}$
0.158	0.275	120.000	0.948 ± 0.016	$0.952^{+0.020}_{-0.019}$
0.168	0.275	130.000	0.953 ± 0.016	$0.951^{+0.020}_{-0.018}$
0.176	0.275	140.000	0.956 ± 0.016	$0.950^{+0.019}_{-0.017}$
0.179	0.603	45.000	0.948 ± 0.029	$0.952^{+0.032}_{-0.030}$
0.179	0.351	90.000	0.918 ± 0.029	$0.952^{+0.027}_{-0.025}$
0.179	0.474	60.000	0.910 ± 0.029	$0.952^{+0.031}_{-0.028}$
0.179	0.297	120.000	0.906 ± 0.028	$0.949^{+0.022}_{-0.020}$
0.179	0.399	75.000	0.930 ± 0.029	$0.951^{+0.029}_{-0.027}$
0.179	0.282	135.000	0.945 ± 0.029	$0.949^{+0.020}_{-0.018}$
0.179	0.275	145.000	0.916 ± 0.029	$0.949^{+0.018}_{-0.017}$
0.183	0.275	150.000	0.952 ± 0.016	$0.949^{+0.018}_{-0.017}$
0.194	0.296	135.000	0.985 ± 0.030	$0.948^{+0.021}_{-0.019}$
0.195	0.418	75.000	1.020 ± 0.031	$0.950^{+0.031}_{-0.028}$
0.195	0.690	40.600	0.941 ± 0.029	$0.951^{+0.035}_{-0.032}$
0.211	0.311	135.000	0.942 ± 0.034	$0.948^{+0.022}_{-0.021}$

Q^2 [GeV^2]	E [GeV]	θ [^{o}]	$\left(\frac{d\sigma}{d\Omega}\right)_{\rm exp} / \left(\frac{d\sigma}{d\Omega}\right)_{\rm dipole}$	$\left(\frac{d\sigma}{d\Omega}\right)_{\rm pQCD} / \left(\frac{d\sigma}{d\Omega}\right)_{\rm dipole}$
0.211	0.438	75.000	0.960 ± 0.033	$0.950^{+0.033}_{-0.030}$
0.212	0.304	145.000	0.992 ± 0.036	$0.947^{+0.021}_{-0.019}$
0.212	0.328	120.000	0.994 ± 0.035	$0.949^{+0.025}_{-0.023}$
0.233	0.690	45.500	1.020 ± 0.031	$0.949^{+0.039}_{-0.035}$
0.233	0.331	135.000	0.910 ± 0.029	$0.949^{+0.024}_{-0.022}$
0.234	0.464	75.000	0.938 ± 0.029	$0.949^{+0.035}_{-0.032}$
0.234	0.550	60.000	0.955 ± 0.030	$0.949^{+0.037}_{-0.034}$
0.272	0.364	135.000	0.884 ± 0.028	$0.950^{+0.027}_{-0.025}$
0.273	0.434	95.000	0.854 ± 0.027	$0.950^{+0.035}_{-0.032}$
0.273	0.449	90.000	0.988 ± 0.036	$0.950^{+0.036}_{-0.033}$
0.273	0.600	60.000	0.952 ± 0.029	$0.948^{+0.041}_{-0.037}$
0.273	0.356	145.000	0.927 ± 0.029	$0.950^{+0.025}_{-0.024}$
0.273	0.508	75.000	0.954 ± 0.030	$0.949^{+0.039}_{-0.035}$
0.291	0.380	135.000	0.908 ± 0.029	$0.951^{+0.028}_{-0.027}$
0.292	0.399	120.000	0.879 ± 0.028	$0.950^{+0.031}_{-0.029}$
0.292	0.528	75.000	0.936 ± 0.029	$0.950^{+0.040}_{-0.037}$
0.292	0.624	60.000	0.947 ± 0.029	$0.949^{+0.043}_{-0.039}$
0.292	0.468	90.000	0.922 ± 0.029	$0.950^{+0.037}_{-0.034}$
0.311	0.396	135.000	0.901 ± 0.028	$0.952^{+0.030}_{-0.028}$
0.311	0.647	60.000	0.965 ± 0.030	$0.950^{+0.045}_{-0.041}$
0.311	0.647	60.000	0.902 ± 0.028	$0.950^{+0.045}_{-0.041}$
0.311	0.387	145.000	0.957 ± 0.030	$0.952^{+0.028}_{-0.027}$
0.311	0.690	55.300	0.894 ± 0.028	$0.949^{+0.045}_{-0.041}$
0.312	0.549	75.000	0.925 ± 0.029	$0.951^{+0.042}_{-0.038}$
0.312	0.416	120.000	0.973 ± 0.036	$0.952^{+0.032}_{-0.030}$
0.350	0.692	60.000	0.912 ± 0.029	$0.951^{+0.048}_{-0.044}$
0.350	0.588	75.000	0.932 ± 0.029	$0.952^{+0.045}_{-0.041}$
0.350	0.427	135.000	0.942 ± 0.029	$0.956^{+0.032}_{-0.031}$
0.388	1.249	31.700	0.916 ± 0.044	$0.952^{+0.056}_{-0.051}$
0.389	0.736	60.000	0.953 ± 0.029	$0.954^{+0.051}_{-0.047}$
0.389	0.457	135.000	0.927 ± 0.029	$0.960^{+0.035}_{-0.034}$
0.389	0.557	90.000	0.969 ± 0.036	$0.957^{+0.044}_{-0.041}$
0.389	0.557	90.000	0.958 ± 0.030	$0.957^{+0.044}_{-0.041}$
0.389	1.009	40.600	1.010 ± 0.137	$0.952^{+0.055}_{-0.050}$
0.389	1.009	40.600	0.967 ± 0.133	$0.952^{+0.055}_{-0.050}$
0.389	0.696	64.700	0.940 ± 0.043	$0.954^{+0.050}_{-0.046}$
0.389	0.447	145.000	0.941 ± 0.029	$0.961^{+0.033}_{-0.033}$
0.389	0.848	50.100	0.923 ± 0.044	$0.953^{+0.053}_{-0.048}$

Q^2 [GeV^2]	E [GeV]	θ [^{o}]	$\left(\frac{d\sigma}{d\Omega}\right)_{\rm exp} / \left(\frac{d\sigma}{d\Omega}\right)_{\rm dipole}$	$\left(\frac{d\sigma}{d\Omega}\right)_{\rm pQCD} / \left(\frac{d\sigma}{d\Omega}\right)_{\rm dipole}$
0.389	0.556	90.300	0.956 ± 0.044	$0.957^{+0.044}_{-0.041}$
0.390	0.627	75.000	0.941 ± 0.029	$0.955^{+0.048}_{-0.044}$
0.390	0.479	120.000	0.926 ± 0.029	$0.959^{+0.038}_{-0.036}$
0.390	1.231	32.300	0.939 ± 0.044	$0.952^{+0.056}_{-0.051}$
0.390	0.900	46.600	1.010 ± 0.031	$0.953^{+0.054}_{-0.049}$
0.390	1.142	35.200	0.944 ± 0.044	$0.953^{+0.055}_{-0.050}$
0.397	0.745	60.000	0.933 ± 0.031	$0.955^{+0.052}_{-0.047}$
0.397	0.485	120.000	0.957 ± 0.040	$0.960^{+0.038}_{-0.037}$
0.428	0.486	135.000	0.959 ± 0.030	$0.964^{+0.037}_{-0.037}$
0.429	0.664	75.000	0.951 ± 0.029	$0.959^{+0.050}_{-0.046}$
0.429	0.950	46.600	1.010 ± 0.031	$0.956^{+0.057}_{-0.052}$
0.467	0.900	53.000	0.974 ± 0.030	$0.959^{+0.058}_{-0.053}$
0.467	0.950	49.500	0.993 ± 0.030	$0.959^{+0.059}_{-0.054}$
0.467	0.504	145.000	0.969 ± 0.030	$0.970^{+0.038}_{-0.039}$
0.468	0.515	135.000	0.955 ± 0.030	$0.969^{+0.040}_{-0.040}$
0.468	0.700	75.000	0.947 ± 0.029	$0.962^{+0.053}_{-0.049}$
0.487	0.717	75.000	0.923 ± 0.029	$0.964^{+0.054}_{-0.050}$
0.506	0.950	52.500	1.010 ± 0.031	$0.963^{+0.061}_{-0.056}$
0.506	0.543	135.000	0.942 ± 0.029	$0.975^{+0.042}_{-0.043}$
0.507	0.735	75.000	0.918 ± 0.029	$0.967^{+0.055}_{-0.052}$
0.545	0.570	135.000	0.958 ± 0.030	$0.980^{+0.044}_{-0.045}$
0.545	0.950	55.600	1.050 ± 0.032	$0.967^{+0.062}_{-0.058}$
0.545	0.900	59.800	0.977 ± 0.030	$0.968^{+0.062}_{-0.057}$
0.545	0.769	75.000	0.923 ± 0.029	$0.971^{+0.058}_{-0.054}$
0.546	0.559	145.000	1.020 ± 0.031	$0.981^{+0.043}_{-0.044}$
0.579	1.171	44.500	0.943 ± 0.044	$0.969^{+0.067}_{-0.062}$
0.583	1.629	30.200	0.989 ± 0.045	$0.967^{+0.070}_{-0.065}$
0.583	0.597	135.000	0.988 ± 0.030	$0.985^{+0.046}_{-0.048}$
0.584	0.886	64.700	0.959 ± 0.044	$0.973^{+0.062}_{-0.059}$
0.584	0.647	110.000	0.959 ± 0.046	$0.982^{+0.051}_{-0.051}$
0.584	0.802	75.000	0.928 ± 0.029	$0.975^{+0.060}_{-0.057}$
0.584	0.718	90.000	1.020 ± 0.040	$0.978^{+0.056}_{-0.054}$
0.584	0.718	90.000	1.040 ± 0.048	$0.978^{+0.056}_{-0.054}$
0.584	1.522	32.700	0.953 ± 0.044	$0.967^{+0.070}_{-0.064}$
0.584	0.645	111.000	0.981 ± 0.046	$0.982^{+0.051}_{-0.051}$
0.585	0.717	90.300	0.973 ± 0.044	$0.978^{+0.056}_{-0.054}$
0.585	1.072	50.100	0.951 ± 0.044	$0.970^{+0.066}_{-0.061}$
0.585	0.950	58.800	1.050 ± 0.032	$0.972^{+0.064}_{-0.060}$

Q^2 [GeV^2]	E [GeV]	θ [^{o}]	$\left(\frac{d\sigma}{d\Omega}\right)_{\rm exp} / \left(\frac{d\sigma}{d\Omega}\right)_{\rm dipole}$	$\left(\frac{d\sigma}{d\Omega}\right)_{\rm pQCD} / \left(\frac{d\sigma}{d\Omega}\right)_{\rm dipole}$
0.585	0.718	90.100	0.972 ± 0.044	$0.978^{+0.056}_{-0.054}$
0.585	0.892	64.200	0.971 ± 0.044	$0.973^{+0.063}_{-0.059}$
0.585	1.042	52.000	0.977 ± 0.045	$0.971^{+0.066}_{-0.061}$
0.585	1.540	32.300	0.968 ± 0.044	$0.967^{+0.070}_{-0.064}$
0.586	1.431	35.200	0.975 ± 0.044	$0.968^{+0.069}_{-0.064}$
0.621	1.520	34.100	0.927 ± 0.085	$0.971^{+0.072}_{-0.066}$
0.623	0.624	135.000	0.974 ± 0.030	$0.991^{+0.048}_{-0.051}$
0.623	0.835	75.000	0.919 ± 0.029	$0.980^{+0.062}_{-0.059}$
0.623	1.652	31.000	1.040 ± 0.109	$0.971^{+0.072}_{-0.067}$
0.623	1.652	31.000	1.020 ± 0.107	$0.971^{+0.072}_{-0.067}$
0.623	0.900	67.000	0.980 ± 0.030	$0.978^{+0.064}_{-0.061}$
0.623	0.950	62.000	0.979 ± 0.030	$0.977^{+0.065}_{-0.062}$
0.623	0.802	80.000	0.996 ± 0.030	$0.981^{+0.060}_{-0.059}$
0.623	0.612	145.000	0.990 ± 0.030	$0.992^{+0.047}_{-0.050}$
0.661	0.867	75.000	0.973 ± 0.030	$0.984^{+0.064}_{-0.062}$
0.662	0.950	65.400	1.010 ± 0.031	$0.982^{+0.066}_{-0.064}$
0.662	0.651	135.000	1.050 ± 0.032	$0.997^{+0.050}_{-0.053}$
0.664	1.190	48.200	1.040 ± 0.072	$0.978^{+0.071}_{-0.067}$
0.665	1.680	31.700	0.981 ± 0.090	$0.975^{+0.075}_{-0.069}$
0.670	0.805	86.000	0.952 ± 0.033	$0.988^{+0.061}_{-0.061}$
0.681	0.883	75.000	1.010 ± 0.031	$0.986^{+0.064}_{-0.063}$
0.701	0.899	75.000	1.020 ± 0.031	$0.989^{+0.065}_{-0.064}$
0.701	0.864	80.000	0.970 ± 0.030	$0.990^{+0.064}_{-0.063}$
0.701	0.950	68.900	1.060 ± 0.032	$0.987^{+0.067}_{-0.066}$
0.701	0.677	135.000	0.977 ± 0.030	$1.002^{+0.052}_{-0.056}$
0.701	0.664	145.000	0.991 ± 0.030	$1.003^{+0.051}_{-0.055}$
0.739	0.930	75.000	1.110 ± 0.033	$0.993^{+0.067}_{-0.067}$
0.740	0.950	72.600	1.030 ± 0.031	$0.993^{+0.068}_{-0.067}$
0.740	0.703	135.000	1.040 ± 0.031	$1.007^{+0.054}_{-0.058}$
0.766	1.104	59.900	1.030 ± 0.041	$0.992^{+0.073}_{-0.071}$
0.778	0.784	110.000	1.010 ± 0.045	$1.008^{+0.060}_{-0.064}$
0.778	0.961	75.000	1.080 ± 0.032	$0.998^{+0.069}_{-0.069}$
0.778	0.728	135.000	1.180 ± 0.035	$1.012^{+0.056}_{-0.061}$
0.779	0.865	90.000	1.020 ± 0.041	$1.002^{+0.065}_{-0.067}$
0.779	0.900	83.800	0.933 ± 0.029	$1.001^{+0.066}_{-0.068}$
0.779	0.950	76.500	1.110 ± 0.033	$0.998^{+0.068}_{-0.069}$
0.779	1.789	32.700	0.981 ± 0.045	$0.985^{+0.080}_{-0.076}$
0.779	0.925	80.000	0.937 ± 0.029	$0.999^{+0.067}_{-0.068}$

Q^2 [GeV^2]	E [GeV]	θ [^{o}]	$\left(\frac{d\sigma}{d\Omega}\right)_{\rm exp} / \left(\frac{d\sigma}{d\Omega}\right)_{\rm dipole}$	$\left(\frac{d\sigma}{d\Omega}\right)_{\rm pQCD} / \left(\frac{d\sigma}{d\Omega}\right)_{\rm dipole}$
0.779	0.865	90.100	1.010 ± 0.046	$1.002^{+0.065}_{-0.067}$
0.779	0.715	145.000	1.020 ± 0.031	$1.014^{+0.055}_{-0.060}$
0.780	1.064	64.200	0.964 ± 0.046	$0.995^{+0.072}_{-0.071}$
0.780	1.392	44.500	1.000 ± 0.045	$0.989^{+0.077}_{-0.075}$
0.780	1.683	35.200	0.985 ± 0.050	$0.986^{+0.079}_{-0.076}$
0.784	1.190	55.000	1.040 ± 0.111	$0.992^{+0.075}_{-0.073}$
0.852	1.250	55.100	1.060 ± 0.090	$0.999^{+0.077}_{-0.077}$
0.856	0.764	145.000	1.160 ± 0.034	$1.024^{+0.059}_{-0.065}$
0.857	1.022	75.000	1.160 ± 0.034	$1.007^{+0.072}_{-0.074}$
0.857	1.975	31.000	1.110 ± 0.115	$0.992^{+0.083}_{-0.081}$
0.857	0.779	135.000	1.210 ± 0.035	$1.023^{+0.060}_{-0.066}$
0.857	0.950	85.100	1.010 ± 0.031	$1.010^{+0.069}_{-0.072}$
0.973	1.003	90.100	1.040 ± 0.048	$1.025^{+0.072}_{-0.078}$
0.973	0.915	110.000	1.000 ± 0.053	$1.031^{+0.068}_{-0.075}$
0.973	1.718	40.200	1.060 ± 0.046	$1.005^{+0.086}_{-0.086}$
0.974	1.224	64.200	1.030 ± 0.046	$1.014^{+0.079}_{-0.082}$
0.975	1.913	35.200	1.020 ± 0.045	$1.003^{+0.087}_{-0.087}$
1.002	1.048	86.000	1.050 ± 0.037	$1.026^{+0.074}_{-0.080}$
1.012	0.862	145.000	1.100 ± 0.033	$1.042^{+0.066}_{-0.074}$
1.090	0.910	145.000	1.060 ± 0.032	$1.051^{+0.069}_{-0.079}$
1.120	1.104	90.000	1.040 ± 0.053	$1.039^{+0.078}_{-0.086}$
1.167	1.135	90.100	1.050 ± 0.048	$1.043^{+0.079}_{-0.088}$
1.167	1.040	110.000	1.090 ± 0.068	$1.050^{+0.076}_{-0.086}$
1.167	1.162	86.000	1.050 ± 0.034	$1.041^{+0.080}_{-0.089}$
1.168	1.910	40.300	1.070 ± 0.059	$1.019^{+0.091}_{-0.096}$
1.168	1.375	64.200	1.080 ± 0.047	$1.031^{+0.085}_{-0.092}$
1.169	0.958	145.000	1.030 ± 0.031	$1.058^{+0.072}_{-0.083}$
1.169	2.358	31.000	1.160 ± 0.123	$1.015^{+0.093}_{-0.097}$
1.169	2.358	31.000	1.170 ± 0.122	$1.015^{+0.093}_{-0.097}$
1.169	2.358	31.000	1.070 ± 0.116	$1.015^{+0.093}_{-0.097}$
1.169	1.137	90.000	1.260 ± 0.144	$1.043^{+0.079}_{-0.088}$
1.169	1.137	90.000	1.140 ± 0.136	$1.043^{+0.079}_{-0.088}$
1.169	1.137	90.000	1.070 ± 0.036	$1.043^{+0.079}_{-0.088}$
1.362	1.512	64.700	1.090 ± 0.055	$1.044^{+0.091}_{-0.101}$
1.363	1.263	90.300	1.070 ± 0.053	$1.057^{+0.086}_{-0.098}$
1.364	1.160	111.000	1.060 ± 0.057	$1.065^{+0.082}_{-0.095}$
1.364	1.790	50.100	1.030 ± 0.049	$1.036^{+0.095}_{-0.103}$
1.501	1.383	86.000	1.070 ± 0.040	$1.063^{+0.090}_{-0.104}$

Q^2 [GeV^2]	E [GeV]	θ [^{o}]	$\left(\frac{d\sigma}{d\Omega}\right)_{\rm exp} / \left(\frac{d\sigma}{d\Omega}\right)_{\rm dipole}$	$\left(\frac{d\sigma}{d\Omega}\right)_{\rm pQCD} / \left(\frac{d\sigma}{d\Omega}\right)_{\rm dipole}$
1.514	1.700	59.900	0.914 ± 0.101	$1.049^{+0.096}_{-0.108}$
1.516	1.870	51.800	1.100 ± 0.103	$1.044^{+0.098}_{-0.109}$
1.517	2.250	40.000	0.954 ± 0.100	$1.037^{+0.101}_{-0.111}$
1.518	1.520	72.700	1.090 ± 0.094	$1.057^{+0.093}_{-0.106}$
1.518	1.520	72.700	1.160 ± 0.103	$1.057^{+0.093}_{-0.106}$
1.525	2.710	31.600	0.980 ± 0.088	$1.033^{+0.103}_{-0.112}$
1.525	2.710	31.600	1.030 ± 0.141	$1.033^{+0.103}_{-0.112}$
1.525	1.710	59.800	1.060 ± 0.092	$1.050^{+0.097}_{-0.108}$
1.557	1.282	110.000	1.110 ± 0.055	$1.076^{+0.088}_{-0.104}$
1.557	1.389	90.100	1.070 ± 0.060	$1.068^{+0.091}_{-0.106}$
1.558	1.661	64.200	1.140 ± 0.058	$1.054^{+0.096}_{-0.109}$
1.751	1.512	90.000	1.090 ± 0.041	$1.075^{+0.097}_{-0.114}$
1.752	1.597	80.000	1.160 ± 0.064	$1.070^{+0.098}_{-0.115}$
1.752	1.789	64.700	1.100 ± 0.053	$1.061^{+0.101}_{-0.116}$
1.752	1.513	90.000	1.160 ± 0.161	$1.075^{+0.097}_{-0.114}$
1.752	1.513	90.000	1.270 ± 0.183	$1.075^{+0.097}_{-0.114}$
1.753	1.544	86.000	1.090 ± 0.034	$1.073^{+0.098}_{-0.114}$
1.753	1.511	90.300	1.150 ± 0.061	$1.075^{+0.097}_{-0.114}$
1.753	2.988	31.000	1.300 ± 0.136	$1.039^{+0.108}_{-0.120}$
1.753	2.988	31.000	1.370 ± 0.141	$1.039^{+0.108}_{-0.120}$
1.753	2.988	31.000	1.190 ± 0.136	$1.039^{+0.108}_{-0.120}$
1.753	2.988	31.000	1.180 ± 0.124	$1.039^{+0.108}_{-0.120}$
1.754	1.397	111.000	1.090 ± 0.077	$1.083^{+0.095}_{-0.112}$
1.946	1.632	90.100	1.060 ± 0.069	$1.079^{+0.103}_{-0.121}$
1.964	1.644	90.000	1.130 ± 0.250	$1.079^{+0.104}_{-0.122}$
1.995	2.998	34.100	1.080 ± 0.044	$1.044^{+0.113}_{-0.128}$
2.001	1.699	86.000	1.090 ± 0.037	$1.077^{+0.105}_{-0.123}$
2.001	1.699	86.000	1.100 ± 0.034	$1.077^{+0.105}_{-0.123}$
2.330	1.670	129.000	1.230 ± 0.208	$1.093^{+0.111}_{-0.133}$
2.331	1.901	86.000	1.140 ± 0.042	$1.078^{+0.114}_{-0.135}$
2.331	2.630	47.100	1.110 ± 0.139	$1.053^{+0.119}_{-0.138}$
2.334	2.220	62.500	0.901 ± 0.120	$1.064^{+0.117}_{-0.137}$
2.335	2.670	46.100	1.040 ± 0.095	$1.052^{+0.119}_{-0.138}$
2.336	1.904	86.000	1.080 ± 0.035	$1.078^{+0.114}_{-0.135}$
2.337	1.870	90.000	0.989 ± 0.128	$1.080^{+0.114}_{-0.135}$
2.338	1.880	88.900	1.470 ± 0.139	$1.079^{+0.114}_{-0.135}$
2.341	3.460	32.100	1.050 ± 0.097	$1.042^{+0.121}_{-0.140}$
2.342	2.220	62.800	0.865 ± 0.086	$1.064^{+0.117}_{-0.137}$

Q^2 [GeV^2]	E [GeV]	θ [^{o}]	$\left(\frac{d\sigma}{d\Omega}\right)_{\rm exp} / \left(\frac{d\sigma}{d\Omega}\right)_{\rm dipole}$	$\left(\frac{d\sigma}{d\Omega}\right)_{\rm pQCD} / \left(\frac{d\sigma}{d\Omega}\right)_{\rm dipole}$
2.497	3.294	36.200	1.060 ± 0.044	$1.044^{+0.124}_{-0.145}$
2.498	2.998	41.400	1.060 ± 0.044	$1.047^{+0.123}_{-0.144}$
2.499	3.296	36.200	1.050 ± 0.045	$1.044^{+0.124}_{-0.145}$
2.922	2.216	90.000	1.550 ± 0.261	$1.070^{+0.126}_{-0.155}$
2.922	2.216	90.000	1.840 ± 0.323	$1.070^{+0.126}_{-0.155}$
2.922	4.070	31.000	1.380 ± 0.184	$1.033^{+0.132}_{-0.158}$
3.000	2.300	86.000	1.090 ± 0.047	$1.066^{+0.127}_{-0.157}$
3.000	2.300	86.000	1.100 ± 0.036	$1.066^{+0.127}_{-0.157}$
3.112	3.470	41.200	0.944 ± 0.102	$1.036^{+0.133}_{-0.163}$
3.117	4.120	32.200	1.100 ± 0.115	$1.029^{+0.134}_{-0.163}$
3.121	2.670	65.200	1.050 ± 0.134	$1.052^{+0.131}_{-0.162}$
3.743	3.996	40.000	1.040 ± 0.045	$1.018^{+0.141}_{-0.179}$
3.895	2.777	90.000	1.920 ± 0.544	$1.039^{+0.139}_{-0.181}$
3.895	2.777	90.000	1.920 ± 0.449	$1.039^{+0.139}_{-0.181}$
3.895	2.777	90.000	2.010 ± 0.608	$1.039^{+0.139}_{-0.181}$
3.896	4.874	31.000	1.320 ± 0.154	$1.007^{+0.143}_{-0.182}$
3.896	4.874	31.000	1.330 ± 0.203	$1.007^{+0.143}_{-0.182}$
3.896	4.874	31.000	1.340 ± 0.241	$1.007^{+0.143}_{-0.182}$
4.142	3.870	47.300	1.020 ± 0.114	$1.010^{+0.144}_{-0.187}$
4.188	3.110	76.500	1.000 ± 0.112	$1.024^{+0.142}_{-0.187}$
4.275	3.460	61.500	1.180 ± 0.157	$1.014^{+0.144}_{-0.189}$
4.895	4.340	47.600	0.940 ± 0.106	$0.987^{+0.149}_{-0.201}$
5.879	4.960	47.500	0.975 ± 0.110	$0.958^{+0.153}_{-0.215}$
6.830	5.540	47.500	0.840 ± 0.098	$0.932^{+0.159}_{-0.226}$
7.826	6.130	47.600	0.894 ± 0.102	$0.907^{+0.166}_{-0.234}$
8.774	5.710	75.100	0.927 ± 0.283	$0.882^{+0.168}_{-0.239}$
9.560	6.130	75.700	1.040 ± 0.419	$0.862^{+0.171}_{-0.242}$

Table 8.2: Comparison of the fit to the cross section data within the pQCD approach to the experimental results. Here Q^2 is the invariant four-momentum transfer squared, E is the incoming electron energy, θ is the electron scattering angle, $\left(\frac{d\sigma}{d\Omega}\right)_{\rm exp} / \left(\frac{d\sigma}{d\Omega}\right)_{\rm dipole}$ is the experimental cross section data normalised to the dipole cross section, and $\left(\frac{d\sigma}{d\Omega}\right)_{\rm pQCD} / \left(\frac{d\sigma}{d\Omega}\right)_{\rm dipole}$ is the Coulomb-corrected cross section obtained in the cross section fit within the pQCD approach.

Results of the $\Delta^{2\gamma}$ extraction

Table 8.3 gives the numerical results of the estimates of the two-photon exchange corrections in both the SC and the pQCD approaches.

Q^2 [GeV^2]	ϵ	$\Delta^{2\gamma}_{\mathrm{SC}}$	$\Delta^{2\gamma}_{\mathrm{pQCD}}$
0.25	0.00	-0.01155 ± 0.00900	-0.00991 ± 0.01869
0.25	0.10	-0.00467 ± 0.00856	-0.00787 ± 0.02391
0.25	0.20	0.00051 ± 0.00605	-0.00642 ± 0.02814
0.25	0.30	0.00450 ± 0.00568	-0.00527 ± 0.03105
0.25	0.40	0.00764 ± 0.00588	-0.00431 ± 0.03333
0.25	0.50	0.01025 ± 0.00554	-0.00360 ± 0.03532
0.25	0.60	0.01234 ± 0.00594	-0.00296 ± 0.03686
0.25	0.70	0.01414 ± 0.00577	-0.00244 ± 0.03820
0.25	0.80	0.01569 ± 0.00542	-0.00200 ± 0.03934
0.25	0.90	0.01699 ± 0.00446	-0.00161 ± 0.04029
0.50	0.00	-0.02009 ± 0.01867	-0.01005 ± 0.03192
0.50	0.10	-0.01382 ± 0.01820	-0.00807 ± 0.03723
0.50	0.20	-0.00827 ± 0.01603	-0.00625 ± 0.04204
0.50	0.30	-0.00351 ± 0.01426	-0.00474 ± 0.04592
0.50	0.40	0.00068 ± 0.01335	-0.00338 ± 0.04905
0.50	0.50	0.00436 ± 0.01449	-0.00220 ± 0.05169
0.50	0.60	0.00762 ± 0.01476	-0.00115 ± 0.05408
0.50	0.70	0.01053 ± 0.01465	-0.00021 ± 0.05620
0.50	0.80	0.01315 ± 0.01525	0.00063 ± 0.05811
0.50	0.90	0.01552 ± 0.01538	0.00139 ± 0.05983
0.75	0.00	-0.02649 ± 0.02812	-0.01156 ± 0.04182
0.75	0.10	-0.02121 ± 0.02771	-0.00951 ± 0.04655
0.75	0.20	-0.01622 ± 0.02626	-0.00764 ± 0.05133
0.75	0.30	-0.01171 ± 0.02438	-0.00599 ± 0.05550
0.75	0.40	-0.00757 ± 0.02282	-0.00446 ± 0.05925
0.75	0.50	-0.00379 ± 0.02264	-0.00307 ± 0.06234
0.75	0.60	-0.00033 ± 0.02353	-0.00178 ± 0.06497
0.75	0.70	0.00288 ± 0.02367	-0.00061 ± 0.06717
0.75	0.80	0.00584 ± 0.02392	0.00049 ± 0.06917
0.75	0.90	0.00859 ± 0.02491	0.00151 ± 0.07101
1.00	0.00	-0.03147 ± 0.03745	-0.01776 ± 0.04979
1.00	0.10	-0.02702 ± 0.03711	-0.01550 ± 0.05419
1.00	0.20	-0.02273 ± 0.03626	-0.01360 ± 0.05837
1.00	0.30	-0.01871 ± 0.03407	-0.01180 ± 0.06220
1.00	0.40	-0.01495 ± 0.03266	-0.01010 ± 0.06574
1.00	0.50	-0.01142 ± 0.03139	-0.00854 ± 0.06917
1.00	0.60	-0.00811 ± 0.03164	-0.00704 ± 0.07206
1.00	0.70	-0.00500 ± 0.03185	-0.00567 ± 0.07469

Q^2 [GeV^2]	ϵ	$\Delta^{2\gamma}_{\rm SC}$	$\Delta^{2\gamma}_{\rm pQCD}$
1.00	0.80	-0.00207 ± 0.03203	-0.00433 ± 0.07680
1.00	0.90	0.00069 ± 0.03241	-0.00309 ± 0.07870
1.25	0.00	-0.03531 ± 0.04592	-0.02761 ± 0.05632
1.25	0.10	-0.03157 ± 0.04519	-0.02534 ± 0.06026
1.25	0.20	-0.02785 ± 0.04456	-0.02328 ± 0.06420
1.25	0.30	-0.02433 ± 0.04353	-0.02133 ± 0.06785
1.25	0.40	-0.02098 ± 0.04198	-0.01949 ± 0.07124
1.25	0.50	-0.01780 ± 0.04067	-0.01773 ± 0.07435
1.25	0.60	-0.01477 ± 0.03949	-0.01604 ± 0.07716
1.25	0.70	-0.01189 ± 0.03977	-0.01444 ± 0.07981
1.25	0.80	-0.00913 ± 0.04001	-0.01292 ± 0.08214
1.25	0.90	-0.00649 ± 0.04023	-0.01144 ± 0.08392
1.50	0.00	-0.03813 ± 0.05316	-0.03939 ± 0.06197
1.50	0.10	-0.03491 ± 0.05232	-0.03703 ± 0.06530
1.50	0.20	-0.03169 ± 0.05160	-0.03486 ± 0.06891
1.50	0.30	-0.02861 ± 0.05092	-0.03278 ± 0.07237
1.50	0.40	-0.02564 ± 0.05051	-0.03077 ± 0.07565
1.50	0.50	-0.02279 ± 0.04928	-0.02884 ± 0.07863
1.50	0.60	-0.02004 ± 0.04755	-0.02698 ± 0.08144
1.50	0.70	-0.01739 ± 0.04731	-0.02519 ± 0.08412
1.50	0.80	-0.01485 ± 0.04762	-0.02345 ± 0.08663
1.50	0.90	-0.01239 ± 0.04789	-0.02177 ± 0.08869
1.75	0.00	-0.04009 ± 0.06008	-0.05144 ± 0.06806
1.75	0.10	-0.03729 ± 0.05918	-0.04901 ± 0.07099
1.75	0.20	-0.03444 ± 0.05838	-0.04674 ± 0.07402
1.75	0.30	-0.03169 ± 0.05762	-0.04453 ± 0.07691
1.75	0.40	-0.02901 ± 0.05721	-0.04238 ± 0.07967
1.75	0.50	-0.02643 ± 0.05714	-0.04031 ± 0.08227
1.75	0.60	-0.02393 ± 0.05553	-0.03828 ± 0.08495
1.75	0.70	-0.02149 ± 0.05452	-0.03632 ± 0.08755
1.75	0.80	-0.01915 ± 0.05482	-0.03441 ± 0.09006
1.75	0.90	-0.01686 ± 0.05514	-0.03256 ± 0.09223
2.00	0.00	-0.04124 ± 0.06675	-0.06273 ± 0.07379
2.00	0.10	-0.03872 ± 0.06579	-0.06027 ± 0.07643
2.00	0.20	-0.03616 ± 0.06492	-0.05789 ± 0.07915
2.00	0.30	-0.03366 ± 0.06409	-0.05558 ± 0.08178
2.00	0.40	-0.03123 ± 0.06331	-0.05331 ± 0.08431
2.00	0.50	-0.02885 ± 0.06326	-0.05110 ± 0.08662
2.00	0.60	-0.02654 ± 0.06264	-0.04894 ± 0.08885
2.00	0.70	-0.02428 ± 0.06177	-0.04682 ± 0.09103
2.00	0.80	-0.02208 ± 0.06162	-0.04476 ± 0.09317
2.00	0.90	-0.01994 ± 0.06163	-0.04274 ± 0.09503
2.25	0.00	-0.04163 ± 0.07317	-0.07272 ± 0.07906

Q^2 [GeV^2]	ϵ	$\Delta^{2\gamma}_{\mathrm{SC}}$	$\Delta^{2\gamma}_{\mathrm{pQCD}}$
2.25	0.10	-0.03935 ± 0.07217	-0.07023 ± 0.08145
2.25	0.20	-0.03698 ± 0.07125	-0.06776 ± 0.08405
2.25	0.30	-0.03466 ± 0.07034	-0.06533 ± 0.08660
2.25	0.40	-0.03240 ± 0.06905	-0.06296 ± 0.08909
2.25	0.50	-0.03018 ± 0.06841	-0.06063 ± 0.09142
2.25	0.60	-0.02800 ± 0.06789	-0.05834 ± 0.09363
2.25	0.70	-0.02588 ± 0.06759	-0.05609 ± 0.09579
2.25	0.80	-0.02378 ± 0.06742	-0.05388 ± 0.09787
2.25	0.90	-0.02174 ± 0.06761	-0.05172 ± 0.09959
2.50	0.00	-0.04139 ± 0.07854	-0.08124 ± 0.08475
2.50	0.10	-0.03922 ± 0.07783	-0.07862 ± 0.08709
2.50	0.20	-0.03699 ± 0.07718	-0.07606 ± 0.08956
2.50	0.30	-0.03480 ± 0.07607	-0.07353 ± 0.09198
2.50	0.40	-0.03265 ± 0.07454	-0.07105 ± 0.09435
2.50	0.50	-0.03052 ± 0.07352	-0.06858 ± 0.09664
2.50	0.60	-0.02845 ± 0.07325	-0.06618 ± 0.09875
2.50	0.70	-0.02639 ± 0.07298	-0.06378 ± 0.10083
2.50	0.80	-0.02439 ± 0.07271	-0.06147 ± 0.10273
2.50	0.90	-0.02242 ± 0.07266	-0.05916 ± 0.10438
2.75	0.00	-0.04045 ± 0.08332	-0.08794 ± 0.09036
2.75	0.10	-0.03841 ± 0.08255	-0.08534 ± 0.09257
2.75	0.20	-0.03627 ± 0.08184	-0.08268 ± 0.09491
2.75	0.30	-0.03415 ± 0.08142	-0.08005 ± 0.09720
2.75	0.40	-0.03207 ± 0.08039	-0.07744 ± 0.09945
2.75	0.50	-0.03002 ± 0.07888	-0.07488 ± 0.10166
2.75	0.60	-0.02799 ± 0.07849	-0.07234 ± 0.10375
2.75	0.70	-0.02599 ± 0.07821	-0.06982 ± 0.10575
2.75	0.80	-0.02402 ± 0.07792	-0.06735 ± 0.10744
2.75	0.90	-0.02208 ± 0.07764	-0.06491 ± 0.10905
3.00	0.00	-0.03898 ± 0.08832	-0.09308 ± 0.09579
3.00	0.10	-0.03698 ± 0.08761	-0.09037 ± 0.09788
3.00	0.20	-0.03489 ± 0.08712	-0.08761 ± 0.10011
3.00	0.30	-0.03281 ± 0.08660	-0.08486 ± 0.10230
3.00	0.40	-0.03076 ± 0.08574	-0.08214 ± 0.10445
3.00	0.50	-0.02874 ± 0.08420	-0.07945 ± 0.10658
3.00	0.60	-0.02673 ± 0.08361	-0.07678 ± 0.10865
3.00	0.70	-0.02476 ± 0.08331	-0.07415 ± 0.11045
3.00	0.80	-0.02280 ± 0.08299	-0.07153 ± 0.11205
3.00	0.90	-0.02088 ± 0.08257	-0.06897 ± 0.11364
3.25	0.00	-0.03696 ± 0.09361	-0.09653 ± 0.10108
3.25	0.10	-0.03499 ± 0.09265	-0.09375 ± 0.10307
3.25	0.20	-0.03291 ± 0.09193	-0.09087 ± 0.10521
3.25	0.30	-0.03085 ± 0.09124	-0.08802 ± 0.10731

Q^2 [GeV^2]	ϵ	$\Delta^{2\gamma}_{\rm SC}$	$\Delta^{2\gamma}_{\rm pQCD}$
3.25	0.40	-0.02881 ± 0.09037	-0.08518 ± 0.10937
3.25	0.50	-0.02679 ± 0.08936	-0.08237 ± 0.11132
3.25	0.60	-0.02478 ± 0.08861	-0.07956 ± 0.11326
3.25	0.70	-0.02281 ± 0.08823	-0.07681 ± 0.11505
3.25	0.80	-0.02085 ± 0.08776	-0.07406 ± 0.11663
3.25	0.90	-0.01890 ± 0.08727	-0.07134 ± 0.11819
3.50	0.00	-0.03443 ± 0.09845	-0.09838 ± 0.10624
3.50	0.10	-0.03248 ± 0.09740	-0.09555 ± 0.10814
3.50	0.20	-0.03040 ± 0.09655	-0.09256 ± 0.11010
3.50	0.30	-0.02833 ± 0.09579	-0.08957 ± 0.11204
3.50	0.40	-0.02628 ± 0.09491	-0.08662 ± 0.11397
3.50	0.50	-0.02424 ± 0.09386	-0.08369 ± 0.11587
3.50	0.60	-0.02223 ± 0.09319	-0.08078 ± 0.11776
3.50	0.70	-0.02022 ± 0.09288	-0.07788 ± 0.11962
3.50	0.80	-0.01823 ± 0.09239	-0.07499 ± 0.12119
3.50	0.90	-0.01626 ± 0.09190	-0.07213 ± 0.12274
3.75	0.00	-0.03149 ± 0.10319	-0.09885 ± 0.11108
3.75	0.10	-0.02951 ± 0.10208	-0.09586 ± 0.11285
3.75	0.20	-0.02740 ± 0.10111	-0.09275 ± 0.11477
3.75	0.30	-0.02531 ± 0.10026	-0.08966 ± 0.11666
3.75	0.40	-0.02322 ± 0.09925	-0.08657 ± 0.11855
3.75	0.50	-0.02116 ± 0.09801	-0.08352 ± 0.12042
3.75	0.60	-0.01912 ± 0.09730	-0.08047 ± 0.12227
3.75	0.70	-0.01707 ± 0.09713	-0.07743 ± 0.12411
3.75	0.80	-0.01505 ± 0.09695	-0.07441 ± 0.12577
3.75	0.90	-0.01304 ± 0.09645	-0.07141 ± 0.12732
4.00	0.00	-0.02810 ± 0.10722	-0.09782 ± 0.11580
4.00	0.10	-0.02611 ± 0.10614	-0.09479 ± 0.11754
4.00	0.20	-0.02397 ± 0.10517	-0.09156 ± 0.11941
4.00	0.30	-0.02184 ± 0.10432	-0.08834 ± 0.12128
4.00	0.40	-0.01972 ± 0.10340	-0.08513 ± 0.12314
4.00	0.50	-0.01761 ± 0.10210	-0.08194 ± 0.12498
4.00	0.60	-0.01551 ± 0.10096	-0.07874 ± 0.12681
4.00	0.70	-0.01343 ± 0.10085	-0.07558 ± 0.12863
4.00	0.80	-0.01136 ± 0.10093	-0.07244 ± 0.13036
4.00	0.90	-0.00929 ± 0.10091	-0.06929 ± 0.13193
4.25	0.00	-0.02435 ± 0.11120	-0.09556 ± 0.12050
4.25	0.10	-0.02232 ± 0.11004	-0.09243 ± 0.12221
4.25	0.20	-0.02014 ± 0.10900	-0.08908 ± 0.12407
4.25	0.30	-0.01796 ± 0.10806	-0.08574 ± 0.12591
4.25	0.40	-0.01579 ± 0.10712	-0.08240 ± 0.12775
4.25	0.50	-0.01364 ± 0.10608	-0.07909 ± 0.12958
4.25	0.60	-0.01149 ± 0.10490	-0.07578 ± 0.13139

Q^2 [GeV^2]	ϵ	$\Delta^{2\gamma}_{\mathrm{SC}}$	$\Delta^{2\gamma}_{\mathrm{pQCD}}$
4.25	0.70	-0.00935 ± 0.10453	-0.07248 ± 0.13320
4.25	0.80	-0.00722 ± 0.10454	-0.06919 ± 0.13497
4.25	0.90	-0.00510 ± 0.10454	-0.06591 ± 0.13660
4.50	0.00	-0.02028 ± 0.11515	-0.09218 ± 0.12520
4.50	0.10	-0.01819 ± 0.11390	-0.08890 ± 0.12690
4.50	0.20	-0.01595 ± 0.11282	-0.08543 ± 0.12874
4.50	0.30	-0.01372 ± 0.11177	-0.08197 ± 0.13058
4.50	0.40	-0.01150 ± 0.11078	-0.07851 ± 0.13240
4.50	0.50	-0.00929 ± 0.10997	-0.07507 ± 0.13422
4.50	0.60	-0.00708 ± 0.10919	-0.07162 ± 0.13603
4.50	0.70	-0.00488 ± 0.10832	-0.06819 ± 0.13783
4.50	0.80	-0.00269 ± 0.10812	-0.06475 ± 0.13961
4.50	0.90	-0.00051 ± 0.10805	-0.06135 ± 0.14134
4.75	0.00	-0.01587 ± 0.11914	-0.08763 ± 0.12972
4.75	0.10	-0.01375 ± 0.11786	-0.08430 ± 0.13145
4.75	0.20	-0.01145 ± 0.11670	-0.08071 ± 0.13333
4.75	0.30	-0.00916 ± 0.11579	-0.07712 ± 0.13519
4.75	0.40	-0.00687 ± 0.11488	-0.07354 ± 0.13701
4.75	0.50	-0.00460 ± 0.11399	-0.06995 ± 0.13878
4.75	0.60	-0.00233 ± 0.11309	-0.06639 ± 0.14055
4.75	0.70	-0.00007 ± 0.11220	-0.06283 ± 0.14231
4.75	0.80	0.00219 ± 0.11167	-0.05926 ± 0.14406
4.75	0.90	0.00444 ± 0.11152	-0.05572 ± 0.14581
5.00	0.00	-0.01120 ± 0.12332	-0.08219 ± 0.13424
5.00	0.10	-0.00902 ± 0.12216	-0.07874 ± 0.13596
5.00	0.20	-0.00666 ± 0.12111	-0.07502 ± 0.13783
5.00	0.30	-0.00430 ± 0.12006	-0.07131 ± 0.13966
5.00	0.40	-0.00195 ± 0.11901	-0.06760 ± 0.14145
5.00	0.50	0.00039 ± 0.11797	-0.06390 ± 0.14323
5.00	0.60	0.00273 ± 0.11694	-0.06020 ± 0.14500
5.00	0.70	0.00506 ± 0.11590	-0.05650 ± 0.14678
5.00	0.80	0.00739 ± 0.11497	-0.05280 ± 0.14854
5.00	0.90	0.00971 ± 0.11487	-0.04912 ± 0.15031

Table 8.3: Values of $\Delta^{2\gamma}$ in both the SC and the pQCD approaches. Here Q^2 is the invariant four-momentum transfer squared and ϵ is the virtual photon polarisation.

References

[ABCC05] A. V. Afanasev, S. J. Brodsky, C. E. Carlson, Y. C. Chen and M. Vanderhaeghen, Phys. Rev. D **72**, 013008 (2005) [arXiv:hep-ph/0502013].

[Abl05] M. Ablikim *et al.* [BES Collaboration], Phys. Lett. B **630** (2005) 14 [arXiv:hep-ex/0506059].

[ACG80] R. G. Arnold, C. E. Carlson and F. Gross, Phys. Rev. C **23** (1981) 363.

[Ach05] M. N. Achasov *et al.*, J. Exp. Theor. Phys. **101** (2005) 1053 [Zh. Eksp. Teor. Fiz. **101** (2005) 1201] [arXiv:hep-ex/0506076].

[Akh99] R. R. Akhmetshin *et al.* [CMD-2 Collaboration], arXiv:hep-ex/9904027.
R. R. Akhmetshin *et al.* [CMD-2 Collaboration], Phys. Lett. B **527** (2002) 161 [arXiv:hep-ex/0112031].
R. R. Akhmetshin *et al.* [CMD-2 Collaboration], Phys. Lett. B **578** (2004) 285 [arXiv:hep-ex/0308008].

[AKNT06] C. Alexandrou, G. Koutsou, J. W. Negele and A. Tsapalis, Phys. Rev. D **74** (2006) 034508 [arXiv:hep-lat/0605017].

[Ale06] C. Alexandrou, arXiv:hep-lat/0608025.

[Alo04] A. Aloisio *et al.* [KLOE Collaboration], Phys. Lett. B **606** (2005) 12 [arXiv:hep-ex/0407048].

[Amb99] M. Ambrogiani *et al.* [E835 Collaboration], Phys. Rev. D **60** (1999) 032002.

[And06] B. Anderson *et al.* [Jefferson Lab E95-001 Collaboration], arXiv:nucl-ex/0605006.

[Ani98] K. A. Aniol *et al.* [HAPPEX Collaboration], Phys. Rev. Lett. **82** (1999) 1096 [arXiv:nucl-ex/9810012].

[Ant93] A. Antonelli *et al.*, Phys. Lett. B **313** (1993) 283.

[Ant94] A. Antonelli *et al.*, Phys. Lett. B **334** (1994) 431.

[Ant98] A. Antonelli *et al.*, Nucl. Phys. B **517** (1998) 3.

[AR68] A. I. Akhiezer and M. P. Rekalo, Sov. Phys. Dokl. **13** (1968) 572 [Dokl. Akad. Nauk Ser. Fiz. **180** (1968) 1081].

[AR74] A. I. Akhiezer and M. P. Rekalo, Sov. J. Part. Nucl. **4** (1974) 277 [Fiz. Elem. Chast. Atom. Yadra **4** (1973) 662].

[Arr03] J. Arrington, Phys. Rev. C **68** (2003) 034325 [arXiv:nucl-ex/0305009].

[Aub05] B. Aubert *et al.* [BABAR Collaboration], Phys. Rev. D **73** (2006) 012005 [arXiv:hep-ex/0512023].

[Bar94] G. Bardin *et al.*, Nucl. Phys. B **411** (1994) 3.

[Bas77] G. Bassompierre *et al.* [Mulhouse-Strasbourg-Turin Collaboration], Phys. Lett. B **68** (1977) 477.

[Ber03] J. Bermuth *et al.*, Phys. Lett. B **564** (2003) 199 [arXiv:nucl-ex/0303015].

[BFHM98] V. Bernard, H. W. Fearing, T. R. Hemmert and U.-G. Meißner, Nucl. Phys. A **635** (1998) 121 [Erratum-ibid. A **642** (1998 NUPHA,A642,563-563.1998) 563] [arXiv:hep-ph/9801297].

[BGKP01] S. Boffi, L. Y. Glozman, W. Klink, W. Plessas, M. Radici and R. F. Wagenbrunn, Eur. Phys. J. A **14** (2002) 17 [arXiv:hep-ph/0108271].

[BHM05] M. A. Belushkin, H.-W. Hammer and U.-G. Meißner, Phys. Lett. B **633**, 507 (2006) [arXiv:hep-ph/0510382].

[Bis90] D. Bisello *et al.* [DM2 Collaboration], Z. Phys. C **48** (1990) 23.

[BJY02] A. V. Belitsky, X. d. Ji and F. Yuan, Phys. Rev. Lett. **91** (2003) 092003 [arXiv:hep-ph/0212351].

[BKM96] V. Bernard, N. Kaiser and U.-G. Meißner, Nucl. Phys. A **611** (1996) 429 [arXiv:hep-ph/9607428].

[BMT03] P. G. Blunden, W. Melnitchouk and J. A. Tjon, Phys. Rev. Lett. **91** (2003) 142304 [arXiv:nucl-th/0306076].

[BMT05] P. G. Blunden, W. Melnitchouk and J. A. Tjon, Phys. Rev. C **72** (2005) 034612 [arXiv:nucl-th/0506039].

[Bou96] S. Bourzeix *et al.*, Phys. Rev. Lett. **76**, 384 (1996)

[BS05] P. G. Blunden and I. Sick, Phys. Rev. C **72** (2005) 057601 [arXiv:nucl-th/0508037].

[CABC04] Y. C. Chen, A. Afanasev, S. J. Brodsky, C. E. Carlson and M. Vanderhaeghen, Phys. Rev. Lett. **93**, 122301 (2004) [arXiv:hep-ph/0403058].

[CKGZ58] G. F. Chew, R. Karplus, S. Gasiorowicz and F. Zachariasen, Phys. Rev. **110** (1958) 265.

[CPSS95] F. Cardarelli, E. Pace, G. Salme and S. Simula, Phys. Lett. B **357** (1995) 267 [arXiv:nucl-th/9507037].

[CS00] F. Cardarelli and S. Simula, Phys. Rev. C **62** (2000) 065201 [arXiv:nucl-th/0006023].

[Del79] B. Delcourt *et al.*, Phys. Lett. B **86** (1979) 395.

[Dom69] N. Dombey, Rev. Mod. Phys. **41** (1969) 236.

[DR85] T. W. Donnelly and A. S. Raskin, Annals Phys. **169** (1986) 247.

[FF59] W. R. Frazer and J. R. Fulco, Phys. Rev. Lett. **2** (1959) 365.

[FF60a] W. R. Frazer and J. R. Fulco, Phys. Rev. **117** (1960) 1603.

[FF60b] W. R. Frazer and J. R. Fulco, Phys. Rev. **117** (1960) 1609.

[FGT58] P. Federbush, M. L. Goldberger and S. B. Treiman, Phys. Rev. **112** (1958) 642.

[FHK38] H. Fröhlich, W. Heitler, N. Kemmer, Proc. R. Soc. A **166** (1938) 155.

[Fis04] K. G. Fissum *et al.* [Jefferson Lab Hall A Collaboration], Phys. Rev. C **70** (2004) 034606 [arXiv:nucl-ex/0401021].

[Fol52] L. L. Foldy, Phys. Rev. **87** (1952) 688.

[FS33] R. Frisch and O. Stern, Z. Phys. **85** (1933) 4.

[FW89] S. Furuichi and K. Watanabe, Prog. Theor. Phys. **82** (1989) 581.

[FW03] J. Friedrich and T. Walcher, Eur. Phys. J. A **17** (2003) 607 [arXiv:hep-ph/0303054].

[GA04] F. Gross and P. Agbakpe, Phys. Rev. C **73** (2006) 015203 [arXiv:nucl-th/0411090].

[Gel62] M. Gell-Mann, Phys. Rev. **125** (1962) 1067.

[Gel64] M. Gell-Mann, Phys. Lett. **8** (1964) 214.

[GHHP03] M. Göckeler, T. R. Hemmert, R. Horsley, D. Pleiter, P. E. L. Rakow, A. Schafer and G. Schierholz [QCDSF Collaboration], Phys. Rev. D **71** (2005) 034508 [arXiv:hep-lat/0303019].

[Gla04] D. I. Glazier *et al.*, Eur. Phys. J. A **24** (2005) 101 [arXiv:nucl-ex/0410026].

[GNO57] M. L. Goldberger, Y. Nambu and O. Oehme, Ann. Phys. **2** (1957) 226.

[GPRV04] M. Guidal, M. V. Polyakov, A. V. Radyushkin and M. Vanderhaeghen, Phys. Rev. D **72** (2005) 054013 [arXiv:hep-ph/0410251].

[GR55] Donald A. Glaser and David C. Rahm, Phys. Rev. **97** (1955) 474.

[Gre77] W. Grein, Nucl. Phys. B **131** (1977) 255.

[GS68] G. J. Gounaris and J. J. Sakurai, Phys. Rev. Lett. **21**, 244 (1968).

[GSL] M. Galassi et al., GNU Scientific Library Reference Manual, 2nd revised edition (Network Theory Limited, 2006).

[GSS87] J. Gasser, M. E. Sainio and A. Svarc, Nucl. Phys. B **307** (1988) 779.

[HA55] R. Hofstadter and R. W. McAllister, Phys. Rev. **98** (1955) 217.

[HDM03] H.-W. Hammer, D. Drechsel and U.-G. Meißner, Phys. Lett. B **586** (2004) 291 [arXiv:hep-ph/0310240].

[Hei32] W. Heisenberg, Z. Phys. **77** (1932) 1.

[HHMS06] J. Haidenbauer, H.-W. Hammer, U.-G. Meißner and A. Sibirtsev, Phys. Lett. B **643** (2006) 29 [arXiv:hep-ph/0606064].

[HM03] H.-W. Hammer and U.-G. Meißner, Eur. Phys. J. A **20** (2004) 469 [arXiv:hep-ph/0312081].

[HMD96] H.-W. Hammer, U.-G. Meißner and D. Drechsel, Phys. Lett. B **385** (1996) 343 [arXiv:hep-ph/9604294].

[Hof56] R. Hofstadter, Rev. Mod. Phys. **28** (1956) 214.

[Hof57] R. Hofstadter, Ann. Rev. Nucl. Part. Sci. **7** (1957) 231.

[Hoh83] G. Höhler, Pion-Nucleon Scattering, in: H. Schopper (Ed.), Landolt-Börnstein, vol. I/9b, Springer, Berlin, 1983.

[Hol95] K. Holinde, Prog. Part. Nucl. Phys. **36** (1996) 311 [arXiv:nucl-th/9512001].

[Hol96] G. Holzwarth, Z. Phys. A **356** (1996) 339 [arXiv:hep-ph/9606336].

[HP75] G. Hohler and E. Pietarinen, Phys. Lett. B **53** (1975) 471.

[HPSB76] G. Höhler, E. Pietarinen, I. Sabba Stefanescu, F. Borkowski, G. G. Simon, V. H. Walther and R. D. Wendling, Nucl. Phys. B **114** (1976) 505.

[HR99a] H.-W. Hammer and M. J. Ramsey-Musolf, Phys. Rev. C **60** (1999) 045204 [Erratum-ibid. C **62** (2000) 049902] [arXiv:hep-ph/9903367].

[HR99b] H.-W. Hammer and M. J. Ramsey-Musolf, Phys. Rev. C **60** (1999) 045205 [Erratum-ibid. C **62** (2000) 049903] [arXiv:hep-ph/9812261].

[JHS94] G. Janssen, K. Holinde and J. Speth, Phys. Rev. Lett. **73** (1994) 1332.

[JLAB00] M. K. Jones *et al.* [Jefferson Lab Hall A Collaboration], Phys. Rev. Lett. **84** (2000) 1398 [arXiv:nucl-ex/9910005].

[JLAB01] O. Gayou *et al.* [Jefferson Lab Hall A Collaboration], Phys. Rev. Lett. **88** (2002) 092301 [arXiv:nucl-ex/0111010].

[Kai03] N. Kaiser, Phys. Rev. C **68** (2003) 025202 [arXiv:nucl-th/0302072].

[KBMT05] S. Kondratyuk, P. G. Blunden, W. Melnitchouk and J. A. Tjon, Phys. Rev. Lett. **95** (2005) 172503 [arXiv:nucl-th/0506026].

[KKRS97] S. Kopecky, M. Krenn, P. Riehs, S. Steiner, J. A. Harvey, N. W. Hill and M. Pernicka, Phys. Rev. C **56** (1997) 2229.

[KL06] B. Kubis and R. Lewis, Phys. Rev. C **74** (2006) 015204 [arXiv:nucl-th/0605006].

[KM00] B. Kubis and U.-G. Meißner, Nucl. Phys. A **679** (2001) 698 [arXiv:hep-ph/0007056].

[Kub01] G. Kubon *et al.*, Phys. Lett. B **524** (2002) 26 [arXiv:nucl-ex/0107016].

[Lac05] J. D. Lachniet, Ph.D. thesis, Carnegie Mellon University, 2005.

[LB80] G. P. Lepage and S. J. Brodsky, Phys. Rev. D **22** (1980) 2157.

[LMOP47] C. M. G. Lattes, H. Muirhead, G. P. S. Occhialini and C. F. Powell, Nature **159** (1947) 694.

[LOP47a] C. M. G. Lattes, G. P. S. Occhialini and C. F. Powell, Nature **160** (1947) 453.

[LOP47b] C. M. G. Lattes, G. P. S. Occhialini and C. F. Powell, Nature **160** (1947) 486.

[Mei91] U.-G. Meißner, Int. J. Mod. Phys. E **1** (1992) 561.

[Mei07] U.-G. Meißner, arXiv:nucl-th/0701094.

[Mel99] K. Melnikov and T. van Ritbergen, Phys. Rev. Lett. **84** (2000) 1673 [arXiv:hep-ph/9911277].

[Mel06] W. Melnitchouk, private communication, 2006.

[Mil02] G. A. Miller, Phys. Rev. C **66** (2002) 032201 [arXiv:nucl-th/0207007].

[MKW86] U.-G. Meißner, N. Kaiser and W. Weise, Nucl. Phys. A **466** (1987) 685.

[MLKM02] D. Merten, U. Löring, K. Kretzschmar, B. Metsch and H. R. Petry, Eur. Phys. J. A **14** (2002) 477 [arXiv:hep-ph/0204024].

[MMD95] P. Mergell, U.-G. Meißner and D. Drechsel, Nucl. Phys. A **596**, 367 (1996) [arXiv:hep-ph/9506375].

[MMSO97] U.-G. Meißner, V. Mull, J. Speth and J. W. van Orden, Phys. Lett. B **408** (1997) 381 [arXiv:hep-ph/9701296].

[MT68] L. W. Mo and Y. S. Tsai, Rev. Mod. Phys. **41** (1969) 205.

[MT05] L. C. Maximon and J. A. Tjon, Phys. Rev. C **62** (2000) 054320 [arXiv:nucl-th/0002058].

[Mue97] B. Mueller *et al.* [SAMPLE Collaboration], Phys. Rev. Lett. **78** (1997) 3824 [arXiv:nucl-ex/9702004].

[MY63] N. Meister and D. R. Yennie, Phys. Red. **130** (1963) 1210.

[Nee61] Y. Ne'eman, Nucl. Phys. **26** (1961) 222.

[Ped05] T. K. Pedlar *et al.* [CLEO Collaboration], Phys. Rev. Lett. **95** (2005) 261803 [arXiv:hep-ex/0510005].

[Phi06] D. R. Phillips, J. Phys. G **34** (2007) 365 [arXiv:nucl-th/0608036].

[Pie] E. Pietarinen, A calculation of $\pi\pi \to N\bar{N}$ amplitudes in the pseudophysical region, University of Helsinky, Preprint Series in Theoretical Physics, HU-TFT-17-77, unpublished.

[Pla05] B. Plaster *et al.* [Jefferson Laboratory E93-038 Collaboration], Phys. Rev. C **73** (2006) 025205 [arXiv:nucl-ex/0511025].

[RD88] A. S. Raskin and T. W. Donnelly, Annals Phys. **191** (1989) 78 [Erratum-ibid. **197** (1990) 202].

[RJ03] J. P. Ralston and P. Jain, Phys. Rev. D **69** (2004) 053008 [arXiv:hep-ph/0302043].

[Ros50] M. Rosenbluth, Phys. Rev. **79** (1950) 615.

[Sab80] I. Sabba Stefanescu, J. Math. Phys. **21** (1980) 175.

[Sal55] G. Salzman, Phys. Rev. **99** (1955) 973.

[Sch49] J. S. Schwinger, Phys. Rev. **76**, 790 (1949).

[Sch99] C. Schwob *et al.*, Phys. Rev. Lett. **82**, 4960 (1999).

[SGS05] M. R. Schindler, J. Gegelia and S. Scherer, Eur. Phys. J. A **26** (2005) 1 [arXiv:nucl-th/0509005].

[Sic01] I. Sick, Prog. Part. Nucl. Phys. **47** (2001) 245 [arXiv:nucl-ex/0208009].

[Sic03] I. Sick, Phys. Lett. B **576** (2003) 62 [arXiv:nucl-ex/0310008].

[Sic06] I. Sick, private communication, 2006.

[Sky61] T. H. R. Skyrme, Proc. Roy. Soc. Lond. A **260** (1961) 127.

[Sky62] T. H. R. Skyrme, Nucl. Phys. **31** (1962) 556.

[Tsa61] Y. S. Tsai, Phys. Rev. **122** (1961) 1898.

[Tza70] C. Tzara, Nucl. Phys. B **18** (1970) 246.

[War03] G. Warren *et al.* [Jefferson Lab E93-026 Collaboration], Phys. Rev. Lett. **92** (2004) 042301 [arXiv:nucl-ex/0308021].

[WBKP00] R. F. Wagenbrunn, S. Boffi, W. Klink, W. Plessas and M. Radici, Phys. Lett. B **511** (2001) 33 [arXiv:nucl-th/0010048].

[WKL95] R. A. Williams, S. Krewald and K. Linen, Phys. Rev. C **51** (1995) 566.

[Yao06] W.-M. Yao *et al.*, J. Phys. G **33** (2006) 1.

[YLR57] D. R. Yennie, M. M. Lévy and D. G. Ravenhall, Rev. Mod. Phys. **29** (1957) 144.

[Yuk35] H. Yukawa, Proc. Phys. Math. Soc. Jap. **17** (1935) 48.

[Zis05] V. Ziskin, Ph.D. thesis, MIT, April 2005.
`http://blast.lns.mit.edu/PUBLIC_RESULTS/THESES/Ziskin.pdf`

[Zwe64] G. Zweig, Published in 'Developments in the Quark Theory of Hadrons'. Volume 1. Edited by D. Lichtenberg and S. Rosen. Nonantum, Mass., Hadronic Press, 1980. pp. 22-101.

Acknowledgements

First and foremost, I would like to express my gratitude to my advisor, Prof. Ulf-G. Meißner, and my co-advisor, Prof. Hans-Werner Hammer, for their endless support. This work would not have been possible without their invaluable advice and discussions. Their ideas and suggestions have always kept me motivated, and have extended this work beyond a pure form factor analysis.

I would like to thank Dr. Bastian Kubis and Dr. Bernard Metsch for valuable discussions. I thank Dr. Bugra Borasoy and Robin Nißler for valuable discussions concerning the generation of error bands for our results.

I express my gratitude to the BABAR collaboration, and in particular Dr. Vladimir Druzhinin, for providing us with preliminary form factor data. I thank the CLAS collaboration, and in particular Dr. Will Brooks, for making the preliminary CLAS data available to us, and for their permission for us to display these data. The analysis of cross section data with Coulomb corrections would not have been possible without the data compilation by Prof. Ingo Sick.

I thank Dr. Wally Melnitchouk for useful discussions of the two-photon exchange effects and for providing the results of the calculations for use in our plots.

Finally, I would like to thank all the staff of the Helmholtz - Institut für Strahlen- und Kernphysik for a very friendly and welcoming working atmosphere.